

LIBRARY Michigan State University

This is to certify that the dissertation entitled

NUMERICAL SIMULATIONS OF SOLAR AND STELLAR CONVECTION AND OSCILLATIONS

presented by

Dali Giorgobiani

has been accepted towards fulfillment of the requirements for the

Ph.D.	degree in _	Physics					
Matt Sth							
	Major Profe	essor's Signature					
	12/9	103					
		Date					

MSU is an Affirmative Action/Equal Opportunity Institution

PLACE IN RETURN BOX to remove this checkout from your record. TO AVOID FINES return on or before date due. MAY BE RECALLED with earlier due date if requested.

DATE DUE	DATE DUE	DATE DUE
AUG 0 9 2006		

6/01 c:/CIRC/DateDue.p65-p.15

NUMERICAL SIMULATIONS OF SOLAR AND STELLAR CONVECTION AND OSCILLATIONS

 $\mathbf{B}\mathbf{y}$

Dali Giorgobiani

A DISSERTATION

Submitted to
Michigan State University
in partial fulfillment of the requirements
for the degree of

DOCTOR OF PHILOSOPHY

Department of Physics and Astronomy

2003

ABSTRACT

NUMERICAL SIMULATIONS OF SOLAR AND STELLAR CONVECTION AND OSCILLATIONS

By

Dali Giorgobiani

The Sun has a resonant cavity between the surface where the density decreases rapidly due to its low temperature and the interior where the sound speed increases with increasing temperature. Sound waves are trapped in this resonant cavity, and thousands of these p-mode oscillations are observed in the velocity Doppler shift and intensity variations of the lines in the solar spectrum. These resonant modes are excited by convection near the solar surface and are used to probe both the local and global structure of the Sun.

The question of interest here is excitation of acoustic waves by convection, and the interaction between convection and the resonant p-modes. Turbulent motions stochastically excite the resonant modes via Reynolds stresses and entropy fluctuations. Interaction between the convective motions and the waves modifies the mode frequencies, spectrum and amplitudes.

We investigate turbulence and its interaction with oscillations by means of the realistic three-dimensional numerical simulations of the shallow upper layer of the solar convective zone. We use the numerical code of Stein & Nordlund, which solves 3D system of the compressible (magneto)hydrodynamic equations and includes LTE radiative transfer near the visible surface.

The properties of oscillation modes in the simulation closely match their observed characteristics. This means that our numerical model reproduces the basic properties of solar oscillations. This is an important step in studying the physical properties of solar oscillations and their interaction with turbulence. The similarity of the oscillation mode properties in the simulation and observations means that the simulations can be used to investigate the origin of mode behavior and its interaction with turbulent plasma.

The frequency spectra of the solar acoustic modes are asymmetric. We study the corresponding asymmetry of the simulation modes in order to understand its origin and its relation to the excitation sources. We find that radiative transfer on top of the convection zone can be responsible for the acoustic mode asymmetry reversal.

Acoustic mode excitation rates depend on the details of the turbulent energy spectra. We analyze spatial and temporal components of the spectra in the simulations to learn more about stellar turbulent convection and its role in mode driving. We use similar simulations of convection in other stars to calculate their mode excitation rates, and determine how p-mode driving depends on stellar parameters.

I would like to dedicate this thesis to my parents

ACKNOWLEDGMENTS

I would like to express my sincere gratitude to a large number of people who helped me in different ways through several stages of my life. First of all, I would like to thank my thesis advisor, Professor Robert Stein, for his support and assistance, for everything I have learned from him, for always being there for me when I needed help. I thank Prof. Stein for allowing me to use his 3D (M)HD code, which is the basis of my research and which represents one of the best analytic tools in the realm of stellar convection, available nowadays. Prof. Stein always clearly defines a problem and actively participates in its solution, using his extensive knowledge and physical intuition; these qualities make it especially enjoyable working with Prof. Stein on the fascinating problems of stellar physics. I am very grateful to Sasha Kosovichev for his interest in my research, for his encouragement and constant help, for countless discussions and patience. I am thankful to him for inviting me to Stanford several times, where I got a better understanding of several aspects of my research. I would like to thank Jeff Kuhn who offered me a Summer Research position at Sac Peak Observatory in 1994 and 1995, and then suggested to apply to MSU to work with Prof. Stein; I am greatly indebted to Jeff for all his help, and especially for welcoming me in this country and granting me the opportunity to continue my research here. I appreciate great help and friendly discussions with Regner Trampedach, my colleague,

friend and officemate. It has been nice to communicate with Dave Bercik, Bill Abbett and Sydney D'Silva. My colleagues and friends, Günter Houdek, Rakesh Nigam and Reza Samadi, helped me to learn more about the theoretical aspects of solar and stellar physics. I am grateful to Pawan Kumar for insightful discussions and his attention to my work. I would like to thank Hans-Günter Ludwig for his helpful questions and creative ideas. I would like to express my deep gratitude to Åke Nordlund who created the 3D numerical code together with Prof. Stein. Jørgen Christensen-Dalsgaard has always been attentive to my research; I would like to thank him for hospitality during my short visit to Århus, Denmark.

My eternal gratitude belongs to my parents George and Florina for encouraging me to follow my father's example and become a scientist, for their constant support and unconditional love; to my brother George for always driving my curiosity; to my husband Eduard Pozdeyev for his support, love and care, for being a fine example of an excellent scientist himself, making me proud of him and wanting to live up to his standards; to my best friends Irma Kuljanishvili and Maria Bailey for being supportive and compassionate and always ready to share my *joie de vivre*. I would like to thank all my other friends for making my life enjoyable and meaningful.

I would like to mention my colleagues at the Abastumani Astrophysical Observatory, Georgia, where I grew up and became enchanted by the mysteries of the Universe, and where I was a PhD student prior to coming here; my colleagues at IZMIRAN, Moscow, where I spent some time working with Vladimir Obridko; professors of Tbilisi State University where I have earned my previous degree; and of course my current fellow students and professors here at PA Department of MSU de-

serve many thanks for being friendly, kind and always ready to help. Shawna Prater and Debbie Simmons deserve special thanks for kindly helping me to take care of all sorts of bureaucratic problems.

TABLE OF CONTENTS

LI	ST OF TABLES	Ж
LI	ST OF FIGURES	x
1	INTRODUCTION 1.1 Helioseismology	1 2 5 7
2	NUMERICAL MODEL	14
3	VELOCITY AND INTENSITY LINE PROFILES 3.1 Introduction	18 19 20 22 26 26
4	ROLE OF RADIATIVE TRANSFER IN THE ASYMMETRY REVERSAL	28
	4.1 Introduction	29 30 32 33 37 41
5	SOURCE DEPTHS AND ASYMMETRIES 5.1 Introduction	44 44 45 52
6	SPECTRAL PROPERTIES OF TURBULENT CONVECTION 6.1 Introduction	53 53

	6.3	Conclusions
7	EX	CITATION OF STELLAR OSCILLATIONS
	7.1	Introduction
	7.2	Mode Excitation Rates
	7.3	Stellar Simulations
	7.4	Results
	7.5	Conclusions
8	CO	NCLUSIONS
	8.1	Summary
	8.2	Future Work

LIST OF TABLES

1	Simulated stars,	resolution	$50 \times 50 \times 82$								79
2	Simulated stars,	resolution	$125\times125\times82$								80

LIST OF FIGURES

1	Observed and simulated power spectra of velocity for $\ell=740$ from the SOHO/MDI and for the first non-radial mode (with a 6 Mm horizontal wavelength) from a 72 hour simulation of solar surface convection on a 6 Mm \times 6 Mm \times 3 Mm deep domain. Observed velocities are from the Doppler shifts of the NiI 6768 Å line summed over all $m=2\ell+1$ modes. Velocity power spectral density is in units of $(cm/s)^2/Hz$. The simulated modes are sparser and broader than the observed modes because the simulated domain is shallower than the turning points of the observed modes, resulting in a smaller mass for the simulated modes	24
2	Observed and simulated power spectra of intensity for the same cases as the velocity in figure 1. Observed intensity is from the NiI 6768 Å line summed over all $m=2\ell+1$ modes. Observed intensity power spectral density is in units of (CCD counts per sec) ² /Hz. Simulated intensity is from the solution of the transfer equation along a vertical ray. Simulated intensity power spectral density is in units of $(erg/cm^2/s/ster)^2/Hz$	25
3	Observed and simulated intensity – velocity phase difference. Observed data is from SOHO/MDI with $\ell=740$ summed over all $m=2\ell+1$ values. Simulated data is for the first non-radial mode (with horizontal wavelength 6 Mm). The phase jumps $\sim \pi/2$ at the modes where the oscillation amplitude is large	27
4	Spectrum of intensity, I_{ν} , in erg cm ⁻² s ⁻¹ sterad ⁻¹ . The solid curve is smoothed over $\Delta \nu = 0.23$ mHz	34
5	Spectrum of temperature, T_{ν} , at $\tau(x, y, t) = 1$. Again, the solid curve is smoothed	35
6	Phase difference between the intensity and the temperature measured at the $\tau=1$ level	35
7	Spectrum of velocity, V_{ν} , at $\tau(x, y, t) = 1$. Its spectrum is almost the same at fixed geometrical depth corresponding to $\langle \tau \rangle_{x,y,t} = 1$. Observed Doppler velocity spectrum is plotted for comparison	36

8	Spectrum of temperature, I_{ν} , at $\langle \tau \rangle = 1$. The temperature at $\langle \tau \rangle = 1$ has the same asymmetry as the velocity	36
9	The temperature (dashed) and velocity (solid) spectrum for the first non-radial fundamental mode measured at $<\tau>=1$. Here and after, diamonds represent unsmoothed temperature profiles, whereas stars correspond to the parameter on the left y-axis. The temperature and velocity profiles look similar to each other. Curves are smoothed over $38.6~\mu{\rm Hz}.$	38
10	The temperature (dashed) and velocity (solid) spectrum for the first non-radial fundamental mode measured at $\tau=1$. The amplitude of the temperature fluctuations is nonuniformly reduced across the mode peak	38
11	The temperature (dashed) and opacity (solid) spectrum for the first non-radial fundamental mode measured at $<\tau>=1$. The larger temperature fluctuations on the low frequency side of the mode produce larger opacity variations.	39
12	The spectrum of the height of local optical depth one, $z_{\tau(x,y,t)=1}$, (solid) and temperature (dashed) measured at local $\tau=1$. The location of local optical depth unity varies more on the low frequency side of the mode, where the opacity variation is larger due to the larger temperature fluctuations. This reduces the temperature fluctuations at local optical depth unity more on the low frequency side of the mode compared to the high frequency side and, in accordance with the Eddington-Barbier relations, leads to smaller intensity fluctuations on the low frequency side of the mode and larger intensity fluctuations on the high frequency side of the mode	40
13	The phase (solid line) between the height of $\tau=1$ and the temperature at $<\tau>=1$. Phase $\approx 180^{\circ}$ means that the height of unit optical depth is greatest (smallest z and lowest temperature) when the temperature at $<\tau>=1$ is largest. Also shown is temperature at $\tau=1$ (dashed)	43
14	Kinetic energy power spectra at different depths (upper graph) and integrated over the depth (lower graph). Ordinates are logarithmic, with arbitrary units	46
15	Well mode profiles in the region I (below the source). Lines become lighter with depth, and the thick line is the line profile measured at the surface. Profiles are different for different source locations, and their asymmetry changes with depth. Source locations are measured from the surface down. The ordinate is a normalized power. The colorbar indicates the sampling depth, in Mm, relative to the surface.	50

16	Comparison of the simulated velocity power spectra with the square well (upper part) and mean atmosphere potential (lower part). Different lines and numbers correspond to different source locations. Minima are matched at the high frequency ends of modes. Ordinates are in relative units. Model profiles were shifted in frequency for a better fit.	51
17	$k-\nu$ diagram for the gas pressure at the depth 1 Mm beneath the solar surface. Note the broad power peak in the convection region and narrow acoustic mode ridge	58
18	Temporal power spectra of the vertical velocity at 0.5 Mm beneath the surface, for different k_h values (in Mm ⁻¹). The spectra follow a power law at low k_h and form plateau at high k_h , exponentially decaying at high frequencies. Modal structure appears at low k_h in the peak driving range of frequencies	59
19	Temporal power spectra of the horizontal velocity at 0.5 Mm beneath the surface. Different values of k_h (in Mm ⁻¹) are considered. The spectra behave in similar way as the vertical velocity spectra, but modes are not visible	59
20	Temporal power spectra of the vertical velocity, at two depths z and for several wavenumbers k_h . Different power laws represent these spectra rather well, especially at low k_h . At higher k_h , broad plateau forms, and all functions give satisfactory fits	61
21	Temporal power spectra of the horizontal velocity, at same depths and wavenumbers. At low k_h , either power laws or LF could be a good representation of these spectra, while at higher k_h the spectra fall off as EF at high frequencies	62
22	Temporal power spectra of the turbulent pressure, again at same depths and wavenumbers. Almost everywhere, LF seems to be a good match for these spectra. At low k_h , power laws also work rather well	63
23	Temporal power spectra of the gas pressure, at same z and k_h values. As in vertical velocity, mode peaks are visible at low k_h . The spectra behave like LF or power laws at low k_h , and look similar to EF at high k_h	64
24	Temporal power spectra of the entropy, at same depths and wavenumbers. At large depths, they look like LF; power laws also fit well at low k_h . At low depths, they form a plateau and drift from LF to EF with increasing k_h	65

25	Frequency averaged spatial spectra of the vertical velocity at different depths. Thin solid line represents the power law of -5/3 characteristic for the turbulent cascade. The inertial range is extremely short, almost non-existent.	66
26	Vertical velocity spatial spectra for low frequencies, ν (in mHz), at 0.5 Mm below the surface. The inertial range extends from $k \simeq 3$ Mm ⁻¹ to $k \simeq 15$ Mm ⁻¹	66
27	Vertical velocity spatial spectra for higher frequencies, in the peak driving range between 1 and 5 mHz. Inertial range disappears with increasing frequency. High k decaying tail corresponds to the numerical damping	67
28	Spatial spectrum of the vertical velocity at 0.5 Mm, at $\nu=2$ mHz, away from the modes (stars). Two power laws, $k^{1.9}$ and $k^{-5/3}$, describe low and high k behavior (solid lines)	67
29	Spectra of excitation rates per unit area, due to the total pressure fluctuations, for the simulated stars. Peak excitation increases with increasing effective temperature and lower surface gravity shifts the spectrum to lower frequencies	81
30	Energy input rate per unit area integrated over the frequency (base $10 \log \operatorname{arithms}$ in $\operatorname{erg/cm^2/s}$) as a function of $T_{\rm eff}$ and $\log g$ for two sets of stellar simulations. Excitation is higher in hotter stars with larger convective fluxes and higher convective velocities	82
31	Energy input rate integrated over the frequency (base 10 logarithms in erg/s), presented as function of $T_{\rm eff}$ and $\log g$ for two sets of stellar simulations. Total excitation is higher in hotter stars and in stars with lower surface gravity, where convection is more vigorous and surface area is larger	83
32	Energy input rate integrated over frequency as a function of effective temperature (stars). The excitation is fit by a power law, $dE/dt \propto T_{\rm eff}^9$ (solid line)	85
33	Energy input rates in the Sun for different spatial resolution	89
34	Mode driving in the Sun. Contributions from gas- and turbulent-pressure are shown separately, along with the total excitation rate	90
35	Mode driving in the FV star. As in Fig. 34, the individual contributions, as well as the total excitation rates, are presented. \dots .	91
36	Mode driving in the KV star. As in Fig. 34, the individual contributions, as well as the total excitation rates, are presented	92

37	Mode driving in the KIV star. As in Fig. 35, the individual contributions, as well as the total excitation rates, are presented. Note the different frequency range.	93
38	Energy input rate due to the turbulent pressure, per unit area, integrated over the frequency (base 10 logarithms in $erg/cm^2/s$) as a function of $T_{\rm eff}$ and $\log g$. Excitation is higher in hotter stars with larger convective fluxes and higher convective velocities	94
39	Energy input rate due to the gas pressure, per unit area, integrated over the frequency (base 10 logarithms in $\operatorname{erg/cm^2/s}$) as a function of $T_{\rm eff}$ and $\log g$ for two sets of stellar simulations. Excitation is higher in hotter stars with larger convective fluxes and higher convective velocities	95
40	The frequency-integrated excitation rates as a function of the maximum rms vertical velocity. The main sequence stars' excitation vary roughly as $v^{1.5}$	96

Images in this dissertation are presented in color.

Chapter 1

INTRODUCTION

Oscillatory motions in the solar atmosphere were discovered by Leighton (see Leighton et al. 1962). These photospheric motions known as "5-minute oscillations" have periods between 3 and 12 minutes. After a decade, Ulrich (1970) and Leibacher & Stein (1971) explained their existence as standing waves trapped in a solar resonant cavity. Five years later, Deubner (1975) discovered that these oscillations have a spectrum of discrete frequencies. The 5-minute oscillations are identified as acoustic waves, or p-modes, because the pressure gradient acts as a restoring force. The discrete mode pattern is a consequence of the existence of a resonant cavity with reflecting boundaries. A special case is represented by the fundamental mode, or f-mode, which is a surface gravity wave. It is incompressible and does not have radial nodes. There exist also gravity waves, where buoyancy acts as a restoring force, as well as fast and slow MHD and Alfven waves driven by interaction of turbulence with magnetic fields. These waves are beyond the scope of our work.

Solar p-mode oscillations are observed as fluctuations of intensity and Doppler velocity. Terrestrial observations suffer from several constraints, e.g., atmospheric turbulence and day-night cycle data gaps. The SOlar and Heliospheric Observatory (SOHO), launched in 1995, overcomes these problems and produces high-quality he-

lioseismic data. The Michelson Doppler Imager (MDI) on board the SOHO mission observes solar oscillations using the NiI 6768 Å absorption line (Scherrer et al. 1995). MDI provides information about the continuum intensity, Doppler velocity and line depth. Continuous coverage is also provided by the Global Oscillation Network Group (GONG) array of telescopes girdling the Earth (Hill et al. 1994).

1.1 Helioseismology

Modes of different frequencies and wave numbers penetrate to different distances inside the Sun and provide information about the levels where they were refracted back up to the solar surface. Studying solar oscillations allows us to learn about the solar interior. They provide the most detailed knowledge we have of the internal structure of the Sun, from the surface almost to the center (e.g. Christensen-Dalsgaard 2002). The outstanding questions that remain to be understood revolve around the dynamical interaction between the oscillations and turbulent convection – the excitation, damping, frequency shifts, and spectrum modifications of the oscillations.

The forward method of global helioseismology begins with the computation of a solar model. From this model, one calculates the depth dependent coefficients of the oscillation equations, which are then solved numerically, subject to specific boundary conditions, for their eigenfrequencies and eigenfunctions (radial dependence of the displacement). By adjusting parameters in the solar models, one can achieve a close match between the calculated and observed modes and therefore choose the most appropriate solar model. This method provides constraints on the solar metallicity, depth of convection zone, correct form of the equation of state etc. The inverse prob-

lem in helioseismology consists of determining aspects of the solar internal structure from the values of its observed eigenfrequencies. The differences between the theoretical and observed frequencies together with functions giving the sensitivity of the frequencies to perturbations of the model are used to determine the temperature, density and rotational structure of the solar interior. P-modes of different angular degree ℓ penetrate to different depths in the Sun and provide information about variation of local sound speed with depth. For the Sun, several thousands of acoustic modes have been identified and measured with a relative standard deviation of less than 5×10^{-6} and from which the sound speed variation has been determined with an accuracy of better than 0.5% (e.g. Basu et al. 1996).

Local helioseismology uses the observed modes to probe the near surface structure of the Sun to determine flow velocities, sound speed and magnetic field structures. There are several methods used in this field.

Time – distance helioseismology measures the time taken by a wave packet to travel from one point on the solar surface to another (Duvall et al. 1993b; Kosovichev & Duvall 1997). The wave travel time depends on the sound speed perturbations and the velocity of flow along the ray paths. The effects of the sound speed perturbations and flows can be separated by measuring the wave travel time propagating in opposite directions along the same ray paths. Magnetic fields cause anisotropy of the wave speed. The inversion method applied to infer the properties of subsurface convection is based on a geometric acoustic ray approximation.

The Fourier-Hankel approach decomposes oscillations into waves propagating inwards and outwards between a point on the solar surface and surrounding annulus

and computes their amplitudes and phases (Braun et al. 1988; Cally & Bogdan 1997). The outgoing waves can be viewed as being produced by scattering of the incoming waves, induced emission forced by the incoming waves and spontaneous emission. The relation between incoming and outgoing waves depends on the properties of the region being analyzed (Bogdan et al. 1998), and is computed by solving the inhomogeneous wave equation for the scattered waves in the Born approximation. From the solution, the phase shifts between the incoming and outgoing waves of individual modes are computed. The variations of the phase shifts with angular degree ℓ and radial order n show different behavior for inhomogeneities with different characteristic depths (Fan et al. 1995; Chou et al. 1996).

The basic idea of the helioseismic holography (Lindsey & Braun 1997) is to use the time-reversed, observed wave field as a wave source to drive a sourceless model of the Sun. For a single point source, the resulting waves that propagate downward from the surface, attain a maximum value at that point in space and time where the original source was located. Essentially, the method consists of tracking the excitation source back in time and space. The difficulty of this method is that the images of single point sources will produce significant overlap if the source density is large. Same problem occurs if the source is extended in space. Skartlien (2001) improved this method by modifying the exact Green's functions (the propagators of the image wave field) to eliminate wave reflection and make reliable source images in case of large source density.

1.2 Mode Frequencies and Spectral Asymmetries

The first step in global helioseismology is determining the mode frequencies from the solar observations. Solar acoustic mode frequencies were originally determined by fitting a (symmetric) Lorentzian profile to the power spectra. Later it was discovered (Duvall et al. 1993a) that oscillation spectra of p-modes are asymmetric, and velocity and intensity spectra exhibit an opposite sense of asymmetry. It is important to study p-mode line asymmetries in order to refine the process of frequency calculations. The assumption that line profiles are symmetric and can be fitted by a Lorentzian, fails. This approach leads to systematic errors in determination of eigenfrequencies and therefore affects the results of helioseismic inversions. Instead, it is advisable to use the phenomenological asymmetrical fitting formalism by Nigam & Kosovichev (1998). This phenomenon was studied by several authors (Duvall et al. 1993a; Gabriel 1993; Abrains & Kumar 1996; Roxburgh & Vorontsov 1997; Nigam et al. 1998; Rast & Bogdan 1998; Georgobiani et al. 2001). They have found that the asymmetries depend on the acoustic source depth and type. For a sufficiently localized source, the source depth determines the frequencies of minima of the p-mode power, while the positions of the modal maxima are determined by the resonant properties of the acoustic cavity, and are therefore universal for a given angular degree ℓ . The minima do not lie in the middle between the maxima, which makes line shapes asymmetric and provides a diagnostic of the source properties.

In reality, the observed Doppler shift and intensity fluctuations used to construct p-mode spectra contain not only pure acoustic waves, but also contributions from the convective motions near the solar surface, in the zone where the spectral lines are formed. Granulation manifests similar timescales and length scales as do p-modes of high degree ℓ , excited near the surface. Granular motions can contribute additive noise to the p-mode spectra. Some part of this noise maybe associated with acoustic sources and thus be correlated with the acoustic modes (Nigam & Kosovichev 1998). Solar oscillations are excited by turbulent solar convection and according to Goode et al. (1998), they are excited in the intergranular dark lanes. Therefore, the observed fluctuations have a noise component which originates directly from the intergranular lanes and is correlated to the amplitude of the oscillations. This correlated noise is then the signature of the nonlinear granular dynamics, which occurs within some time interval of the wave excitation. The phase relationship between the correlated noise and the acoustic modes thus contains the information on the source characteristics.

Realistic three-dimensional simulations of the solar convection zone with radiative transfer at the visible surface have resonant acoustic modes similar to the
Sun. The emergent intensity and vertical velocity in the simulated atmosphere have
asymmetric power spectra, and their asymmetry is reversed like in the Sun. Plasma
temperature in the simulations behaves as intensity when measured at continuum
optical depth equal to 1 (the visible solar surface), but it exhibits velocity-like asymmetry when sampled at fixed geometrical depth at which average optical depth is
unity. The opacity is a non-linear function of temperature. Oscillations cause opacity changes which in turn alternate the location of radiation emission in a way that
reduces the magnitude of temperature fluctuations nonuniformly across the mode
peak and reverses its asymmetry. In the regions where the local temperature is hot-

ter, the opacity is larger, therefore the radiation temperature (which is the same as the gas temperature at local optical depth unity) becomes significantly reduced. This indicates that the asymmetry reversal in the simulations is caused by radiative transfer effects, rather than correlated noise.

1.3 Acoustic Mode Excitation

A theory of sound generation by fluid flow in a homogeneous medium was originally developed by Lighthill (1952). According to this theory, sound is generated by conversion of kinetic energy into acoustic energy as a result of fluctuations in the fluid. Lighthill combined the equations of motion, with the linear and nonlinear terms separated, into an inhomogeneous wave equation. The linear terms collected on the left hand side represent the wave propagation operator. The remaining nonlinear terms gathered on the right hand side are interpreted as source terms for the waves. If there are no source terms, then the wave equation becomes homogeneous and governs free wave propagation. With source terms, the wave equation represents the equation of sound propagation in a uniform medium due to externally applied fluctuating stresses. It is assumed that all effects such as the convection of sound by the turbulent flow or the variations of sound speed within it, are taken into account and incorporated in those stresses. Originally, Lighthill introduced his theory to understand and reduce aerodynamic jet engine noise. In his theory, the quadrupole sources (Reynolds stresses) are shown to behave as if they are concentrated into independent quadrupoles, one in each average turbulent eddy volume.

In general, the right hand side of the inhomogeneous wave equation contains

sources of different multiplicity. The monopole source arises from the continuity equation as a result of forcing the mass in a fixed region of space to fluctuate. In the Sun, entropy fluctuations due to radiative cooling at the surface are responsible for the monopole source. The momentum equation contains the force term with both dipole and quadrupole (turbulent Reynolds stress) source. The dipole source is a result of forcing the momentum in a fixed region of space to fluctuate. Both entropy and momentum flux are responsible for the dipole emission on the Sun. The quadrupole source accounts for fluctuating rates of momentum flux across fixed surfaces. Essentially, internal stresses with no associated mass or momentum flux (as in free turbulence) are responsible for quadrupolar emission of acoustic waves. In the Sun, quadrupole sources are represented by Reynolds stresses.

For turbulence in the absence of external forces (free turbulence), there is no net mass or momentum transfer, and sound is generated by quadrupole emission only. In a gravitational field, monopole and dipole emission also occur (Unno 1964; Stein 1967), therefore one has to take into account the effect of gravitational stratification when considering the wave excitation in stellar atmospheres. Stein (1967) extended Lighthill's method to calculate the acoustic and gravity wave emission by turbulent motions in a stratified atmosphere. He also computed acoustic emission assuming a variety of different forms for the spatial and temporal components of turbulent spectrum.

Solar acoustic oscillations are excited by Reynolds stress and entropy fluctuations produced by turbulent convection near the solar surface (Goldreich & Kumar 1990; Stein & Nordlund 1991; Balmforth 1992; Bogdan et al. 1993; Goldreich et al.

1994; Kumar 1994, 1997; Stein & Nordlund 1998a; Nordlund & Stein 1998). Goldreich & Keeley (1977) identified the turbulent Reynolds stress as the main source term of stochastic excitation of the solar acoustic modes. They derived an approximate estimation for the acoustic power injected into the oscillations by assuming equipartition of energy between the turbulence and oscillations. Later, entropy fluctuations were added as a possible excitation source (Stein & Nordlund 1991; Balmforth 1992; Goldreich et al. 1994; Samadi & Goupil 2001). Balmforth (1992) examined how the acoustic emission excites global pulsations and, following Goldreich & Keeley (1977), derived the expression for the rate of energy injected into modes by quadrupole emission through the fluctuating Reynolds stress. A similar expression could be obtained for the emission of the acoustic radiation by low order multipole sources through the fluctuating entropy. Goldreich et al. (1994) calculate the ratio of the noise generation rate between the fluctuating entropy and Reynolds stress. Estimations of this ratio for the solar conditions result in the noise generation rate due to the fluctuating entropy being about an order of magnitude larger than the contribution from the fluctuating Reynolds stress. Samadi & Goupil (2001) proposed a turbulent excitation model based on the approach of Goldreich et al. (1994). They included a more sophisticated model for the excitation process due to entropy perturbations. They also show that the actual entropy source term results from the advection of the entropy fluctuations by the turbulent motions. There is some disagreement concerning the comparative importance of turbulent stress versus entropy source terms: entropy fluctuations are found to contribute to excitation significantly in the analytical approach of Goldreich et al. (1994) and in the earlier results of the numerical simulations

(Stein & Nordlund 1991), but are not so large in recent results from the same simulations (Stein & Nordlund 2001) or even negligible in other cases (Balmforth 1992). A related, but not identical problem is the importance of the sources of different multiplicity. There is a certain inherent ambiguity in the formulation of the wave excitation in terms of these sources, resulting from writing down the wave equation without properly considering the turbulent eddy dynamics, according to Balmforth (1992). He finds the monopole and dipole sources unimportant comparing to the quadrupole source, but admits that this effect could exist due to the assumption of the adiabatic stratification, in the manner of Goldreich & Kumar (1990). In their formalism, there exists a destructive interference between the monopole and dipole source amplitudes. Goldreich et al. (1994) state that although the monopole and dipole amplitudes are individually larger than the quadrupole amplitude, their sum compares to the quadrupole source.

The analytic excitation formulations of Stein (1967), Goldreich & Keeley (1977), Balmforth (1992), Goldreich et al. (1994), Musielak et al. (1994), Samadi & Goupil (2001) and others all require a model of the turbulent medium. Unfortunately, there are no complete models of stellar turbulence. The energy spectrum in the Sun is not exactly a Kolmogorov spectrum, according to the observations of Nesis et al. (1993) and others. The mixing length theory (Böhm-Vitense 1958) describes mean properties in stellar envelopes fairly well, but it does not accurately reproduce dynamic properties, and besides, it introduces free parameters. Sophisticated three-dimensional numerical simulations do not introduce free parameters and describe the upper layers of the solar atmosphere rather well, capturing both its static and dy-

namic properties (e.g. Stein & Nordlund 2000). They can be used to determine the statistical properties of the turbulent convection.

The analysis of temporal and spatial spectra of the simulated convection shows several trends. Temporal spectra have different functional forms at various spatial wavenumbers. They behave as power laws at low wavenumbers, while they are exponential at high wavenumbers. Spatial spectra obey the Kolmogorov scaling law and exhibit extended inertial ranges only at low frequencies; at high frequencies, there is no signature of the inertial range. These results differ from the previous assumptions of Gaussian-like temporal spectra and Kolmogorov-like spatial spectra, therefore they are important for future development of analytical estimates of the acoustic excitation.

1.4 Asteroseismology

The solar oscillations are excited by subsurface convection, thus one can expect that all stars with an outer convection zone exhibit similar oscillations. Such oscillations are referred to as solar-like to emphasize that they are stochastically excited by convection. Unfortunately, in solar-like stars, the p-mode amplitudes are very small, thus very difficult to detect in remote stars. However, recently several groups produced convincing observational evidence of solar-like oscillations in other stars (Bedding & Kjeldsen 2003); cf also Chapter 7.

For stars other than the Sun, it is impossible to visually resolve stellar disks. Only low ℓ modes are observable in light integrated over the stellar disk, because modes with $\ell=4$ and higher are canceled out. The visible peaks in spectra appear

almost uniformly spaced, and can be identified as a sequence of $\ell=1$ acoustic modes alternating with closely spaced double peaks arising from $\ell=0$ and $\ell=2$ modes. From asymptotic theory applied to the frequency set (Tassoul 1980) one can obtain two parameters describing the so-called large separation of the cyclic frequency $\nu_{n,\ell}$ of modes of same degree ℓ and adjacent radial order n and the small frequency separation of the closely spaced peaks which measures $\nu_{n,0} - \nu_{n-1,2}$. These seismic parameters essentially provide information about the global structure of a star and about the inhomogeneities in the core due to changes in the mean molecular weight with depth and in particular with age. These parameters can be obtained from full-disk measurements in integrated light, and they may help to refine our knowledge about the stellar interiors as well as determine masses and ages of solar-type stars (Christensen-Dalsgaard 1988).

Asteroseismology provides a means for inferring the internal structure, composition, rotation, and magnetic activity from observations of low angular order global oscillation modes. Several space missions – COROT (Baglin & The COROT Team 1998), MOST (Matthews et al. 2000), Eddington (Roxburgh & Favata 2003) and others – will supply a wealth of data that can help in refining our understanding of structure of all the observed stars. For correct interpretation of the oscillation data and accurate measurements of normal mode frequencies, it is important to know the physical characteristics of the oscillations such as the distribution of the mode amplitude, linewidth, and line asymmetry that are determined by the excitation mechanism, as well as the frequency shift due to the interaction between the waves and turbulence.

To date, the only estimates of the oscillation amplitude are made by postulating equipartition between the energy of an oscillation mode and the kinetic energy of one convective eddy or balance between acoustical energy generation by turbulence (Lighthill mechanism) and linear damping, and using mixing-length theories of convection. These phenomenological estimates are not accurate even for the solar case.

We investigate properties of oscillations of stars by means of the realistic numerical simulations of the upper turbulent convective layer for a broad range of stellar parameters. These simulations will help us to investigate interaction between stellar turbulent convection and oscillations and its dependence on global stellar parameters. We find that stellar excitation rates per unit area increase with increasing effective temperature and are nearly independent of surface gravity. Reynolds stress and entropy fluctuations make similar contributions to the excitation rates in solar-like stars, but in hotter stars and sub-giants, the dominant driving is caused by Reynolds stress fluctuations.

Chapter 2

NUMERICAL MODEL

Sophisticated simulations of solar surface convection generate acoustic mode oscillations, like in real Sun. Therefore numerical models can be used to study properties of p-mode oscillations. Stellar convection is modeled by means of the three-dimensional numerical code, solving the complete system of MHD equations. The equations of mass, momentum and internal energy conservation, along with the induction equation, are solved for variables $\ln \rho$ (logarithm of density), \mathbf{u} (velocity), \mathbf{e} (internal energy per unit mass) and \mathbf{A} (vector potential):

$$\begin{split} \frac{\partial \ln \rho}{\partial t} &= -\mathbf{u} \cdot \nabla \ln \rho - \nabla \cdot \mathbf{u}, \\ \frac{\partial \mathbf{u}}{\partial t} &= -\mathbf{u} \cdot \nabla \mathbf{u} + \mathbf{g} - \frac{P}{\rho} \nabla \ln P + \frac{1}{\rho} \mathbf{J} \times \mathbf{B} + \frac{1}{\rho} \nabla \cdot \tau, \\ \frac{\partial e}{\partial t} &= -\mathbf{u} \cdot \nabla e - \frac{P}{\rho} \nabla \cdot \mathbf{u} + Q_{rad} + Q_{visc} + Q_{joule}, \\ \frac{\partial \mathbf{A}}{\partial t} &= \mathbf{u} \times \mathbf{B} - \eta \mathbf{J} \end{split}$$

(Nordlund & Stein 1989, 1990). Here, **g** is the gravitational acceleration, P is the gas pressure, **J** is the electric current density, **B** is the magnetic field, τ is the turbulent Reynolds stress tensor, Q_{rad} is the radiative heating, Q_{visc} and Q_{joule} are the viscous

and resistive dissipation, and η is the resistivity. The time advance is a third order predictor - corrector. Sixth-order compact centered derivatives are used in horizontal directions, while cubic splines are applied in the vertical direction, to achieve high accuracy with small numerical damping.

The simulations are essentially parameter-free; the only parameters are the grid resolution and the numerical viscosity and resistivity coefficients. The resolutions used are 253×253×163, 125×125×82 and 63×63×63 grid points (the first two numbers represent the horizontal area, the third number is vertical resolution). The simulated convection domain represents the box of 6 Mm by 6 Mm horizontally and 3 Mm in vertical direction, extending from the temperature minimum down to 2.5 Mm beneath the visible surface. Numerical diffusion is present in each equation for the code stabilization and prevention of the energy accumulation at the smallest scales. On the other hand, diffusion decreases with increasing wavelength to avoid damping on the well resolved scales. The numerical viscosity coefficients are kept at minimum sufficient for smooth variation of all the variables.

The physics of the calculations is detailed enough to realistically model convection near the solar surface and photosphere above it. A proper equation of state and radiation treatment must be included if one needs to make quantitative comparisons with observations.

The internal energy is dominated by ionization near the surface. In the code, the net flux is constrained to have the solar value, therefore one needs to include the ionization energy contribution to the total flux in order to reproduce the observed velocity and temperature fluctuation amplitudes. The equation of state is tabulated

to include ionization and excitation of hydrogen, helium and other abundant atoms, as well as H_2 molecule formation.

Radiative transfer is very important in determining the structure of the upper convective zone and overlying photosphere. Radiative energy exchange generates the entropy fluctuations that produce buoyancy work, thus driving the convection. The top of the convective zone corresponds approximately to the surface where the continuum optical depth $\tau_{cont}=1$, therefore neither the diffusion approximation nor the optically thin approximation give reasonable results. In the code, the three-dimensional, LTE radiation transfer is included. The radiative energy exchange rate is calculated solving the Feautrier equation along straight, slanted, rays, after averaging the Planck function into four bins by wavelength sorted according to opacity (cf Nordlund 1982; Nordlund & Stein 1990, 1991). Line blocking is also included because it increases the temperature of the photosphere and therefore modifies the atmospheric structure.

Boundary conditions are important to ensure the appropriate behavior of the incoming and outcoming fluid. In reality, the simulated convection domain is coupled to an external medium with a priori unknown characteristics. However, the convection is driven at the surface by the entropy fluctuations generated by radiative cooling in the atmosphere. The region above the simulated atmosphere contains too little mass to influence the interior significantly. On the lower boundary, convection asymptotically approaches its adiabatic state, with nearly uniform and isentropic upflowing fluid. Therefore, the lack of information about the region below 2.5 Mm should not significantly affect our results. For these reasons, and to minimize the

boundary effects, we use periodic horizontal boundary conditions and transmitting top and bottom boundaries. The parameters at the top of the simulated domain (particularly, the effective temperature) is adjusted by changing the entropy of the incoming fluid at the bottom, until they reach the solar values. To ensure stability, the total pressure (sum of gas and magnetic pressures) at the bottom is kept horizontally uniform by adjusting the mass and energy densities consistent with isentropy. The magnetic field is potential at the top boundary. At the bottom boundary horizontal field is advected into the simulation domain by inflows. The field in outflows is determined using one-sided derivatives. To facilitate the analysis of acoustic mode driving, the instantaneous net vertical mass flux is zero at the bottom boundary, making it therefore a node for vertical modes of the oscillations.

Chapter 3

VELOCITY AND INTENSITY LINE PROFILES

We use the three-dimensional hydrodynamic code of Stein and Nordlund to realistically simulate the upper layers of the solar convection zone in order to study physical characteristics of solar oscillations. Our first result is that the properties of oscillation modes in the simulation closely match the observed properties. Recent observations from SOHO/MDI and GONG have confirmed the asymmetry of solar oscillation line profiles, initially discovered by Duvall et al. In this chapter we compare the line profiles in the power spectra of the Doppler velocity and continuum intensity oscillations from the SOHO/MDI observations with the simulation. We also compare the phase differences between the velocity and intensity data. We have found that the simulated line profiles are asymmetric and have the same asymmetry reversal between velocity and intensity as observed. The phase difference between the velocity and intensity signals is negative at low frequencies and jumps in the vicinity of modes as is also observed. Thus, our numerical model reproduces the basic observed properties of solar oscillations, and allows us to study the physical properties which are not observed.

3.1 Introduction

The peaks of solar oscillation modes observed in velocity and intensity power spectra are asymmetric (Duvall et al. 1993a). Moreover, the asymmetry between the velocity and intensity line profiles is reversed. This latter was a puzzling result, and it was initially thought to be an error in the observations (Abrams & Kumar 1996). However, recently it was confirmed by SOHO/MDI observations (Nigam et al. 1998). The velocity power spectrum has negative asymmetry (more power on the low frequency side of the peak), while the intensity power spectrum has positive asymmetry (more power on the high frequency side of the peak). In general, the asymmetry is a result of excitation of solar oscillations by a localized source. It originates from the interference of direct waves from the source with waves that start inward and are refracted back out. The asymmetry is a strong function of frequency, and varies weakly with angular degree ℓ .

The reversal of asymmetry between velocity and intensity is thought to be due to the presence of correlated background noise, whose level depends on characteristics of granulation (Nigam et al. 1998). Since the model of Nigam et al. (1998) is a phenomenological one, the physics of the correlated noise is not yet fully understood. Roxburgh & Vorontsov (1997) proposed that the reversal in asymmetry occurs in velocity. Observations suggest that the reversal occurs in intensity as proposed by Nigam et al. (1998). It is therefore desirable to test these ideas. Realistic 3D hydrodynamic simulations of upper layers of the solar convection zone (e.g. Stein & Nordlund 1989, 1998b) have p and f modes with similar asymmetries and asymmetry

reversals as the observed modes. These simulations can therefore be used to study the characteristics of the correlated noise.

We have found that the reversal of asymmetry between velocity and intensity may be due to radiation transfer effects - asymmetry in the temperature fluctuations produces asymmetric opacity variations, which leads to an asymmetry in the height of formation of the observed radiation.

Another interesting property of solar oscillation modes is the phase difference between velocity and intensity, which was first observed by Deubner & Fleck (1989) and studied theoretically by Marmolino & Severino (1991). It may provide a useful diagnostic of the excitation mechanism of the oscillations. Severino et al. (1998), Straus et al. (1998), Oliviero et al. (1999), Nigam & Kosovichev (1999) and Skartlien & Rast (2000) attribute the phase behavior to the interaction of the correlated background with the oscillations. These phase relations can also be studied using the realistic hydrodynamic simulations of the near surface layers of the Sun.

3.2 Calculations of Power Spectra

SOHO/MDI and GONG measure the oscillations in velocity and intensity from the Ni I 6768Å absorption line, which is formed about 200–300 km above the photosphere. The MDI instrument on SOHO spacecraft records filtergrams (intensity images at five wavelengths) which span the absorption line. The velocity signal is obtained by differencing the filtergrams on opposite sides of the line which is sensitive to Doppler shift and minimizes the effect of intensity fluctuations. The intensity signal is obtained by summing the filtergrams in a way to approximate the continuum

intensity in the vicinity of the spectral line and minimize the effects of Doppler shifts (Scherrer et al. 1995). For the comparison with the numerical simulations, we use a time series of the spherical harmonic transform of the full-disk data for $\ell=740$. (The first non-radial mode in the simulations has a wavelength of 6 Mm). The effect of solar differential rotation is removed; and the oscillation power spectra are summed over all $2\ell+1$ m values. We note that MDI measures the continuum intensity in the vicinity of the Ni I 6768Å line, which is different from the broad-band continuum data obtained from the simulations. This might be a source of some of the divergences between the model and the observations.

We use the numerical code to make a physically realistic three-dimensional simulation of the shallow upper layers of the solar convective zone. We have generated data for 72 hours of solar time, which provide 3.86 μ Hz frequency resolution. We calculate power spectra of the velocity and intensity and their phase differences to study properties of the oscillations generated in this simulation box. In the simulation, the first set of nonradial modes corresponds to a harmonic degree $\ell = 740$ (or $k_h = 1 \text{ Mm}^{-1}$), the second set corresponds to $\ell = 1480 \ (k_h = 2 \text{ Mm}^{-1})$ etc. In the numerical model, the vertical component of velocity, V(x, y, t), is calculated at a height of 200 km above the $\tau = 1$ surface, close to the formation height of the observed MDI Doppler velocities. The simulated continuum intensity (the emergent continuum specific intensity), I(x, y, t), is calculated by solving the Feautrier equation along a vertical ray, in LTE, using a multigroup method to approximate the non-grey opacity. To extract the nonradial modes we multiply V(x,y,t) and I(x,y,t) by $\sin(k_x x)$, $\sin(k_y y)$, $\cos(k_x x)$ and $\cos(k_y y)$, where k_x or k_y are horizontal wave numbers equal to

 $2\pi n/L$, where L=6 Mm is the horizontal dimension of the simulation box (the same for both x and y directions), and n=1,2,3,... is the number of nodes in horizontal direction. Then we average the products of V and I with these sines and cosines over the horizontal planes. This corresponds to the 2-dimensional Fourier transform of the data with specific horizontal wave numbers. We then take Fourier transforms in time to obtain the power spectra, $\tilde{V}(k_x,k_y,\omega)$ and $\tilde{I}(k_x,k_y,\omega)$, and sum these four different spectra to obtain a power spectrum for a particular horizontal wave number $k_h^2 = k_x^2 + k_y^2$. This corresponds to summing the observational power spectra over azimuthal degree m. Since the line profiles for $k_h=2$ Mm⁻¹ ($\ell=1480$) and higher are rather noisy, we present the results for $k_h=1$ Mm⁻¹ ($\ell=740$) only. The $k_h=1$ Mm⁻¹ spectra are obtained either for $n_x=1$ and $n_y=0$ or $n_x=0$ and $n_y=1$. The modulus and phase of the cross spectra $\tilde{I}\tilde{V}^*$ give the coherence and phase difference between intensity and velocity.

3.3 Comparison between the Observed and Simulated Power Spectra

In Figures 1 and 2 we compare the observed and simulated mode power spectral densities in velocity and intensity for $\ell = 740$. The observational data represent 5 days of the observations of a quiet-sun region with a spatial resolution of 2 arcsec/pixel ($\sim 1,500 \text{ km}$) and temporal resolution 1 min. The simulation data are for the lowest non-radial mode of the same angular degree, $\ell = 740 \text{ (}k_h = 1 \text{ Mm}^{-1}\text{)}$ calculated from a 72 hour run with a horizontal grid spacing of 100 km and time spacing of 0.5 min. In order to make our comparison more appropriate, we took only 72 hours of the observational data and every other snapshot in the simulated data to have the same

1 min time step as in observations. The simulated and observed velocity power are similar to each other. The simulation power falls off more rapidly at high frequencies, both in velocity and frequency, probably due to numerical damping in the simulation. The frequency separation between the simulated modes is larger than the separation between the observed modes because of the shallow computational domain. It is only 2.5 Mm deep, whereas $\ell=740$ modes in the Sun have the turning points below ~ 4 Mm. As a result, the resonant frequencies in the simulation are different from the frequencies of solar modes. Also, due to the shallow domain, the simulated modes have less inertia than the solar modes. Because of the smaller inertia (mode mass) the damping rate is much larger in the simulation than the Sun, so the simulated line profiles are broader than the observed ones. However, these differences do not prevent us from studying the mode physics with the numerical simulations.

The lowest frequency mode in the power spectra is the f mode, which is essentially a surface gravity mode. It does not exist in radial oscillations, but in the nonradial data, it is very strong and shows the same asymmetry behavior as do p modes. Interestingly enough, in the simulations the amplitude of the f mode is greater than the amplitudes of the p modes, whereas in the observational data the f-mode amplitude is smaller than the amplitude of the p_1 mode.

For both the simulations and the observations the velocity and intensity line profiles are clearly asymmetric, with opposite asymmetries in velocity and intensity (Figures 1 and 2). Also, the slopes of the power spectra in velocity and intensity have a power law behavior in both the simulation and observations.

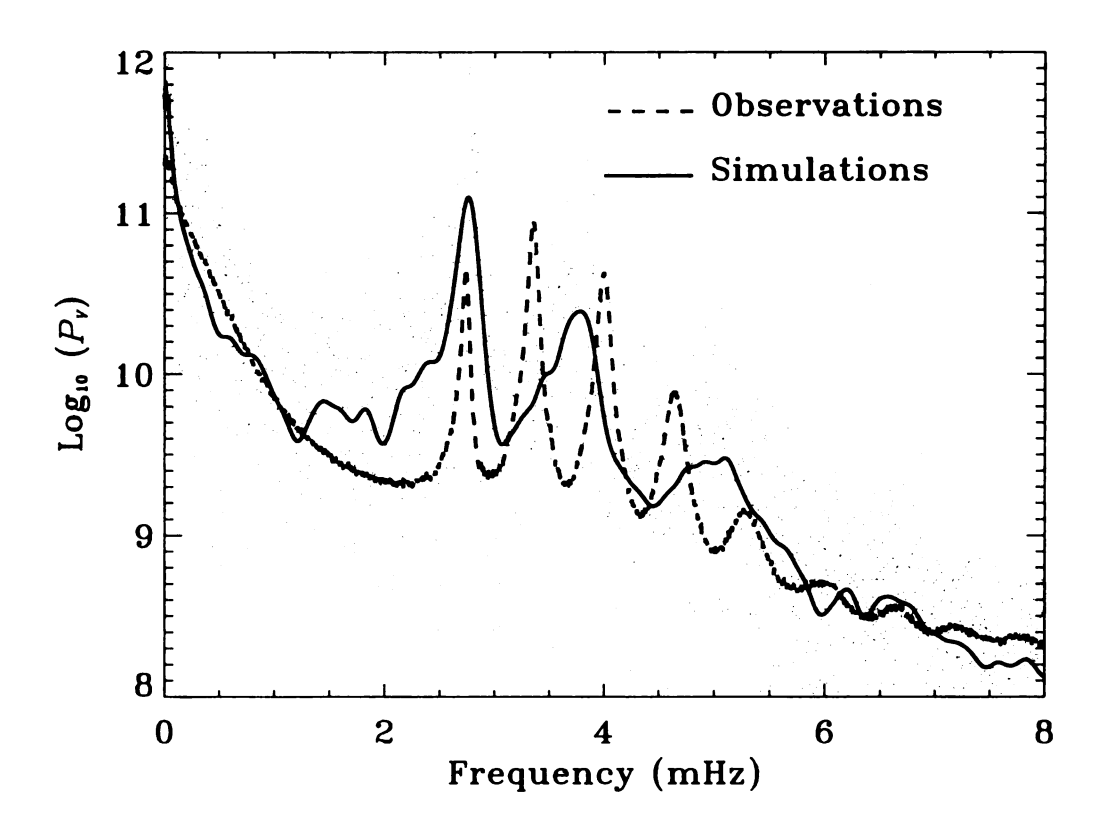


Figure 1. Observed and simulated power spectra of velocity for $\ell=740$ from the SOHO/MDI and for the first non-radial mode (with a 6 Mm horizontal wavelength) from a 72 hour simulation of solar surface convection on a 6 Mm \times 6 Mm \times 3 Mm deep domain. Observed velocities are from the Doppler shifts of the NiI 6768 Å line summed over all $m=2\ell+1$ modes. Velocity power spectral density is in units of $(cm/s)^2/Hz$. The simulated modes are sparser and broader than the observed modes because the simulated domain is shallower than the turning points of the observed modes, resulting in a smaller mass for the simulated modes.

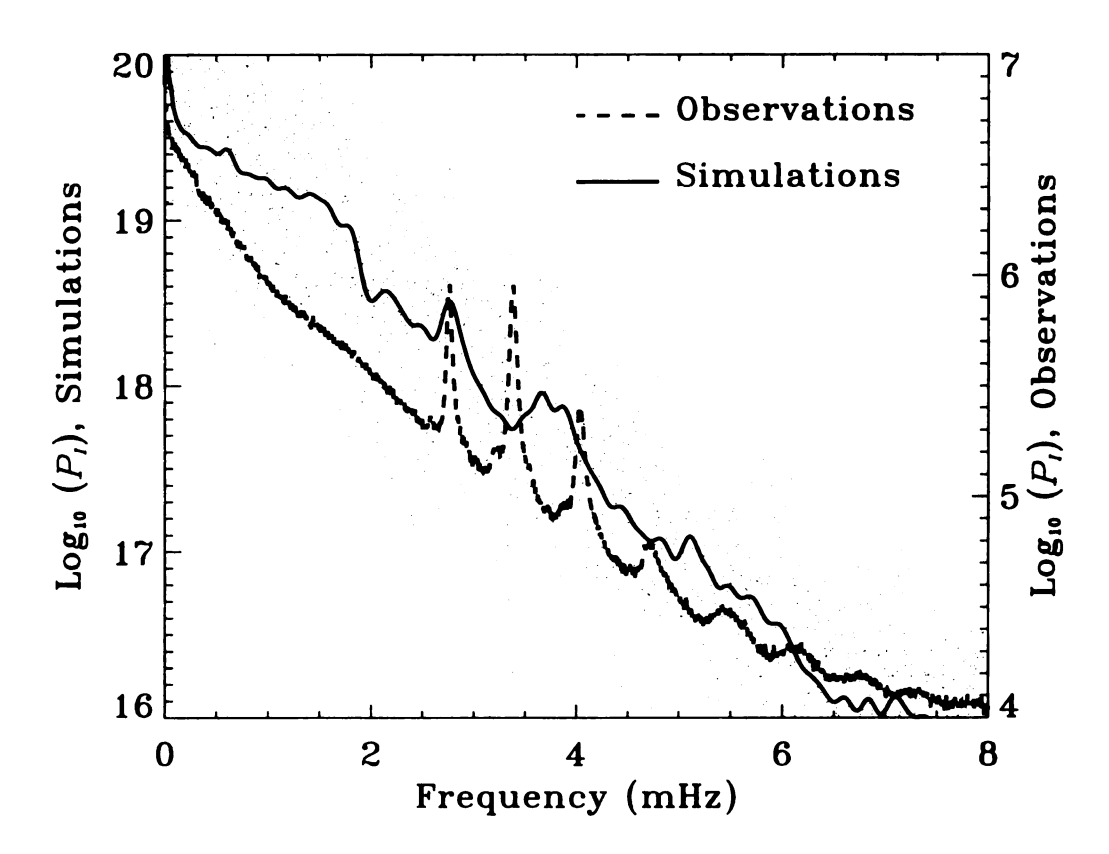


Figure 2. Observed and simulated power spectra of intensity for the same cases as the velocity in figure 1. Observed intensity is from the NiI 6768 Å line summed over all $m = 2\ell + 1$ modes. Observed intensity power spectral density is in units of (CCD counts per sec)²/Hz. Simulated intensity is from the solution of the transfer equation along a vertical ray. Simulated intensity power spectral density is in units of $(erg/cm^2/s/ster)^2/Hz$.

3.4 Intensity - Velocity Phase Difference

Figure 3 compares the observed and simulated phase differences between the intensity and velocity signals, I-V, as a function of frequency. Both the observations and simulations have negative phase difference I-V at low frequency. In both cases, the phase difference departs from the 90° phase difference predicted by the adiabatic theory of trapped standing waves. In both cases, there are jumps in phase of $\sim 90^\circ$ at the mode frequencies. The phase differences approach zero for high frequency propagating waves as expected for adiabatic acoustic waves.

3.5 Conclusions

In this chapter, we have compared observed asymmetries of the oscillation line profiles in the velocity and intensity power spectra with those obtained in 3D hydrodynamic simulations of solar convection. The basic characteristics of the observed mode peak asymmetries are reproduced in the simulations: the modes are asymmetric, with the velocity and intensity having opposite asymmetries. The reversal in asymmetry occurs in the intensity signal (possibly due to the process of radiative transfer, which causes additional signal in the intensity fluctuations correlated with the oscillation). This is an important step in studying the physical properties of solar oscillations and their interaction with turbulence. The basic characteristics of the observed intensity – velocity phase difference are also reproduced in the simulations. The similarity of the oscillation mode properties in the simulation and observations means that the simulations can be used to investigate the origin of mode behavior.

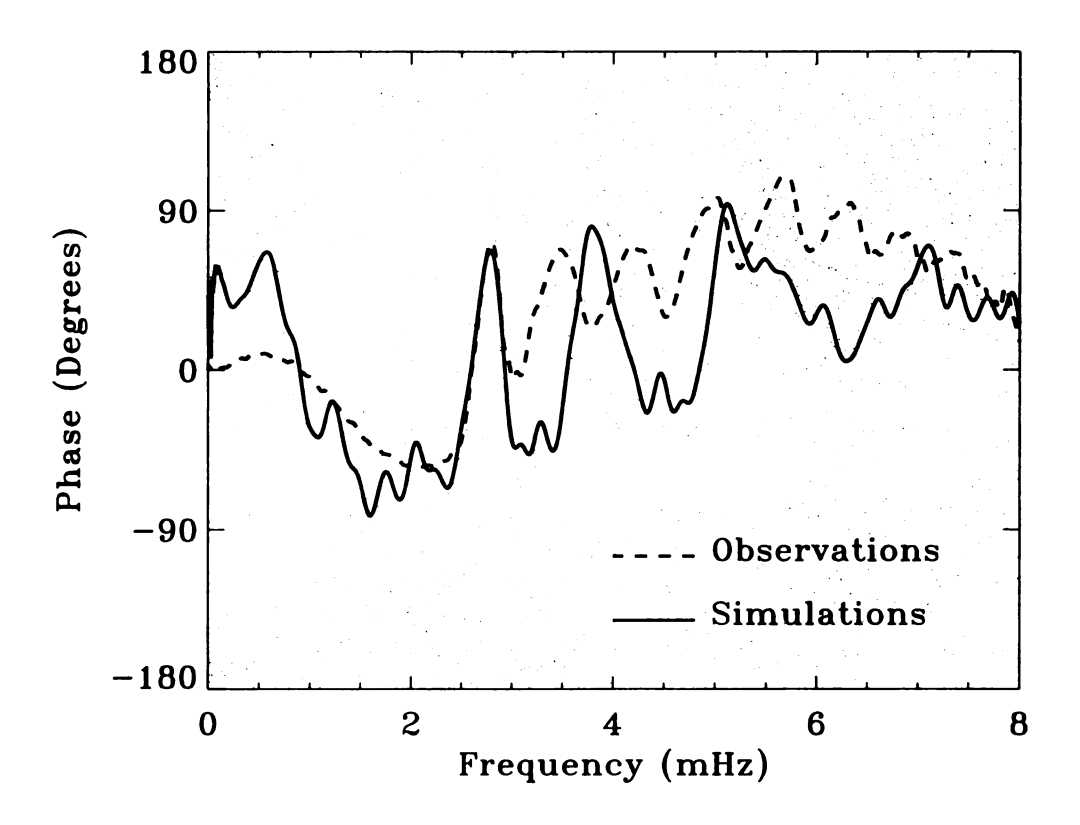


Figure 3. Observed and simulated intensity – velocity phase difference. Observed data is from SOHO/MDI with $\ell=740$ summed over all $m=2\ell+1$ values. Simulated data is for the first non-radial mode (with horizontal wavelength 6 Mm). The phase jumps $\sim \pi/2$ at the modes where the oscillation amplitude is large.

Chapter 4

ROLE OF RADIATIVE TRANSFER IN THE ASYMMETRY REVERSAL

The solar acoustic p-mode line profiles are asymmetric. Velocity spectra have more power on the low-frequency sides, whereas intensity profiles show the opposite sense of asymmetry. The mode asymmetry problem is important for accurate frequency determination, especially for resolving the existing discrepancies between the observed and predicted mode frequencies. Studies of the asymmetry give insight into convection - oscillation interaction, particularly, mode excitation by convective sources. Numerical simulations of the upper convection zone have resonant p-modes with the same asymmetries and asymmetry reversal as the observed modes. The temperature and velocity power spectra at optical depth $\tau_{\rm cont} = 1$ have the opposite asymmetry as is observed for the intensity and velocity spectra. At a fixed geometrical depth, corresponding to $<\tau_{\rm cont}>=1$, however, the temperature and velocity spectra have the same asymmetry. This indicates that the asymmetry reversal in the simulation is produced by radiative transfer effects and not by correlated noise. The cause of this reversal is the non-linear amplitude of the displacements in the simulation and the non-linear dependence of the H⁻ opacity on temperature. Where the temperature is hotter the opacity is larger and photons escape from higher, cooler layers. This

reduces the fluctuations in the radiation temperature compared to the gas temperature. The mode asymmetry reversal in the simulation is a small frequency dependent differential effect within this overall reduction. Because individual solar modes have smaller amplitudes than the simulation modes, this effect may be smaller on the Sun.

4.1 Introduction

For almost a decade, it has been known that the power spectra of solar acoustic modes are asymmetric, velocity has more power on the low frequency side and intensity has more power on the high frequency side of the power maxima (e.g. Duvall et al. 1993a). The asymmetry reversal between velocity and intensity is thought to be due to the correlated background noise contribution to the intensity power spectra (Nigam et al. 1998). It is debated whether the asymmetry reversal occurs in velocity (Roxburgh & Vorontsov 1997) or intensity (Nigam et al. 1998) or both (Kumar & Basu 1999). Theoretical models predict asymmetries that depend on the source depth and type (Kumar & Basu 1999; Georgobiani et al. 2001). Roxburgh & Vorontsov (1997) considered the superposition of dipole and quadrupole sources; Nigam et al. (1998) used a combination of monopole and dipole terms; Kumar & Basu (1999) show that the asymmetry reversal could be triggered even by dipole or quadrupole sources alone.

Simulations of the shallow upper layer of the solar convective zone have resonant acoustic modes like the Sun. The emergent intensity and the velocity in the photosphere have asymmetric spectra with the opposite asymmetry (Georgobiani et al.

2000). In this chapter we calculate the temperature and velocity power spectra at the continuum optical depth $\tau=1$ and at the geometrical depth corresponding to $<\tau>=1$. At unit continuum optical depth the velocity and temperature have opposite asymmetry, with the velocity having more low-frequency power and the intensity more high frequency power. At fixed geometrical depth, however, the velocity and temperature have the same asymmetry, more low frequency power, for the fundamental mode. These results indicate that the asymmetry reversal is caused by radiative transfer effects (Georgobiani et al. 2003).

4.2 Theory of Correlated Noise

Mode asymmetry in the spectral domain is a result of the interference pattern of waves from a localized source not being symmetrical relative to the mode resonant frequencies. Constructive and destructive interference occurs between waves from the source that propagate outward with those that propagate inward and are refracted outward. Destructive interference causes characteristic "troughs" on one side of the modal lines, where the amplitude is minimal. The frequencies of the "troughs" depend on the source location and type (Duvall et al. 1993a; Vorontsov et al. 1998; Nigam & Kosovichev 1999). In the solar case, the destructive interference occurs at frequencies slightly higher than the resonant frequencies. This corresponds to the negative line asymmetry. The interference pattern may be also affected by the presence of an additional signal correlated with the source. Variations of the continuum intensity in the convective granules, which are associated with the process of excitation of solar oscillations, are such a signal (Nigam et al. 1998). This correlated signal shifts

the frequencies of the "troughs". If the correlated signal is sufficiently strong the "troughs" may be shifted to the other side of the mode resonant frequencies, and thus reverse the asymmetry of the modal lines. This reversal of the asymmetry is observed in both the MDI intensity data and the intensity spectra obtained in the numerical simulations. The numerical results allow us to verify that variations in the background intensity in the granules are indeed correlated with the observations (Nordlund & Stein 1998). In the MDI Doppler velocity measurements this correlated variation is essentially cancelled by taking differences of values on opposite sides of the line. In the intensity measurement it is enhanced by summing contributions from opposite sides of the line. The correlated component of the noise must be large enough to reverse the asymmetry in the intensity power spectrum, but not sufficiently large to reverse the asymmetry in the velocity power spectrum (Nigam et al. 1998).

These results are consistent with the observations of Goode et al. (1998), where it appears that the acoustic events occur in cool and narrow intergranular dark lanes. Prior to an acoustic event there is darkening in the intensity. This darkening is also correlated to the strength of the event. Strong events are preceded by longer darkening. The reversal of asymmetry in intensity due to a correlated background has been confirmed by Kumar & Basu (1999) and Rast (1999). However, there is, as yet, no complete theory of the influence of the background variations on the observed properties of solar oscillations.

The variations of the phase difference between the intensity and velocity signals with frequency can also be explained by the presence of the correlated noise (Nigam

& Kosovichev 1999). The intensity - velocity cross spectrum is the product

$$C_{I-V} = (\delta I + N_I)(\delta V + N_V)^* + N_{Iuncorr}N_{Vuncorr}$$

and the intensity - velocity phase difference is

$$\tan \Theta_{I-V} = \Im C_{I-V} / \Re C_{I-V} .$$

Away from a mode the noise contribution dominates, while at an eigenfrequency the mode amplitude is large and dominates. If the intensity and velocity are nearly 90° out of phase, as they are expected to be for adiabatic waves, then they will contribute primarily to the imaginary part in the numerator, but have little effect on the denominator. At the mode eigenfrequency there will be a large jump in mode amplitude, producing a large jump in the ratio $\tan \Theta_{V-I}$, and hence a change in Θ of order $\sim 90^{\circ}$.

The phase and asymmetry behavior of the modes constrains the nature of the excitation mechanism of solar oscillations.

4.3 Calculations of Power Spectra and Phase Relations

We compare power spectra of intensity, temperature and velocity in order to shed light on a cause of the p-mode line profile asymmetry and its reversal between velocity and intensity. From our simulations, we have coordinate- and time-dependent quantities: vertical velocity V(x, y, z, t), temperature T(x, y, z, t), emergent intensity I(x, y, t), etc. To obtain a power spectrum at a particular geometrical depth z_0 , we use V and T at $z=z_0$. To obtain V and T at a particular optical depth, say, $\tau=1$, we calculate $\tau(x,y,z,t)$ and interpolate V and T to the height at which $\tau(x,y,z,t)=1$ for each position (x,y) and time t. We choose z_0 to be the depth for which $<\tau>=1$. Clearly, V(x,y) or T(x,y) at a geometrical depth z_0 will not be the same as V(x,y) or T(x,y) at $\tau=1$: we see deeper in the cooler intergranular lanes compared to the hotter granules. We investigate if this makes a difference in the power spectra and somehow affects line asymmetries.

We separate the oscillation modes into radial modes, for which we average our data horizontally, and non-radial modes, for which we multiply the data by the corresponding spatial sines or cosines and then average horizontally (for more details, see Georgobiani et al. (2000)). We then Fourier - transform these time strings to get power spectra and phase relations. In our simulations, the first non-radial mode (horizontal wavelength $\lambda_h = 6$ Mm) corresponds to a harmonic degree $\ell = 740$, because the simulation box represents a small fraction of the solar surface. We investigate the behavior of the emergent intensity, plasma temperature and plasma velocity for this first non-radial mode of the simulation (see also Georgobiani et al. 2000).

4.4 Results

The emergent continuum intensity (Fig. 4) is a good measure of the plasma temperature at local instantaneous continuum optical depth unity, $\tau(x, y, t) = 1$, as expected from the Eddington-Barbier relations. The temperature at $\tau = 1$ has the same

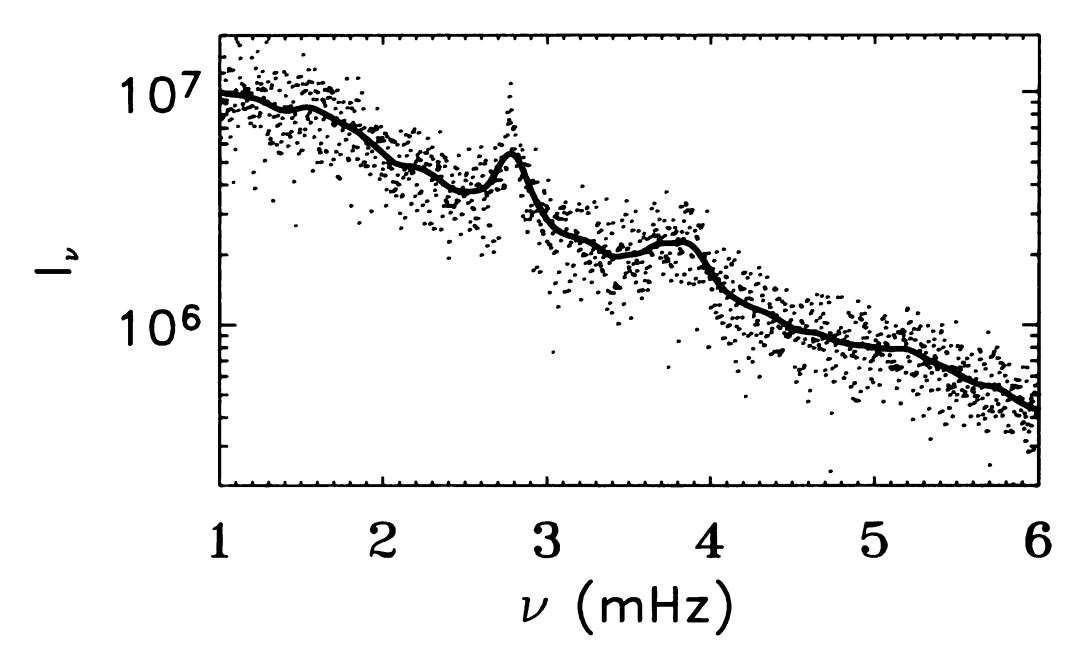


Figure 4. Spectrum of intensity, I_{ν} , in erg cm⁻² s⁻¹ sterad⁻¹. The solid curve is smoothed over $\Delta \nu = 0.23$ mHz.

spectrum (Fig. 5) and phase (Fig. 6) as the emergent intensity. These phase differences are essentially zero for all frequencies. The spectra of the emergent intensity and plasma temperature at $\tau=1$ have opposite asymmetry to the plasma velocity (Fig. 7) as is observed (e.g. Duvall et al. 1993a) and as was discussed by Georgobiani et al. (2000). The spectrum of the temperature at fixed geometrical depth z_0 , corresponding to the average continuum optical depth unity, $\langle \tau \rangle_{x,y,t}=1$, (Fig. 8) is, however, rather different from its spectrum at local instantaneous unit optical depth (Fig. 5), with different asymmetries especially noticeable for the fundamental mode. The temperature at $\langle \tau \rangle = 1$ has the same asymmetry as the velocity.

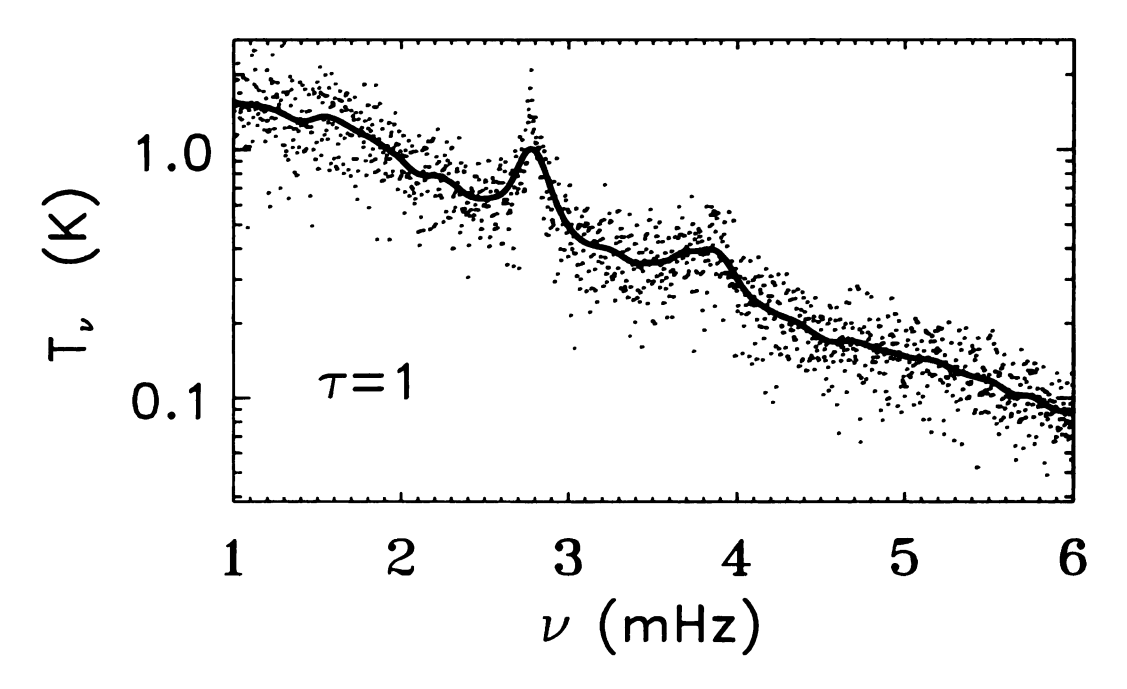


Figure 5. Spectrum of temperature, T_{ν} , at $\tau(x,y,t)=1$. Again, the solid curve is smoothed.

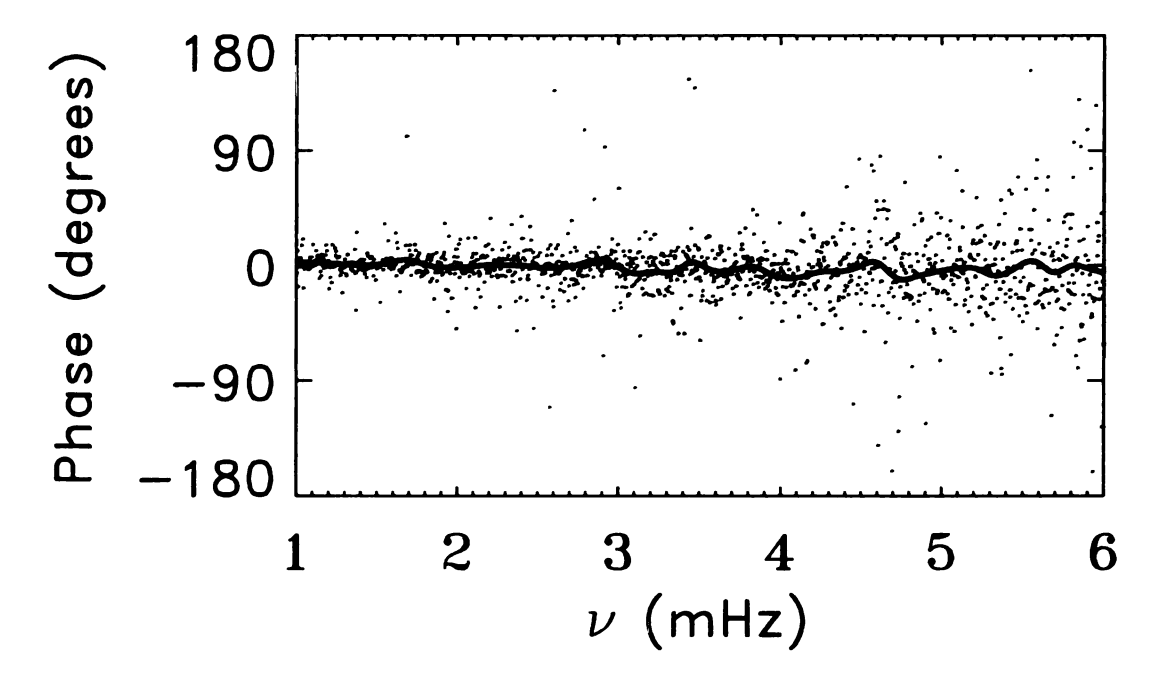


Figure 6. Phase difference between the intensity and the temperature measured at the $\tau = 1$ level.

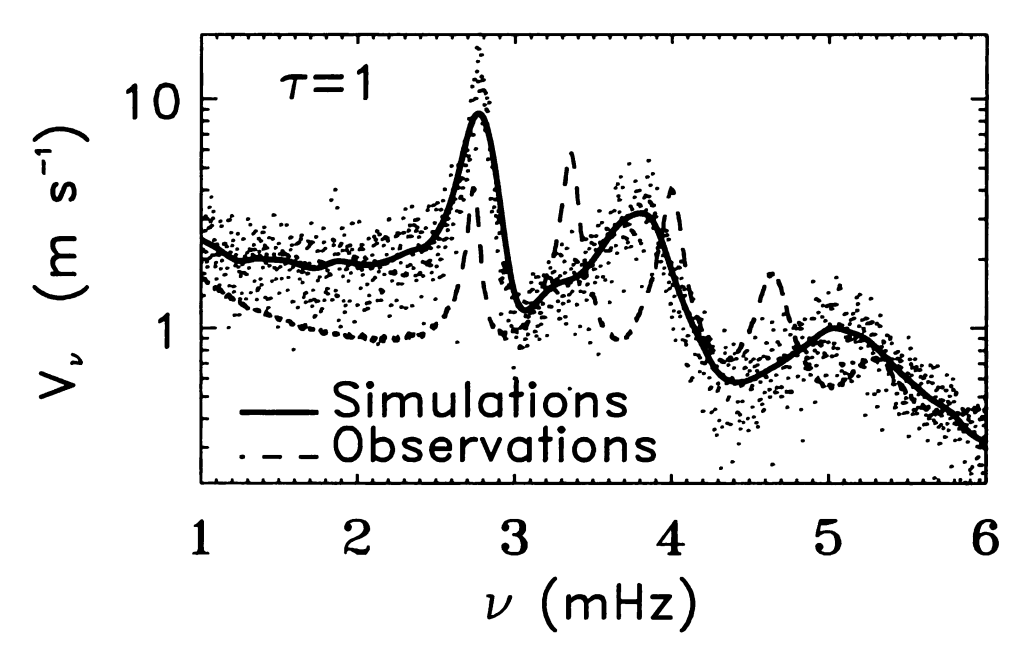


Figure 7. Spectrum of velocity, V_{ν} , at $\tau(x,y,t)=1$. Its spectrum is almost the same at fixed geometrical depth corresponding to $\langle \tau \rangle_{x,y,t}=1$. Observed Doppler velocity spectrum is plotted for comparison.

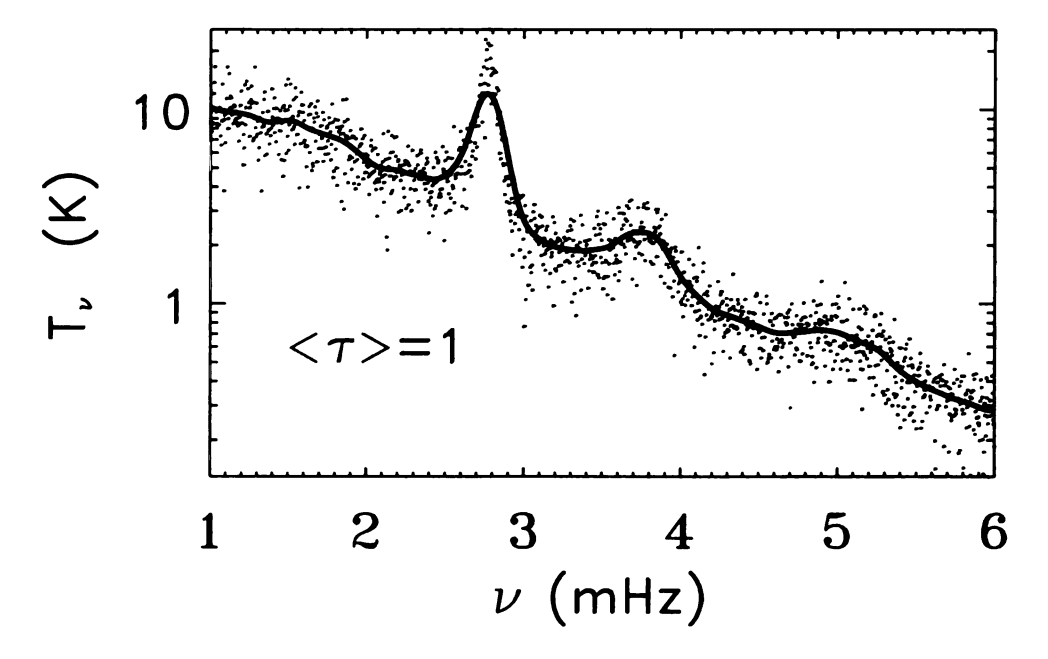


Figure 8. Spectrum of temperature, T_{ν} , at $<\tau>=1$. The temperature at $<\tau>=1$ has the same asymmetry as the velocity.

4.5 Discussion

What changes the asymmetry of the temperature spectrum between measuring it at $\log 2\tau = 1$ and average $<\tau>=1$? We analyze the first non-radial fundamental mode that has the most prominent asymmetry and agrees closely with the corresponding solar $\ell=740$ mode. Figure 9 shows the velocity and temperature profile of this mode at average continuum optical depth one. It is clear that the velocity and temperature have similar profiles. Figure 10 shows the velocity and temperature profiles measured at local optical depth one, which is where one would see them. The velocity spectrum is hardly changed, but the amplitude of the temperature fluctuations is reduced by almost an order of magnitude. The high temperature sensitivity of the H^- opacity obscures high temperature gas and alters the height at which the gas is observed. This reduces the magnitude of the observed temperature fluctuations, but this reduction is not as great on the high frequency side as on the low frequency side. Hence, the mode asymmetry is changed.

Why is the reduction of the temperature fluctuations different at high and low frequencies? At the fixed geometrical height $\langle \tau \rangle = 1$, the temperature fluctuations were larger on the low frequency side of the mode. This produces a larger opacity variation on the low frequency side of the mode (Fig. 11), which in turn leads to a larger variation in the height where local $\tau(x,y,t)=1$ (Fig. 12). The radiation temperature we see is equal to the gas temperature at optical depth unity, according to the Eddington-Barbier relations. The phases of temperature and height of unit optical depth are such that where the temperature at fixed geometrical depth

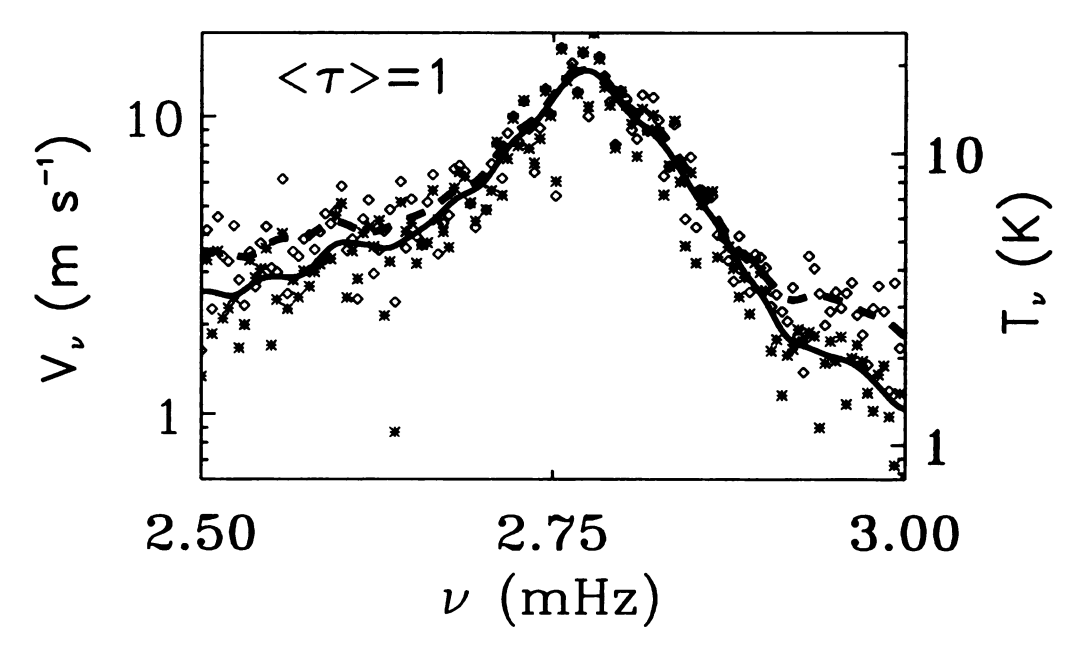


Figure 9. The temperature (dashed) and velocity (solid) spectrum for the first non-radial fundamental mode measured at $<\tau>=1$. Here and after, diamonds represent unsmoothed temperature profiles, whereas stars correspond to the parameter on the left y-axis. The temperature and velocity profiles look similar to each other. Curves are smoothed over 38.6 μ Hz.

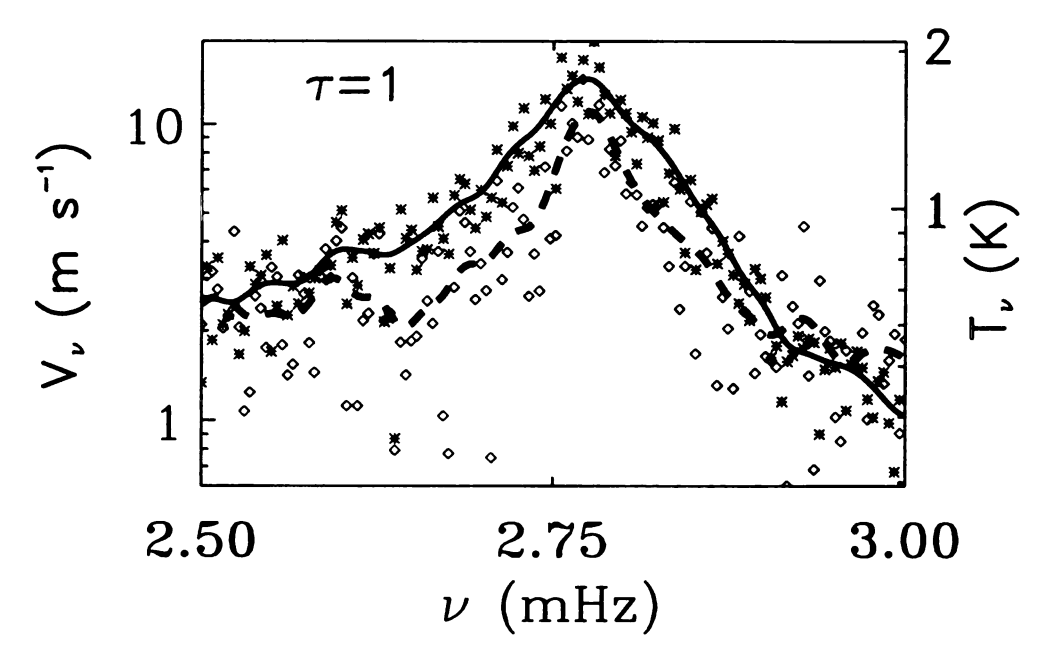


Figure 10. The temperature (dashed) and velocity (solid) spectrum for the first non-radial fundamental mode measured at $\tau = 1$. The amplitude of the temperature fluctuations is nonuniformly reduced across the mode peak.

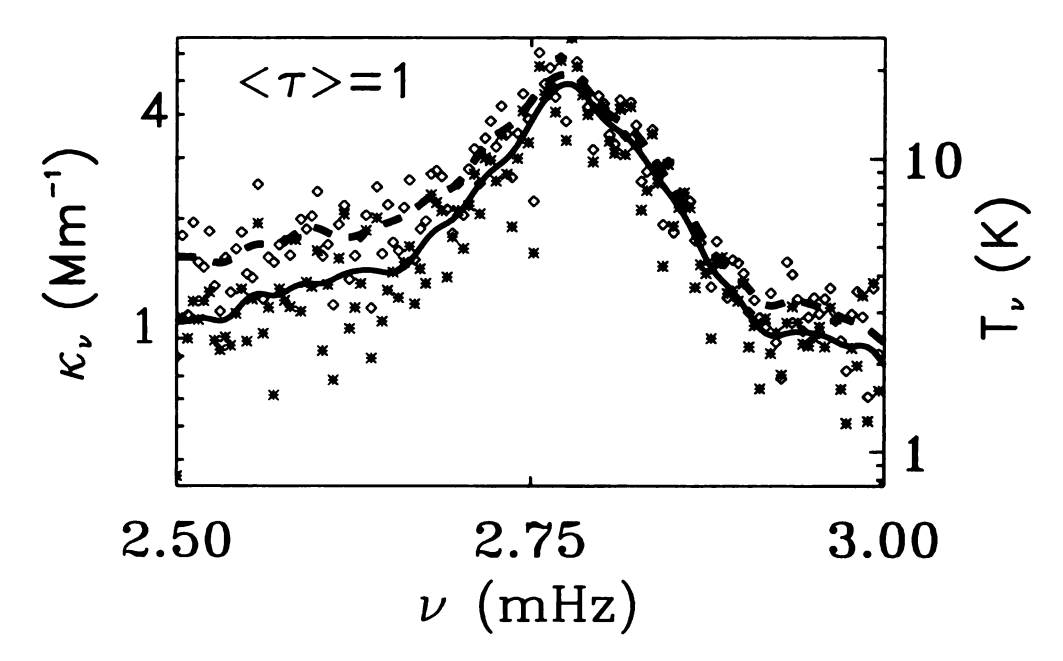


Figure 11. The temperature (dashed) and opacity (solid) spectrum for the first non-radial fundamental mode measured at $<\tau>=1$. The larger temperature fluctuations on the low frequency side of the mode produce larger opacity variations.

is largest we observe the temperature at greatest height (smallest z) (Fig. 13). Since the gas temperature is decreasing outward, the larger variation in the location where the radiation originates on the low frequency side of the mode leads to a smaller temperature variation there, while the smaller variation in the location where radiation originates on the high frequency side of the mode leads to a larger temperature variation there. We therefore observe a larger intensity variation on the high frequency side of the mode and thus the asymmetry is reversed from that observed in the velocity (and temperature when measured at a fixed geometrical depth).

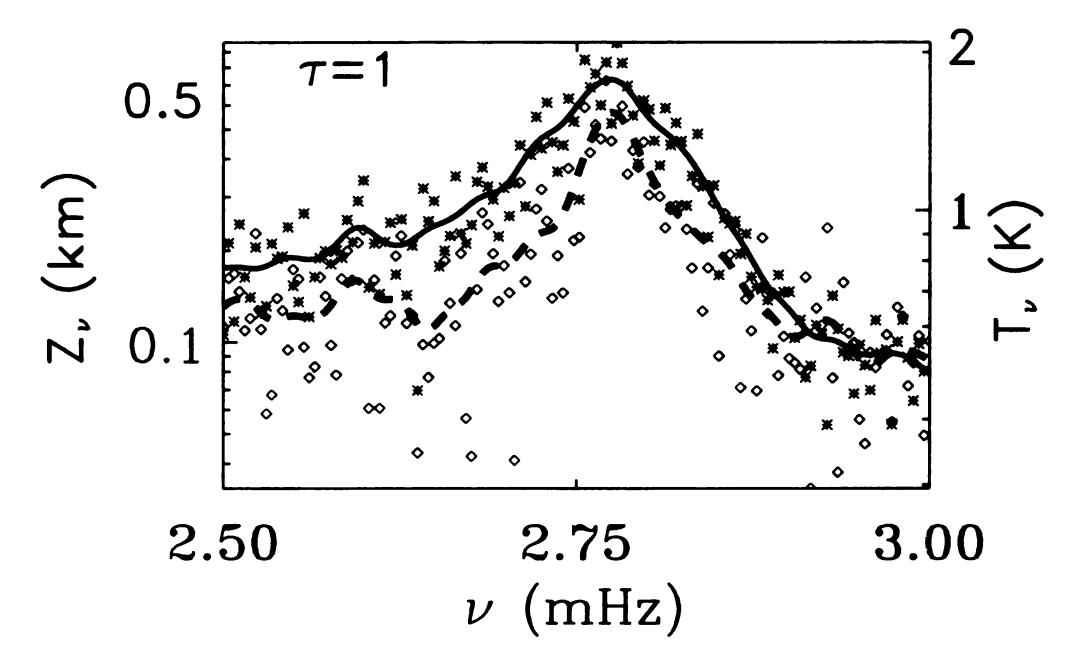


Figure 12. The spectrum of the height of local optical depth one, $z_{\tau(x,y,t)=1}$, (solid) and temperature (dashed) measured at local $\tau=1$. The location of local optical depth unity varies more on the low frequency side of the mode, where the opacity variation is larger due to the larger temperature fluctuations. This reduces the temperature fluctuations at local optical depth unity more on the low frequency side of the mode compared to the high frequency side and, in accordance with the Eddington-Barbier relations, leads to smaller intensity fluctuations on the low frequency side of the mode and larger intensity fluctuations on the high frequency side of the mode.

4.6 Conclusions

We have found that the emergent intensity and the temperature spectra at local instantaneous optical depth unity have the *opposite* asymmetry to the velocity as is observed, while the temperature at fixed geometrical depth corresponding to average optical depth unity has the *same* asymmetry as the velocity. This indicates that radiation transfer plays a crucial role in the asymmetry reversal observed between the intensity and Doppler velocity in the simulation, and that this reversal is not due solely to effects of correlated noise.

The asymmetry reversal in the simulation is due to several non-linear effects: first, the displacement of the atmosphere by the oscillations and convection is significant. Although the amplitudes of the individual solar p-modes are very small and in the linear regime, the total displacement from all the motions is tens of kilometers and not linear. The individual modes in our simulation have larger amplitudes. There are only four of the individual modes in the simulation for $\ell = 740$ vs. 1481 different azimuthal values on the Sun, while their total displacement is comparable to the Sun (Fig. 7). Because the mode displacements are smaller on the Sun their effect on reversing the mode asymmetry will also be smaller. Second, the H⁻ opacity is a non-linear function of the temperature. The mode asymmetry has been shown to depend on the separation of observation location and source location for the case of a simple localized δ -function source (Kumar & Basu 1999; Georgobiani et al. 2001), and $T(\tau = 1)$ and $T(<\tau>=1)$ are observed at different heights. Oscillation induced opacity changes vary the location of radiation emission ($\tau = 1$) in a way that

reduces the magnitude of the temperature fluctuations and reverses their asymmetry. The radiation temperature fluctuations equals the gas temperature fluctuations at local optical depth unity are reduced by an order of magnitude with respect to the temperature fluctuations at a fixed geometrical height $\langle \tau \rangle = 1$. This reduction is due to the highly non-linear dependence of the H⁻ opacity on temperature, so that where the temperature is hotter the opacity is larger and photons escape from higher, cooler layers. Because of this non-linear dependence of the emergent intensity on the atmospheric displacement, it is not possible to consider an individual mode's effect in isolation from the other motions. What we have found is a small differential effect that reverses the temperature asymmetry as part of a larger overall reduction in the magnitude of the temperature fluctuations.

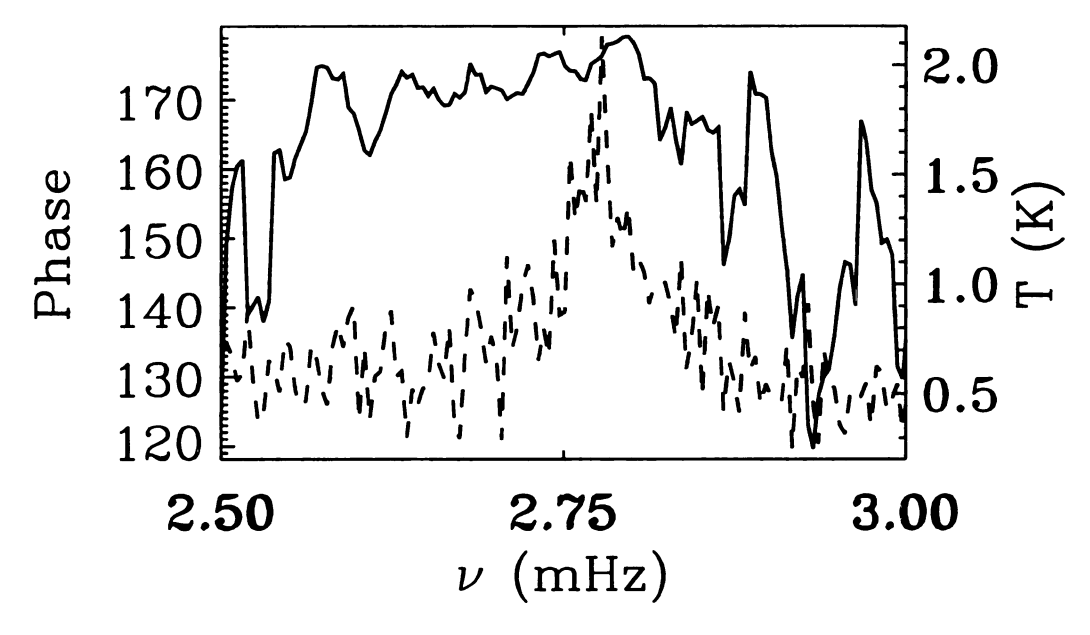


Figure 13. The phase (solid line) between the height of $\tau=1$ and the temperature at $<\tau>=1$. Phase $\approx 180^{\circ}$ means that the height of unit optical depth is greatest (smallest z and lowest temperature) when the temperature at $<\tau>=1$ is largest. Also shown is temperature at $\tau=1$ (dashed).

Chapter 5

SOURCE DEPTHS AND ASYMMETRIES

Mode asymmetries reflect the underlying physics of excitation and provide information about location and types of sources. The asymmetry of the mode profiles varies with depth. At the surface, the velocity asymmetry is the same as in the SOHO/MDI observations, but deeper down it becomes flipped in comparison to the surface asymmetry. This behavior can be reproduced by a simple model of a potential well with a delta-source inside or outside it. Varying the source depth and comparing the asymmetric profiles of the resulting power spectra with the simulation spectra, one can determine the depth of mode driving for different frequencies and heights.

5.1 Introduction

We study p-mode asymmetry behavior with depth. The asymmetry of p-modes at the surface is similar to the observed asymmetry, but it reverses below the surface and becomes completely flipped around 1 Mm deep. We construct simple 1D models to study this effect. Then we compare the simulation mode profiles and profiles resulting from these simple models.

5.2 Simple Analytical Models

To investigate the behavior of the line profile asymmetry, we calculate velocity (or kinetic energy) power spectra at different depths in the simulation box. Figure 14 depicts the results of such calculations for the radial modes. One can see that line asymmetry becomes reversed with depth. The reversal takes place somewhere around 0.5 Mm below the $\tau=1$ surface; at 1 Mm below the surface, the asymmetry is completely reversed (upper graph). However, line profiles integrated over the depth seem to be more symmetric (lower graph). Subtraction of the background noise using Nigam's fitting formalism (Nigam & Kosovichev 1998) does not change the qualitative picture. One can argue that the reversal is an intrinsic property of modes and it does not depend on the background noise.

We have constructed a simple 1D potential well model (cf Abrams & Kumar 1996 and references therein). We consider the wave equation

$$\frac{d^2\Psi_{\omega}}{dr^2} + [\omega^2 - V(r)]\Psi_{\omega} = \delta(r - r_s). \tag{1}$$

Here, Ψ_{ω} is proportional to the fluid displacement, r_s is a δ -source location and V(r) is a simple potential:

$$V(r) = \infty, \quad r \le 0;$$

$$V(r) = 0, \quad 0 < r < L;$$

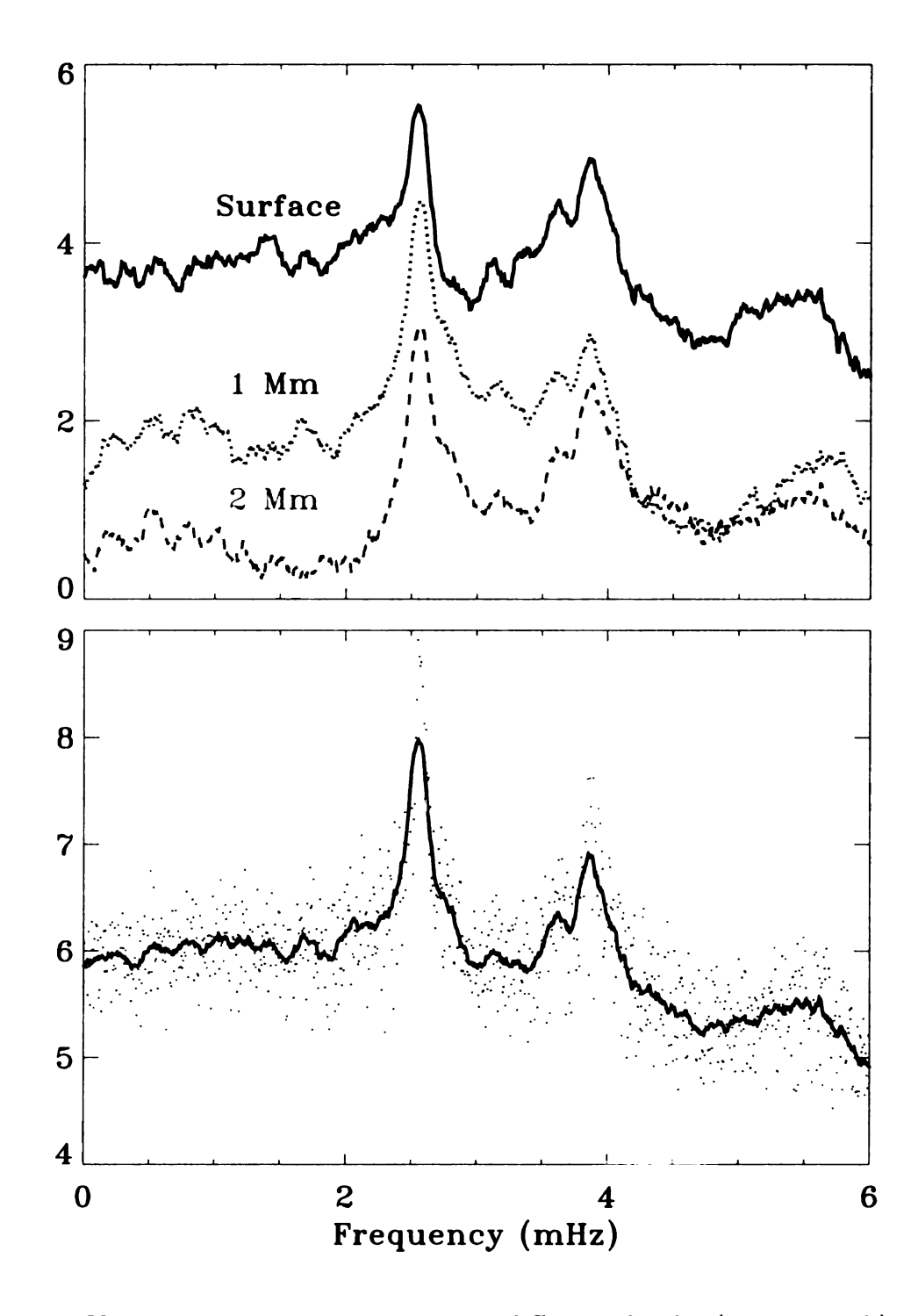


Figure 14. Kinetic energy power spectra at different depths (upper graph) and integrated over the depth (lower graph). Ordinates are logarithmic, with arbitrary units.

$$V(r) = \omega_{ac}^2, \quad r \ge L,$$

L is the width of the well, or depth of the resonant cavity (we take L=2.5 Mm, from the $\tau=1$ surface to the bottom of the simulation domain); ω_{ac} is the acoustic cutoff frequency at the temperature minimum. Sound speed is set to 1. Damping is not included in this simple model. We solve Eq. (1) analytically, for the source located either inside or outside the cavity, constructing wave functions in different regions and matching them at the boundaries and at the source. We obtain Green's functions in all layers for both the source inside and outside of the well. For the source inside the well, the solutions are

$$G_I^i = rac{-\kappa \sin \omega (L - r_s) - \omega \cos \omega (L - r_s)}{\omega [\kappa \sin \omega L + \omega \cos \omega L]} \sin \omega r$$

$$G_{II}^i = \frac{\sin \omega r_s [\kappa \cos \omega L - \omega \sin \omega L]}{\omega [\kappa \sin \omega L + \omega \cos \omega L]} \sin \omega r$$

$$-\frac{\sin \omega r_s}{\omega}\cos \omega r$$

$$G_{III}^{i} = \frac{-\sin \omega r_{s}}{\kappa \sin \omega L + \omega \cos \omega L} e^{-\kappa (r-L)}$$

Here, I is the region between 0 and r_s , II is between r_s and L and III is from L to infinity; $\kappa^2 = \omega^2 - \omega_{ac}^2$. For the source outside the well, the solutions look like

$$G_I^o = \frac{-e^{-\kappa(r_s - L)}}{\kappa \sin \omega L + \omega \cos \omega L} \sin \omega r$$

$$G_{II}^o = \frac{-e^{-\kappa(r_s - L)}[\kappa \sin \omega L - \omega \cos \omega L]}{2\kappa[\kappa \sin \omega L + \omega \cos \omega L]}e^{-\kappa(r - L)}$$

$$+ \frac{-e^{-\kappa(r_s-L)}}{2\kappa}e^{\kappa(r-L)}$$

$$G_{III}^o = \left[\frac{\kappa \sin \omega L \cosh \kappa (r_s - L)}{\kappa [\kappa \sin \omega L + \omega \cos \omega L]} \right]$$

$$+ \frac{\omega \cos \omega L \sinh \kappa (r_s - L)}{\kappa [\kappa \sin \omega L + \omega \cos \omega L]} e^{\kappa (L - r)}$$

In this case, I is the region between 0 and L, II is between L and r_s and III is from r_s to infinity.

It is interesting to see what part of solution is responsible for the line profile asymmetry (e.g. Abrams & Kumar 1996). Power spectra are proportional to the squared Green's functions, $P_{\omega}(r) \propto |G_{\omega}(r)|^2$ (one would have to include higher order terms for more complex sources with higher multiplicity). We see that all the Green's functions have a common denominator (multiplied by either ω or κ). We expand it in the vicinity of a resonant frequency ω_0 and use the eigenvalue condition $\kappa_0 \sin \omega_0 L + \omega_0 \cos \omega_0 L = 0$, where $\kappa_0^2 = \omega_0^2 - \omega_{ac}^2$. The result

$$d = \Delta (1 + \omega_0^2/\kappa_0^2)^{-1/2} [1 + L\kappa_0 - (1 - L\kappa_0)\omega_0^2/\kappa_0^2]$$

contains $\Delta = \omega - \omega_0$ and constants. Δ could be either positive or negative, but power spectra are proportional to always positive Δ^{-2} . All dependence of the power spectra on either the depth or the source location comes from the Green's functions' numerators. In order to closely investigate them, we construct the numerical analogue

of this model, plot the resulting power spectra as function of depth and vary the source location to see how it affects the solutions at different depths. For brevity, we consider only the case with the source inside the well (also it better matches the simulated profiles). We study the power spectra dependence on the source location for two source depths, 100 km and 500 km below the surface. We notice that the source location influences the location of the minima (cf Nigam et al. 1998). In the region III (above the surface), line profiles do not change with depth, but they depend on the source location: for example, p_1 mode is quite asymmetric for the shallower source and it becomes more symmetric for the deeper source (similar result was obtained by Abrams & Kumar (1996)). In the region II (between the source location and the surface), for the shallow source, there is still no change in the asymmetry behavior; for the deeper source, there is a drift of the minimum between p_2 and p_3 towards lower frequencies. In fact, this drift makes p_1 more asymmetric (similar to the shallow source location). Figure 15 depicts the region I (below the source). For the shallow source, minima are drifting toward the high frequencies, reversing the asymmetry sense for p_1 and making p_2 symmetric. For the deep source, the same drift takes place, but the minimum between p_2 and p_3 stays at the same frequency, so the lower frequency minimum just passes through this minimum, shifting toward high frequencies.

One can alter the depth of the source and then compare the profiles from the potential well with those from the simulation. This gives the information where the source of mode excitation could be located for each simulation box mode. Figure 16 (upper graph) presents this comparison. In order to better fit the profiles, we

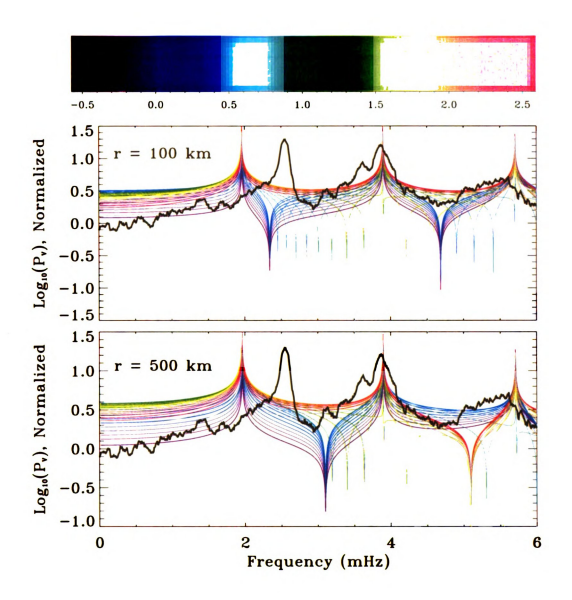


Figure 15. Well mode profiles in the region I (below the source). Lines become lighter with depth, and the thick line is the line profile measured at the surface. Profiles are different for different source locations, and their asymmetry changes with depth. Source locations are measured from the surface down. The ordinate is a normalized power. The colorbar indicates the sampling depth, in Mm, relative to the surface.

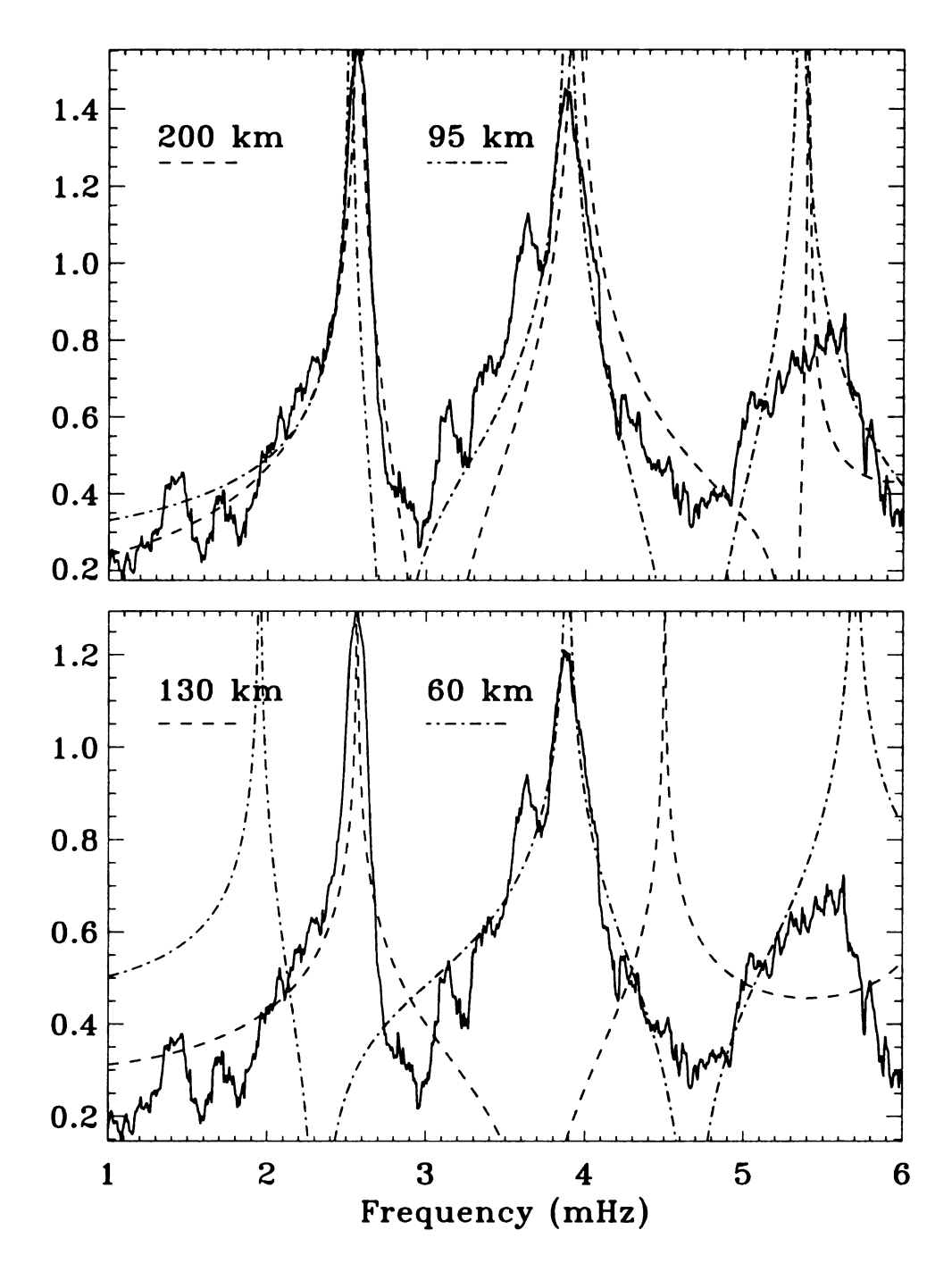


Figure 16. Comparison of the simulated velocity power spectra with the square well (upper part) and mean atmosphere potential (lower part). Different lines and numbers correspond to different source locations. Minima are matched at the high frequency ends of modes. Ordinates are in relative units. Model profiles were shifted in frequency for a better fit.

arbitrarily scale the well solutions and shift them in frequency. Such crude comparison gives the depth of the source location of 200 km beneath the surface for p_1 mode and 95 km for p_2 mode.

To make the simple model closer to the reality, we take the depth profiles of the sound speed and acoustic cutoff frequency from the mean simulation envelope and calculate power spectra for the 1D mean atmosphere potential instead of a rectangular well with constant sound speed and acoustic cutoff frequency. We conduct similar comparison with the 3D model (Figure 16, lower graph). Source depths appear to be even closer to the surface, 130 km for p_1 and 60 km for p_2 mode.

One should bear in mind that the models we use are indeed very simplified, and the δ -function source is utilized instead of a more sophisticated source or combination of sources with different multiplicity. The important result of our comparison is that the asymmetry reversal with depth could be accounted for in terms of simple models, with no damping or background noise involved.

5.3 Conclusions

Lower frequency modes are excited deeper in the convection zone. P-mode line profiles are found to be asymmetric in our numerical simulations, and the sense of asymmetry reverses with depth. The line profiles are more asymmetric for shallow source location, and they become more symmetric (or change the asymmetry sense) as the source moves deeper. The two last results can be reproduced using simplified 1D potential well models.

Chapter 6

SPECTRAL PROPERTIES OF TURBULENT CONVECTION

Recent observations support the theory that solar-type oscillations are stochastically excited by turbulent convection in the outer layers of the solar-like stars. The acoustic power input rates depend on the details of the turbulent energy spectrum. Investigating different assumptions about the stellar turbulent spectra and comparing theoretical estimates with observations, we gain more information on the characteristics of stellar turbulence and acoustic mode excitation and damping. There are large differences in stellar oscillation power calculated using different functional forms for the turbulence spectrum. Detailed numerical simulations together with high resolution ground observations (Swedish Solar Telescope, ATST) and space seismic missions (Solar B) will help to discriminate between various turbulent models.

6.1 Introduction

Acoustic power input to p-modes by turbulent convection has been modeled by several authors (Goldreich & Keeley 1977; Balmforth 1992; Goldreich et al. 1994; Samadi & Goupil 2001). On the basis of Lighthill's work (e.g. Lighthill 1952), mode excitation

rates can be written as

$$\frac{dE}{dt} = \frac{1}{M_{mode}} \int dr K(\omega, r) S(\omega, r),$$

where K is a kernel function proportional to the mode compression $\partial \xi_r/\partial r$ and S is the excitation source. The mode excitation rate is independent of the mode energy damping and so can be compared with observational determinations of the excitation rate found from measurements of the mode velocity amplitude at the surface and widths of the mode spectral peaks, $dE/dt = E\Gamma$, where Γ is the width of the mode spectral peak or the inverse of the mode damping time (Goldreich et al. 1994). After Stein (1967), it has been widely accepted that the turbulent source S which depends on the turbulent spectrum, is usually assumed to be separable into a spatial turbulent energy spectrum E(k) and a temporal turbulent spectrum $\chi_k(\omega)$:

$$S(\omega,m) \propto \int_0^\infty dk \, E(k) \, \chi_k(\omega).$$

The turbulent spectra in S are integrated over all wavenumbers k, and then S is integrated over the stellar mass M in calculations of the mean-square amplitude. Another approach is to calculate the temporal spectra at a characteristic wavenumber k_0 where the power is a maximum.

We show that the temporal components of the turbulent spectra are very different at different spatial wavenumbers k. Therefore, the turbulent energy spectrum is not separable into spatial and temporal factors.

The spatial and temporal turbulent spectra reveal the static (time-averaged) and dynamic properties of the stellar convection, especially relevant to the question of the acoustic mode excitation in stars. An universal property of turbulence is the existence of an inertial range of scales or wavenumbers $k_0 < k < k_d$ located between the basic energy input scale k_0^{-1} and the dissipation scale k_d^{-1} . In this range, the spatial spectrum of the velocity field is scale independent and therefore has a power law form (Monin & Yaglom 1975). It is expected from the theory of fully developed turbulence that the spatial turbulent energy spectrum E(k) should behave as $E(k) \propto k^{-5/3}$ according to Kolmogorov's scaling law (Kolmogorov 1941). Observations of the solar granulation are helpful in determining the solar turbulent spectrum. Solar observations confirm the existence of Kolmogorov cascade in a certain range of wavenumbers $k>k_0$ (Nesis et al. 1993; Espagnet et al. 1993). The small k region, prior to the turbulent cascade, the spectra seems to be a different power law. Espagnet et al. (1993) found a slope with the power of -0.7, while Nesis et al. (1993) found a slope of -5. According to Rieutord et al. (2000), differences at low wavenumbers between various observations of the solar granulation are a consequence of different data averaging techniques. Properties of the kinetic spectrum at low wavenumbers is not yet well determined by the observations of the solar surface. Nordlund et al. (1997) showed that the granulation spectrum does not provide a means for determining the turbulent properties. Musielak et al. (1994) proposed several models of the extension of the turbulent energy spectrum for wavenumbers smaller than k_0 : $E(k) \propto k$ (extended Kolmogorov spectrum), E(k) independent of k (broad Kolmogorov spectrum) and $E(k) \propto k^{-0.7}$ (raised Kolmogorov spectrum). The wavenumber k_0 at which the

turbulent cascade begins is not well defined. Theorists relate it to the mixing length; and arbitrariness of such definition introduces a free parameter.

The temporal part of the turbulent spectrum, represented by $\chi_k(\omega)$, the time evolution of the correlation between turbulent velocities (or other convective parameters) in two points separated by distance $2\pi/k$. Several analytical forms of $\chi_k(\omega)$ have been proposed by Stein (1967), Goldreich & Keeley (1977) and Musielak et al. (1994). Here, we consider, after Samadi et al. (2004), the Gaussian spectrum, the Lorentzian spectrum and the exponential spectrum, as well as power law behavior. A Gaussian function has been the usual choice for the acoustic p-mode excitation calculations, which simply states that two remote points in the turbulent medium are uncorrelated.

6.2 Spatial and Temporal Spectra

We investigate the spatial and temporal spectra of vertical and horizontal velocity components, turbulent and gas pressure and entropy. The functional behavior of these spectra seems to be resolution-dependent (Samadi et al. 2004), therefore we use the highest available resolution, $253\times253\times163$ grid points. We have a series of 1 hr 43 min of solar time. We calculate Fourier transforms of these parameters in horizontal space and time at a given depth. We construct the $k-\nu$ diagrams at several heights in the atmosphere: the visible surface ($\tau=1$), 100 km, 250 km, 500 km and 1 Mm beneath it. Thus we cover the depth range where the mode excitation is most efficient (Stein & Nordlund 2001). The $k-\nu$ diagram reveals the acoustic mode ridges. While mode peaks at low k_h numbers are most distinct in vertical velocity spectra, the mode

ridges are best shown in gas pressure (Fig. 17). We cut through these diagrams either at constant horizontal wavenumber or constant frequency to study the functional behavior of the parameters with frequency or horizontal wavenumber. In studying frequency dependence, we pay special attention to the frequency range where the mode driving occurs (between 2 and 5.5 mHz, where 5.5 mHz is the acoustic cutoff frequency). In studying the wavenumber dependence, scales comparable to granules are most important for consideration.

There are several general trends common for all parameters. For low frequencies, temporal spectra typically exhibit power law behavior at small k_h , while they form plateau at large k_h . At high frequencies, there is a power law decay for all k_h . Maximum power shifts to higher frequencies at higher k_h , and it shifts to lower frequencies with increasing depth. These features are rather common for all variables and heights. Spatial spectra show a wide inertial range at low frequencies, but this range vanishes with increasing frequency. Some parameters (vertical velocity) demonstrate this behavior close to the surface, while others (horizontal velocity, entropy) behave this way deeper down.

In Fig. 18, we present the temporal spectra of the vertical velocity at the depth of 0.5 Mm, for several wavenumbers. The spectra at small k_h are power laws (with acoustic modes showing in the peak driving frequency range), but with increasing k_h change to a plateau at low and intermediate frequencies. Horizontal velocities (Fig. 19) behave similarly, except they do not have distinct acoustic peaks. We choose several horizontal wavenumbers k_h and perform least squares fits to compare time spectra with several analytical functions: Gaussian, Lorentzian and Exponential

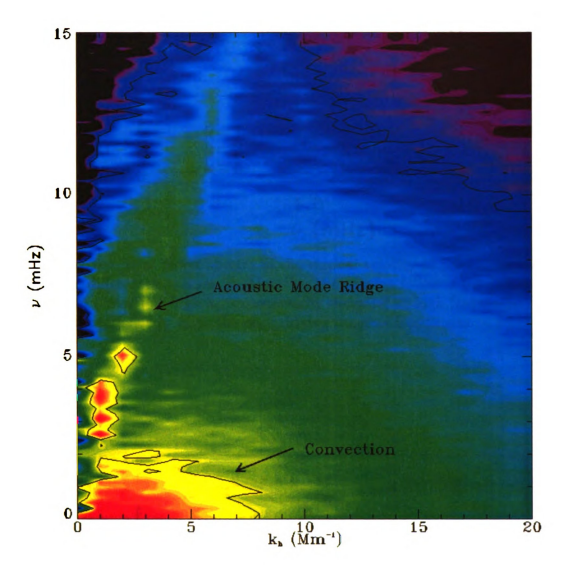


Figure 17. $k-\nu$ diagram for the gas pressure at the depth 1 Mm beneath the solar surface. Note the broad power peak in the convection region and narrow acoustic mode ridge.

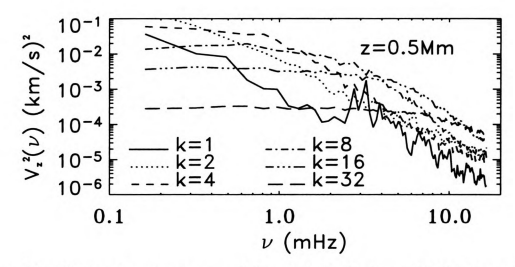


Figure 18. Temporal power spectra of the vertical velocity at 0.5 Mm beneath the surface, for different k_h values (in Mm⁻¹). The spectra follow a power law at low k_h and form plateau at high k_h , exponentially decaying at high frequencies. Modal structure appears at low k_h in the peak driving range of frequencies.

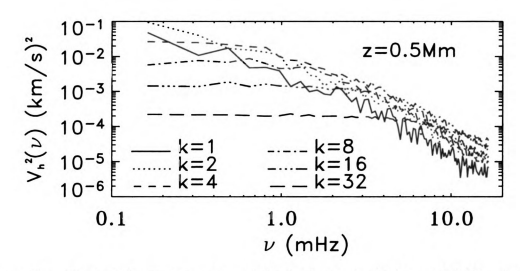


Figure 19. Temporal power spectra of the horizontal velocity at 0.5 Mm beneath the surface. Different values of k_h (in ${\rm Mm}^{-1}$) are considered. The spectra behave in similar way as the vertical velocity spectra, but modes are not visible.

(Samadi et al. 2004) (called respectively GF, LF and EF), and also perform the power law fits for the frequency regions where spectra seem to obey power law behavior.

At small horizontal wavenumbers (horizontal scales 1.5 Mm and larger), vertical and horizontal velocities show power law behavior at all depths and over a broad range of frequencies, from 1 to 10 mHz (Figs. 20, 21). At intermediate k_h (about 0.5 Mm horizontal distance), the velocity is a plateau at low frequency (and is close to all the forms GF, LF and EF) and becomes a power law at high frequency. The larger the horizontal wavenumber, k_h , the higher the frequency to which the plateau extends and the power law begins.

The turbulent pressure, gas pressure and entropy have similar temporal spectra to the velocities, except that they have a noticeable low frequency plateau even at small horizontal wavenumbers. All spectra have a steeper power law closer to the surface and generally a steeper power law at larger horizontal wavenumbers. The Gaussian spectra are always too small at high frequencies compared to the simulations. The Lorentzian spectrum (LF) usually gives a good fit to the simulations, especially at small k_h , but usually lies above the simulation results at high frequencies.

Functional dependence of spatial spectra presents another challenging problem. In the time-averaged spatial power spectra (Samadi et al. 2003b), the Kolmogorov energy cascade is not a good fit at any depth (Fig. 25). At individual frequencies, the behavior is different. In the low frequency range, up to 1 mHz, there is a Kolmogorov cascade with its characteristic -5/3 power law behavior in the broad range of spatial scales (Fig. 26). With increasing frequency the inertial range disappears (Fig. 27). Deeper down the power law slope is steeper than -5/3, and the spectra do not follow

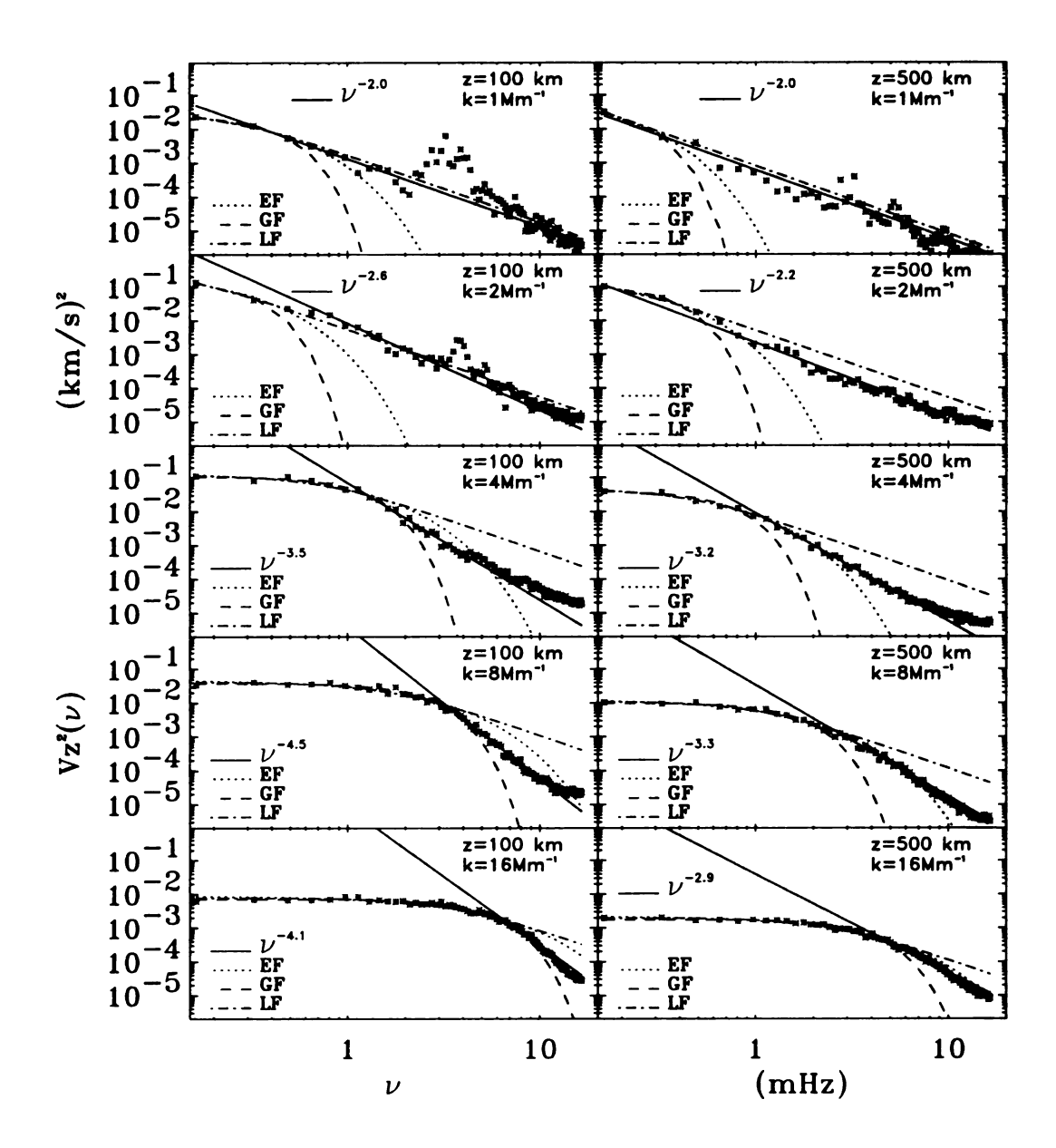


Figure 20. Temporal power spectra of the vertical velocity, at two depths z and for several wavenumbers k_h . Different power laws represent these spectra rather well, especially at low k_h . At higher k_h , broad plateau forms, and all functions give satisfactory fits.

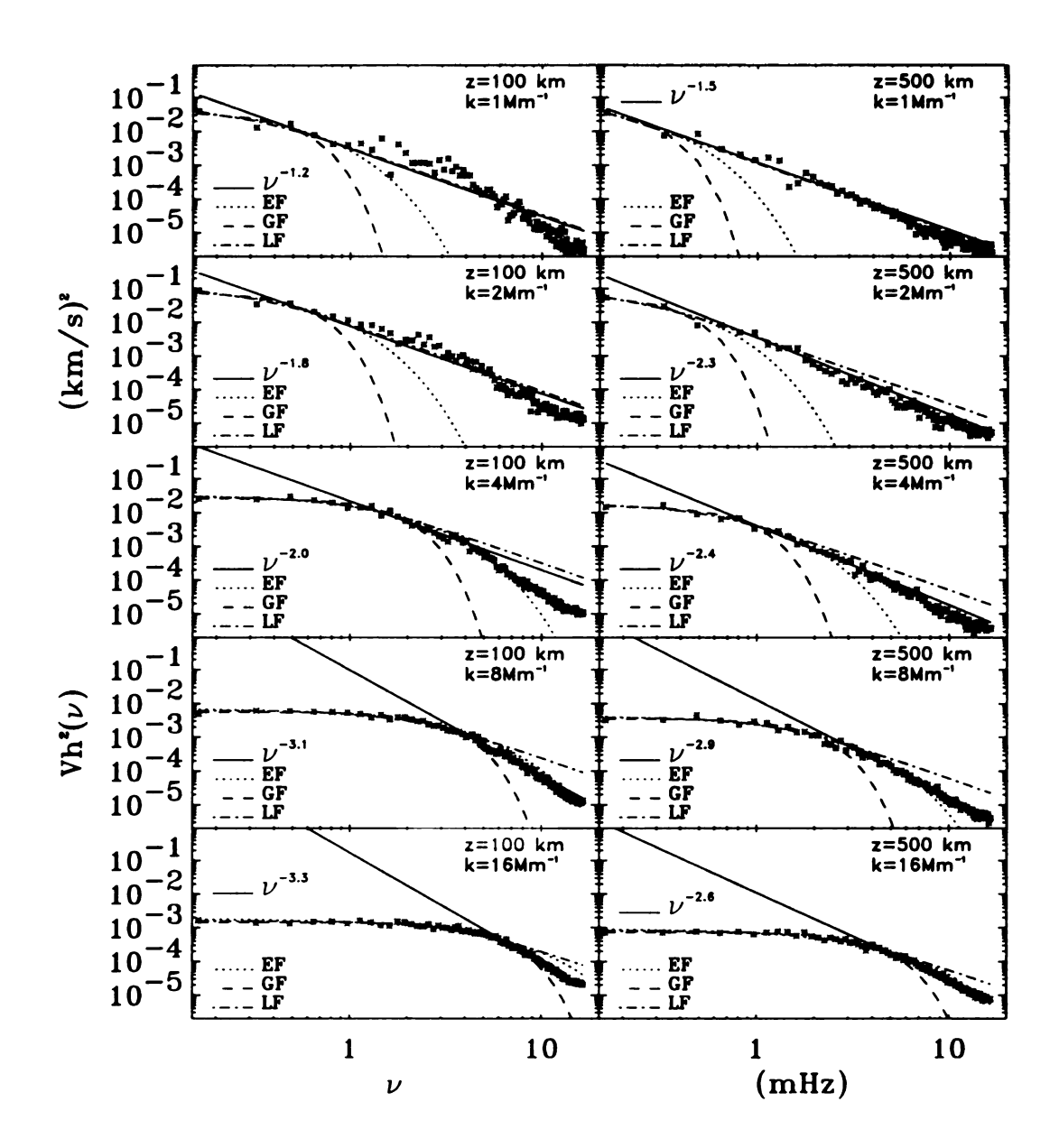


Figure 21. Temporal power spectra of the horizontal velocity, at same depths and wavenumbers. At low k_h , either power laws or LF could be a good representation of these spectra, while at higher k_h the spectra fall off as EF at high frequencies.

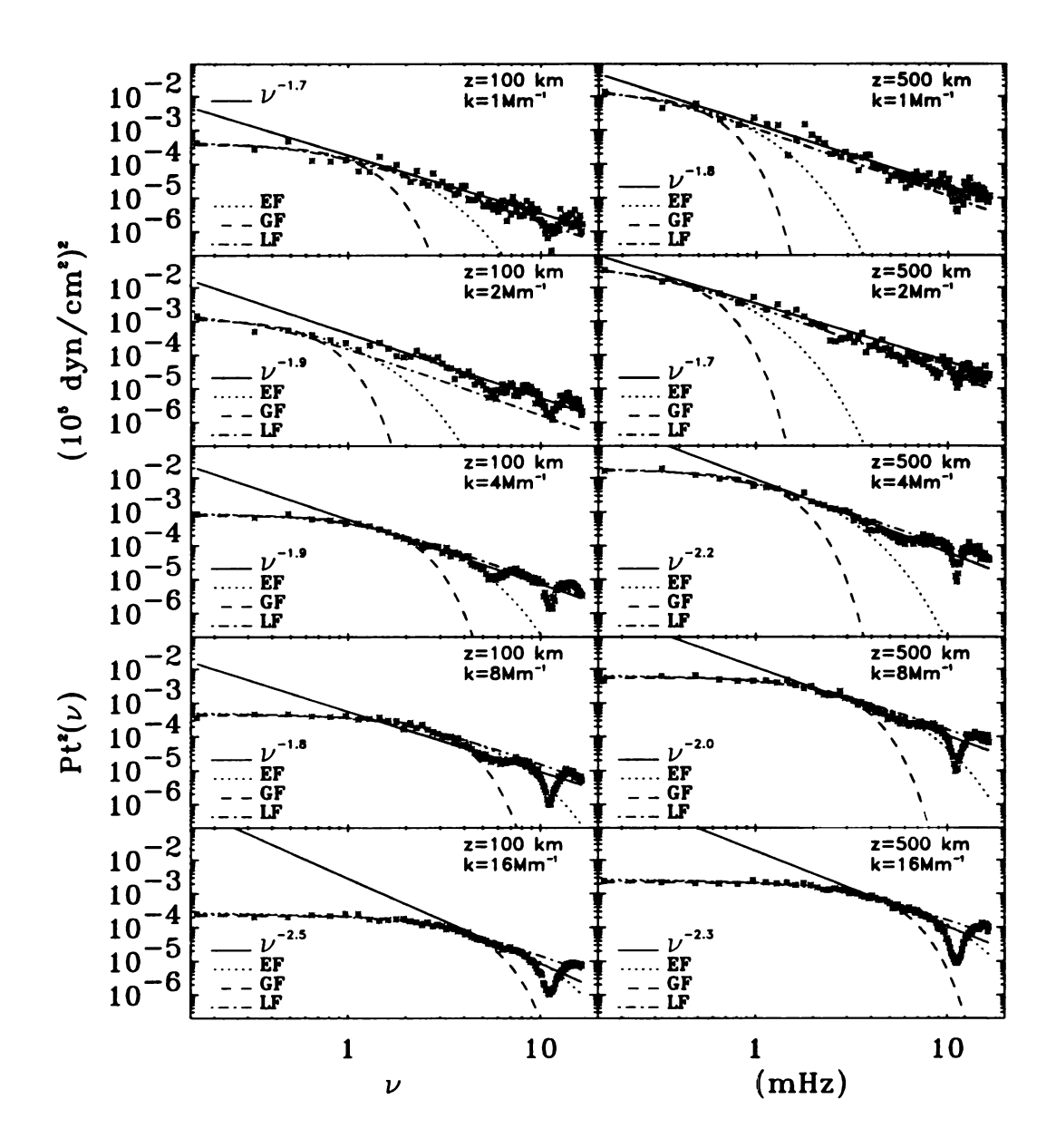


Figure 22. Temporal power spectra of the turbulent pressure, again at same depths and wavenumbers. Almost everywhere, LF seems to be a good match for these spectra. At low k_h , power laws also work rather well.

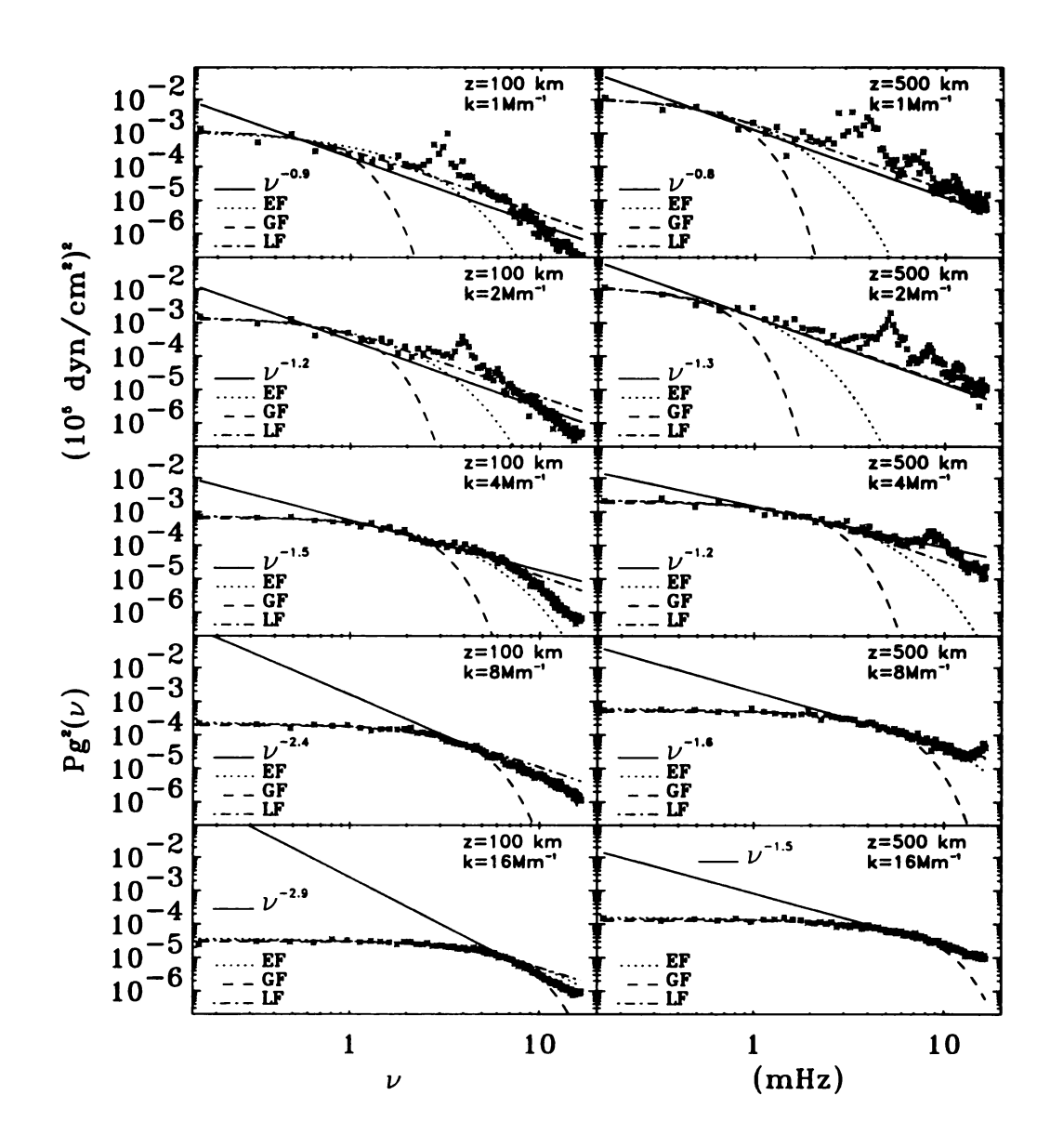


Figure 23. Temporal power spectra of the gas pressure, at same z and k_h values. As in vertical velocity, mode peaks are visible at low k_h . The spectra behave like LF or power laws at low k_h , and look similar to EF at high k_h .

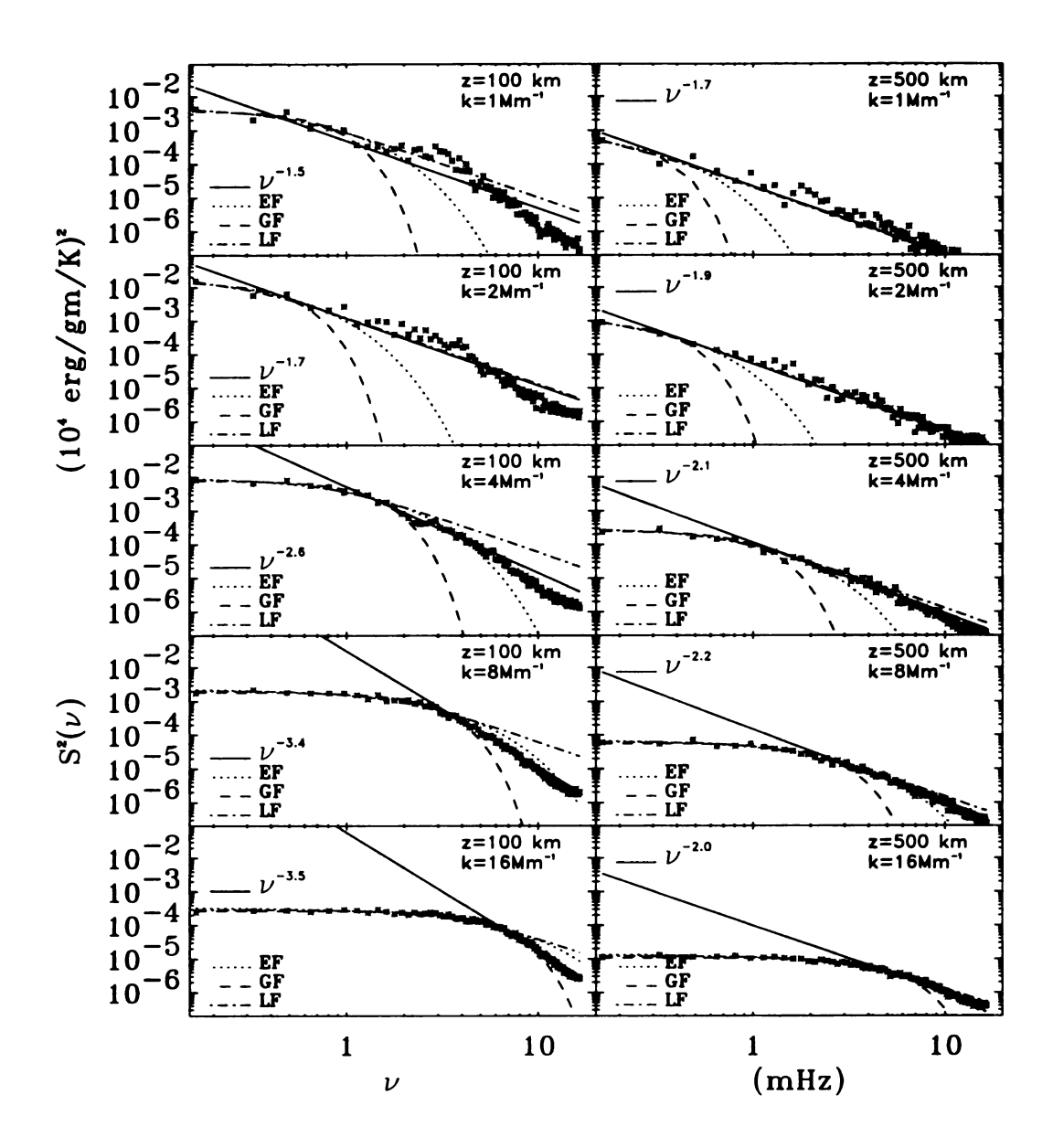


Figure 24. Temporal power spectra of the entropy, at same depths and wavenumbers. At large depths, they look like LF; power laws also fit well at low k_h . At low depths, they form a plateau and drift from LF to EF with increasing k_h .

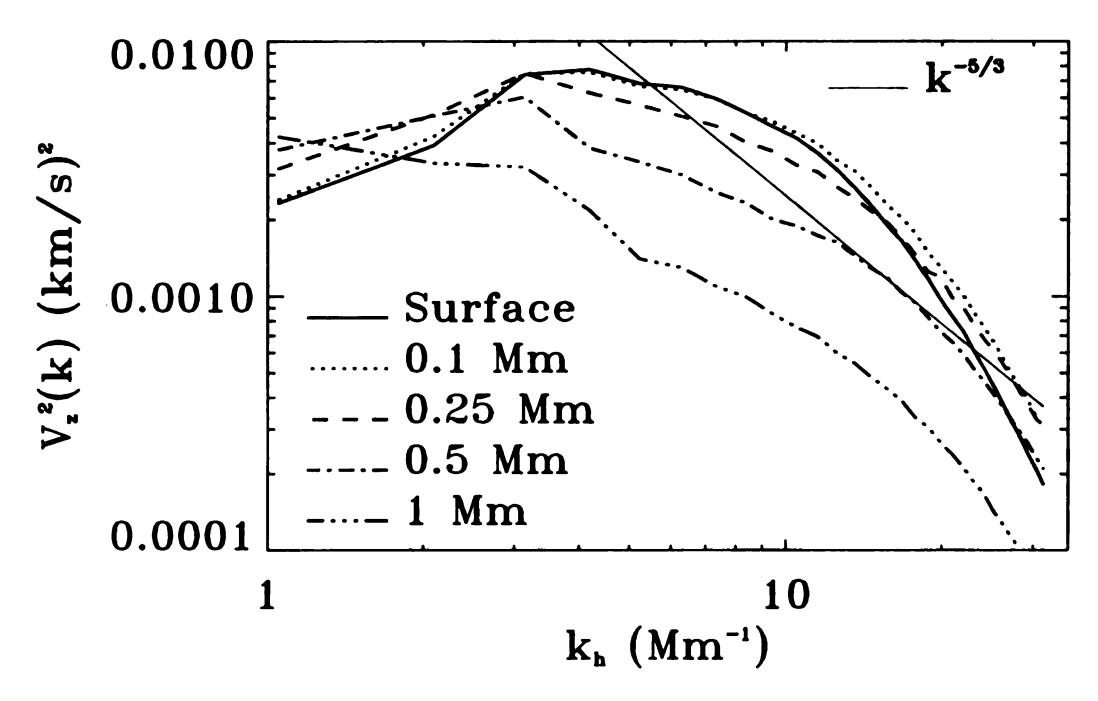


Figure 25. Frequency averaged spatial spectra of the vertical velocity at different depths. Thin solid line represents the power law of -5/3 characteristic for the turbulent cascade. The inertial range is extremely short, almost non-existent.

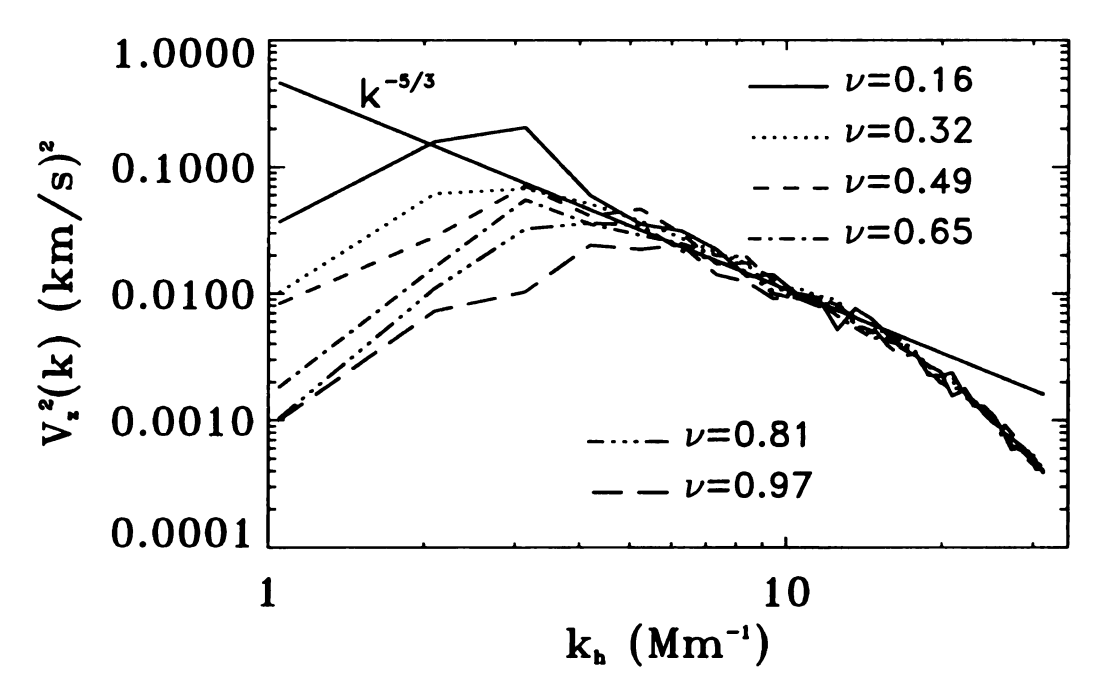


Figure 26. Vertical velocity spatial spectra for low frequencies, ν (in mHz), at 0.5 Mm below the surface. The inertial range extends from $k \simeq 3 \ \mathrm{Mm^{-1}}$ to $k \simeq 15 \ \mathrm{Mm^{-1}}$.

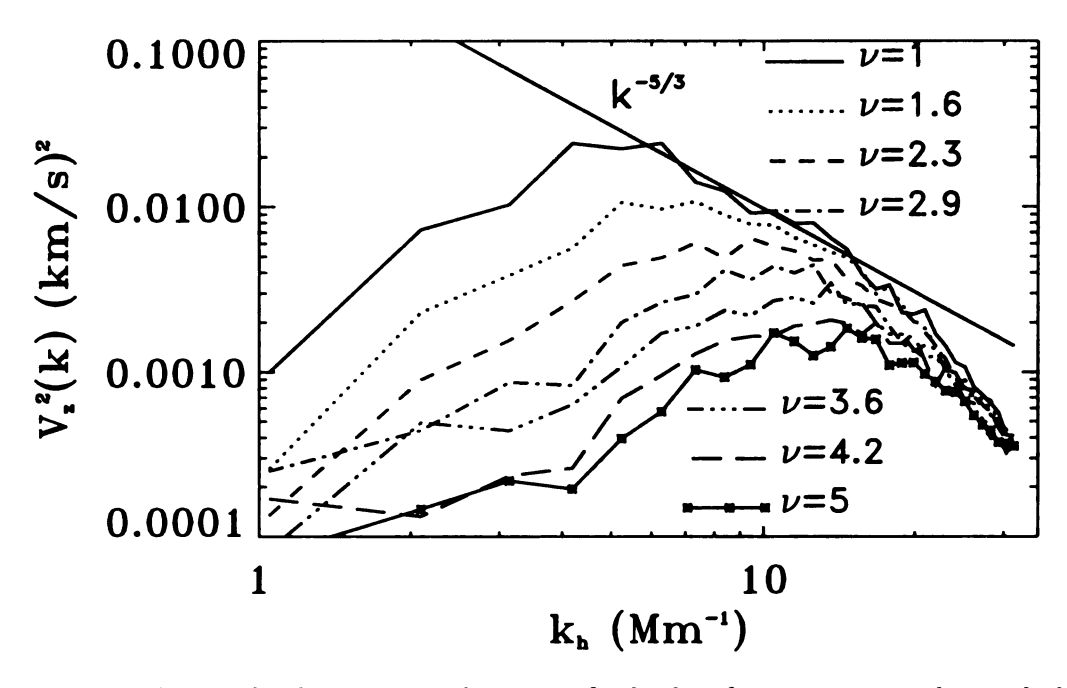


Figure 27. Vertical velocity spatial spectra for higher frequencies, in the peak driving range between 1 and 5 mHz. Inertial range disappears with increasing frequency. High k decaying tail corresponds to the numerical damping.

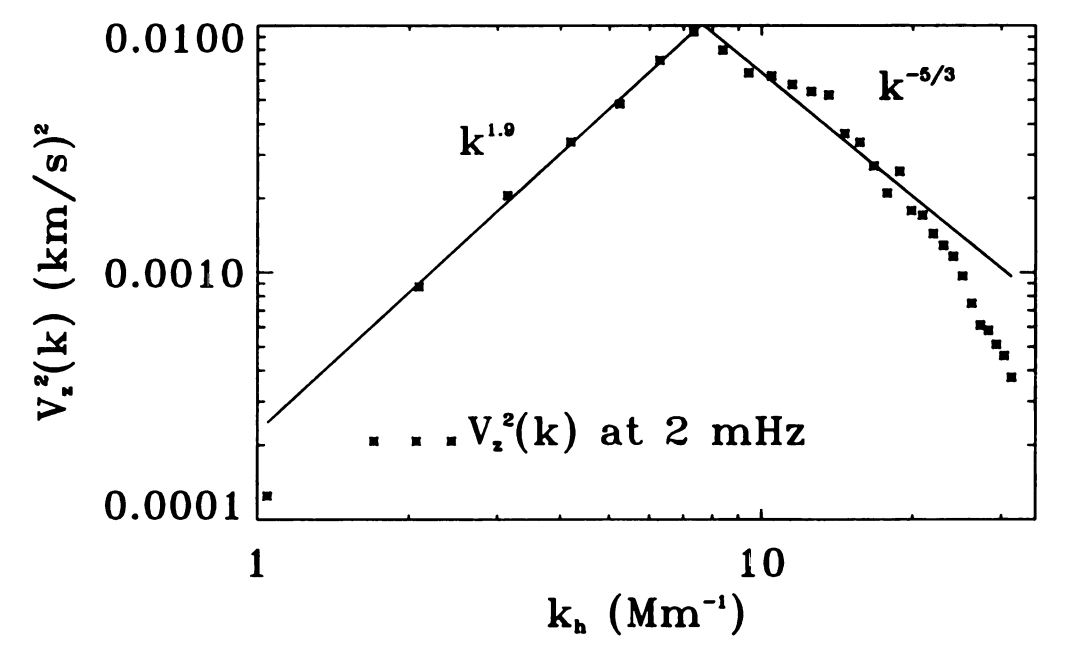


Figure 28. Spatial spectrum of the vertical velocity at 0.5 Mm, at $\nu=2$ mHz, away from the modes (stars). Two power laws, $k^{1.9}$ and $k^{-5/3}$, describe low and high k behavior (solid lines).

Kolmogorov's law even at low frequencies.

For the horizontal velocity components, the picture is quite opposite: the spatial spectra start out rather steep at the surface, but become Kolmogorov-like deeper towards 1 Mm. This must be because vertical velocity peaks close to the surface and then falls with depth rather quickly, while horizontal velocities are still significant around 1 Mm and deeper. Entropy looks similar to the horizontal velocity spectra, and in both cases, turbulent cascade at depth 1 Mm below the surface begins at large horizontal scales, 3 Mm or so for frequencies below 1 mHz. Gas pressure spectra show nice gradual profiles, with wide range of scales for Kolmogorov cascade, starting with rather low k_h . Turbulent pressure spectra have several interesting features: at the surface, they are rather flat, even at low frequencies, and the transition point between the plateau and decaying high k_h tail is located at very high wavenumbers, $k_h = 15$ ${\rm Mm^{-1}}$ and higher, at any frequency. This picture gradually changes with depth: at 1 Mm, maximum of the spectrum is located at horizontal scales 1-1.5 Mm at low frequencies, and horizontal sizes decrease with increasing frequency. The most interesting feature of the turbulent pressure spectra is the absence of deviation of the high wavenumber tail from the Kolmogorov power law. The deviation is attributed to the finite spatial resolution; at small scales, viscous dissipative effects begin to dominate. It is not clear why this feature does not seem to be present in the turbulent pressure spectrum.

For the low k_h range, neither observed solar spectra nor analytical estimates totally agree with the simulated results. For example, vertical velocity at 0.5 Mm, sampled at $\nu=2$ mHz (random frequency value preferably away from the modal

structure), shows power law with the exponent 1.9 (Fig. 28). Interestingly, intersection of the two slopes, at low and high k numbers, give k_0 approximately 7 Mm⁻¹, or 0.85 Mm horizontal scale. For the horizontal velocity components or the total velocity, the low k power law exponent is 0.65, but k_0 is still unexpectedly high, similar to the one found for the vertical velocity. For the velocities, the low k slope is more or less depth-independent. In the turbulent pressure spatial spectra at the peak mode frequency, the low k power law starts at the surface with the same coefficient as for the horizontal velocities, 0.65; it increases almost to 1 towards the 1 Mm depth. Gas pressure spectra are flat (independent of k) in the region of low kat all depths. The transition point between the plateau and $k^{-5/3}$ slope occurs at horizontal scales of 1-1.5 Mm, as expected. Entropy spectra also start flat at the surface, but they get steeper with depth, with power law exponents ranging from 0.5 at 0.1 Mm deep to 0.7-0.9 beneath it and back to 0.4 at 1 Mm beneath the surface. The transition between the plateau and decaying tail occurs around 0.75 Mm for entropy fluctuations. Most probably, at spatial scales smaller than 0.75 Mm viscous dissipation dominates.

6.3 Conclusions

Numerical simulations can be used to deduce analytic fits to the convective properties controlling the excitation of the p-mode oscillations.

Most importantly, temporal spectra have different functional forms at different spatial wavenumbers k_h . The Gaussian function does not represent any of the parameters well, except for very low frequencies (see also Samadi et al. 2003a). Indeed,

Gaussian behavior would imply that the convective characteristics are totally uncorrelated. This is expected at large time differences (low frequencies), but apparently this is not the case for high frequencies. Therefore, one should be cautious when using functional representations of these spectra in the calculations of stellar amplitudes or excitation rates.

Theorists usually consider time-averaged spatial spectra. These averaged spectra do not show an inertial cascade range for the resolvable scales in the simulation. The spatial spectra at different frequencies behave in different ways. At high frequencies, maxima of the spectra are shifted towards high wavenumbers, and the decaying slopes at high wavenumbers are probably due to viscous damping. Low wavenumber region of the spatial spectra does not correspond to the known power laws extracted from observations or obtained analytically; instead, it also exhibits different power laws depending on the parameter or sampling depth. Wavenumber k_0 , where the peak of power occurs, can be loosely defined as a crossing point between the power laws at low and high wavenumbers. From our results, k_0 seems to be higher than expected, which suggests that the mode excitation occurs not on the convective spatial scale (1-2 Mm) but at smaller scales, about 0.5-0.75 Mm. This is rather consistent with the idea of wave excitation in the narrow turbulent downflows, supported by observations (Goode et al. 1998).

In general, there are certain similarities between velocity and turbulent pressure temporal spectra, as well as between the gas pressure and entropy spectra. Both vertical velocity and turbulent pressure spectra manifest a power law behavior at low horizontal wavenumbers and exponential behavior at high wavenumbers. Both gas pressure and entropy spectra look like exponential function close to the surface, but become Lorentzian deeper down. On the other hand, there are subtle differences in their behavior. For example, the power law exponents are different for all parameters, at different depths and wavenumbers. These differences should be taken into account when one adopts a functional representation of these power spectra in analytical estimates of the mode excitation rates.

The rates of the energy input into the solar-like oscillations are very sensitive to the models of the turbulent stellar spectra (Samadi et al. 2001). For the Sun, it is possible to make assumptions about the spatial and temporal turbulent spectra from the observations of the solar granulation (although, cf. Nordlund et al. (1997)). Similar information cannot be obtained for other stars. It is therefore useful to calculate the turbulent spectra from the stellar simulations and deduce their behavior and functional dependence the way it has been done for the solar simulations (Samadi et al. 2004). Seismic observations of stellar oscillations will provide more information on the excitation and damping rates, contributing to better understanding of the stellar turbulent convection.

Chapter 7

EXCITATION OF STELLAR OSCILLATIONS

P-mode oscillations have been observed in several solar-like stars. They can be compared to stellar models to give invaluable information about stellar structure and evolution. We use 3D radiative- hydro-dynamical numerical simulations of stellar convective zones to calculate the excitation rates of stellar oscillations for several stars. Reynolds stress and entropy fluctuations make similar contributions to the mode excitation in main sequence stars. In more evolved stars, the dominant driving is caused by turbulent pressure fluctuations. Stellar excitation rates per unit area increase with increasing effective temperature and are nearly independent of surface gravity. The oscillation amplitudes depend on both excitation and damping rates. For the Sun, the total power in the simulation modes of given ℓ is comparable to that of the solar modes of that ℓ .

7.1 Introduction

According to the theory of stellar evolution, main sequence stars later than F have convective zones in their upper layers, where turbulent convection is responsible for energy transport. Convective motions and entropy fluctuations excite acoustic modes, so these stars are likely to exhibit solar-like p-modes. Such oscillations have been

already detected in several stars: Procyon (Martić et al. 1999), η Boo (Kjeldsen et al. 1995), α Cen A (Bouchy & Carrier 2001, 2002), α Cen B (Carrier & Bourban 2003), β Hyi (Bedding et al. 2001), ζ Her A (Morel et al. 2001), ξ Hya (Frandsen et al. 2002), α UMa (Buzasi 2002) and others (for a recent review, see Bedding & Kjeldsen (2003)).

One of the tasks of the NASA and ESA space missions is to detect such solar-like oscillations in other stars and measure their parameters, namely, frequencies, linewidths and amplitudes. These measurements will provide observational constraints on theories of stellar structure and oscillations. Improved knowledge of mode excitation and damping will help to better understand stellar surface convection. Detailed comparison between the modeling results and observations will clarify the theory of the interaction between stellar convection and oscillations.

There are several models of the stochastic excitation mechanism (e.g. Goldreich & Keeley 1977; Balmforth 1992; Goldreich et al. 1994; Stein & Nordlund 2001; Nordlund & Stein 2001). To evaluate the rate of p-mode excitation by turbulent convection, these models require a description of the properties of stellar turbulent convection. Unfortunately, both the mixing length theory (Böhm-Vitense 1958) and the more modern multiple size eddy model (Canuto & Mazzitelli 1991), are based on a number of approximations that all break down in the atmosphere and in the super-adiabatic layers just below, where a formulation of convection is most needed. Furthermore, both formulations introduce free parameters, and therefore lack predictive power in the description of the dynamic properties of turbulent convection.

3D simulations of stellar convection can provide a way to evaluate the excitation

expressions without making drastic approximations. We use this approach to probe the mechanisms that generate solar-like oscillations and their interplay with stellar turbulent convection. The excitation rates can be calculated directly from the simulations, without any simplifying assumptions or free parameters. To simulate the upper layers of solar and stellar convection, we use the numerical code of Stein & Nordlund (1998b, 2000). The code solves the system of compressible hydro-dynamics (HD) equations, including non-grey radiative transfer and ionization effects.

Limitations on computer resources restrict the simulated domain to a small volume in the stellar surface layers, typically of order 40 scale heights horizontally. For the Sun this is 6 Mm \times 6 Mm. Comparison between the calculated and observed excitation rates gives favorable results for the Sun (Stein & Nordlund 2001). We extend this analysis to other stars in order to investigate how stellar excitation rates depend on global stellar parameters.

Mode driving per unit area increases with increased effective temperature and is nearly independent of surface gravity. Reynolds stress and entropy fluctuations contribute comparably to the excitation of stellar modes in solar-like stars, but oscillations in hotter and giant stars are driven predominantly by turbulent pressure fluctuations.

We describe the formalism for the calculation of stellar mode excitation rates in Sect. 7.2. In Sect. 7.3 we give a short description of the convection simulations and their corresponding 1D stellar structure models. In Sect. 7.4, we present the results of our calculations, followed by conclusions in Sect. 7.5.

7.2 Mode Excitation Rates

The rate of energy input to the modes can be derived from the PdV work using the kinetic energy equation (Nordlund & Stein 2001). This is a stochastic process, so the pressure fluctuations occur with random phases with respect to the oscillation modes. Therefore the excitation expression must be averaged over all possible relative phases. The resulting rate is

$$\frac{\Delta \langle E_{\omega} \rangle}{\Delta t} = \frac{\omega^2 \left| \int_r dr \, \delta P_{\omega}^* \, \frac{\partial \xi_{\omega}}{\partial z} \right|^2}{8 \, \Delta \nu \, E_{\omega}} \,, \tag{2}$$

where δP_{ω}^{*} is a Fourier component of the nonadiabatic, incoherent pressure fluctuations, $\Delta \nu$ is the frequency resolution, ξ_{ω} is the mode displacement eigenfunction,

$$E_{\omega} = \frac{1}{2}\omega^2 \int dr \,\rho \,\xi_{\omega}^2 \left(\frac{r}{R}\right)^2 \tag{3}$$

is the mode energy. We can evaluate Eq. (2) numerically from the simulation, without making any of the assumptions necessary for analytical estimates. The mode excitation rate can be evaluated either in Fourier space or in real space (cf Appendix A in Stein & Nordlund (2001)). Here, we use the Fourier space formalism. First, we calculate the non - adiabatic pressure fluctuations. We obtain the gas pressure, turbulent pressure, density and Γ_1 from the simulations as function of (3D) space and time. The non-adiabatic total $P_{\text{tot}} = P_{\text{gas}} + P_{\text{turb}}$ pressure is calculated from

$$P^{\text{nad}} = (\ln P_{\text{tot}} - \Gamma_1 \ln \rho) P_{\text{tot}}. \tag{4}$$

At that point, we perform horizontal averaging, transform averaged quantities to the Lagrangian frame and then calculate $\delta P^{\rm nad}$, the fluctuations of $P^{\rm nad}$ about its time average. The calculations of the mode displacement eigenfunction $\xi_{\omega}(z)$ are described in Sect. 7.3. In Fourier space, the integral in Eq. (2) is evaluated by taking the time Fourier transform of $\delta P^{\rm nad}$ at each depth z. At the same depth, it is multiplied by the vertical derivative of the mode displacement, interpolated to the simulation frequency scale (defined by simulation time interval and duration) and normalized by the square root of the mode energy. Having done it for each depth, we integrate the result over the depth of the simulation domain, square the absolute value of the integral, and divide by $8 \, \delta \nu$. This gives, finally, the energy input rate per unit area to the modes as function of frequency.

To obtain the total excitation rate for the entire star we multiply by the area of the computational domain which is taken large enough to include several granules and at least one mesogranule. We find that the pressure fluctuations are uncorrelated on larger scales, so the average of δP^2 decreases as the inverse of the area. Multiplication by the area of the simulations gives the driving for the entire star independently of the domain size as long as it is sufficiently large to include many granules. The absence of supergranule and severely constrained mesogranular flow decreases our results for very low frequency modes but does not affect the modes near the frequencies of maximum driving.

Application of this formalism to low- ℓ , solar modes gives results very similar to the actual excitation rate $dE_{\omega}/dt = \Gamma E_{\omega}$ found from energies, E_{ω} , and widths, Γ , of the observed modes (Stein & Nordlund 2001).

Theories predict two main sources of mode driving: turbulent Reynolds-stress and entropy fluctuations. To find the relative importance of different excitation sources, we apply Eq. (2) to individual components of the pressure: the non-adiabatic gas pressure fluctuations which corresponds to entropy fluctuations, and turbulent pressure which reflects the Reynolds-stress contribution,

$$\delta P = \delta P_{\text{turb}} + \delta P_{\text{gas}}^{\text{nad}}, \tag{5}$$

where $\delta P_{\rm turb} = \delta \langle \rho \, \delta V_z^2 \rangle$, and $\delta P_{\rm gas}^{\rm nad}$ is obtained by substituting $P_{\rm gas}$ instead of $P_{\rm tot}$ in Eq. (4). Both components make comparable contributions to the mode excitation on the Sun, and it is important to determine how these contributions depend on stellar parameters.

7.3 Stellar Simulations

We use the 3D convection-code to simulate the surface layers of a number of stars with convective envelopes. From these simulations, we calculate mode parameters and excitation rates directly.

Convection simulations of 6 different solar-type stars were carried out by Trampedach et al. (1998). These hydrodynamical models are, like conventional stellar atmosphere models, characterized by the effective temperature, $T_{\rm eff}$, acceleration of gravity, g, and chemical composition, as listed in Tab. 1. We include the solar model with the same input physics and spatial resolution for comparison purposes. The surface gravity is an input parameter, whereas the effective temperature is adjusted by changing the

entropy of the inflowing gas at the bottom boundary. The temperatures of the simulations therefore only roughly correspond to the observed ones. All of these models are calculated with a spatial resolution of $50\times50\times82$ grid points. They have solar-like chemical composition, with X=70.3% and Z=1.45%. The first four models mimic actual stars, whereas the last two, Star A and Star B, represent hypothetical stars with the given parameters. They all span 11–14 pressure scale-heights in depth, extend out to $\log \tau \simeq -5.5$ in the atmosphere and reach deeper than $\log \tau \simeq 6$ (both for the Rosseland and the 5000 Å optical depth-scale). Here and after, log implies \log_{10} .

The simulation domains are shallow, containing only few modes. In order to obtain all the mode eigenfunctions, we extend the simulations inward, by means of conventional, 1D stellar envelopes. We use the stellar envelope-code presented in Christensen-Dalsgaard & Frandsen (1983), which employs the mixing-length formalism of convection by Böhm-Vitense (1958).

Trampedach et al. (2003a) fit average stratifications of the seven convection simulations to 1D stellar envelopes, by matching temperature and density at a common pressure point near the bottom of the simulations. The fitting parameters are the mixing-length parameter, α , and a form-factor, β , in the expression for turbulent pressure: $P_{\text{turb}}^{1D} = \beta \varrho u_{\text{MLT}}^2/2$, where u_{MLT} is the convective velocities predicted by the mixing-length formulation. By employing the exact same atomic physics in the simulations as well as in the 1D envelopes; the MHD equation of state (EOS) (Däppen et al. 1988) and line-opacities in the form of opacity distribution functions (ODF) by Kurucz (1992a,b), and by using T- τ relations derived from the simulations

Table 1. Simulated stars, resolution $50 \times 50 \times 82$

star	$T_{ m eff}$ [K]	$\log g$	M/M_{\odot}	R/R_{\odot}	L/L_{\odot}
α Cen A	5768	4.30	1.08	1.228	1.50
$\alpha\operatorname{Cen} \mathrm{B}$	5363	4.56	0.90	0.827	0.51
$\eta\mathrm{Boo}$	6023	3.75	1.63	2.805	9.31
Procyon	6470	4.04	1.75	2.102	6.96
$\operatorname{Star} A$	4851	4.10	0.60	1.150	0.66
Star B	6167	4.04	1.24	1.769	4.07
Sun	5802	4.44	1.00	1.000	1.02

(Trampedach et al. 2003b), a smooth and consistent matching of the two is ensured.

Using the average stratification of the simulations augmented by 1D envelope models in the interior, we calculate eigenfunctions of the p-modes, using the adiabatic pulsation code by Christensen-Dalsgaard & Berthomieu (1991).

We also include three convection simulations of an F and a K dwarf, and a K subgiant, as listed in Tab. 2 (cf. Ludwig & Nordlund 2000). These simulations were run at a higher resolution; $125 \times 125 \times 82$, better suited for studying the spatial properties of convection. The effects of numerical resolution on the convection simulations, are investigated by Stein & Nordlund (1998b) and Asplund et al. (2000). The computer code is the same as used for the seven simulations described above, but there are also a number of differences: the matching to a 1D envelope model is carried out, by matching the entropy near the bottom of the convection zone to the entropy of the completely adiabatic parts of the up-flow in the convection simulations (Ludwig et al. 1999). This process uniquely determines the principal parameter of the convection formulation used, e.g., α for the mixing-length formulation. However, since Ludwig et al. (1999) do not allow for a turbulent pressure in the 1D envelopes, the averaged

simulation and the 1D models do not match up, and therefore the pure 1D models are used for the calculation of eigenmodes.

Table 2. Simulated stars, resolution 125×125×82

star	$T_{ m eff}$ [K]	$\log g N$	M/M_{\odot}	$_{\odot}R/R_{\odot}$	L/L_{\odot}
ΚV	4700	4.44	0.8	0.892	0.35
FV	6640	4.44	1.4	1.180	2.43
KIV	4610	2.94	1.0	5.592	12.7

We analyze stars in a wide range of evolutionary states, from the main-sequence and up to the beginning of the ascend along the Hayashi track, and for masses ranging from about $0.6\,M_{\odot}$ to $1.7\,M_{\odot}$.

7.4 Results

We now have all the ingredients for calculating p-mode excitation rates, as well as the separate contributions from entropy fluctuations and Reynolds stresses. We apply the formalism described in Sect. 7.2 to the convection simulations listed in Sect. 7.3 and calculate the oscillation excitation rates. Figure 29 shows the spectra of the calculated mode excitation rates per unit area for the 7 solar-like stars whose characteristics are listed in Table 1 and for 3 non-solar like stars whose characteristics are listed in Table 2 and whose simulations were carried out at higher resolution.

Figure 30 shows the frequency integrated excitation rates per unit area and Figure 31 shows the total frequency integrated excitation rate as a function of log surface gravity and log effective temperature. Clearly, mode driving per unit area increases with increasing effective temperature and is rather insensitive to surface

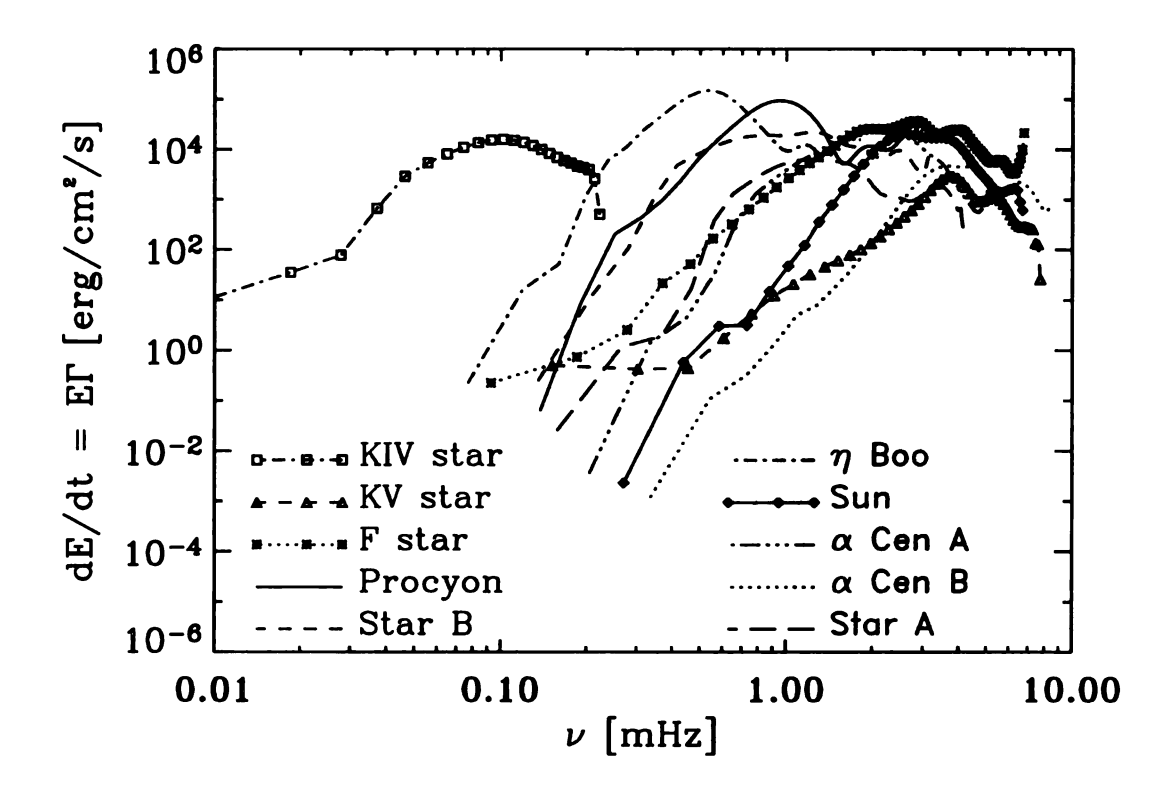


Figure 29. Spectra of excitation rates per unit area, due to the total pressure fluctuations, for the simulated stars. Peak excitation increases with increasing effective temperature and lower surface gravity shifts the spectrum to lower frequencies.

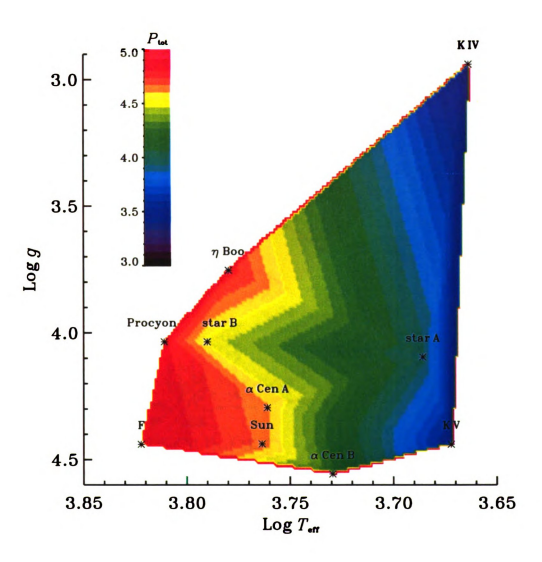


Figure 30. Energy input rate per unit area integrated over the frequency (base 10 logarithms in $\operatorname{erg/cm^2/s}$) as a function of T_{eff} and $\log g$ for two sets of stellar simulations. Excitation is higher in hotter stars with larger convective fluxes and higher convective velocities.

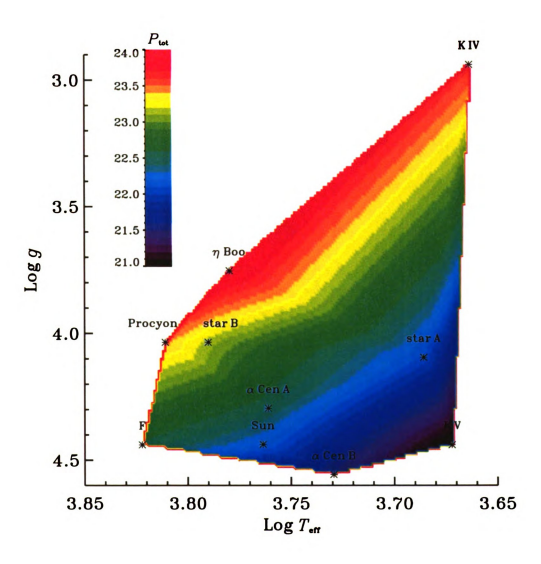


Figure 31. Energy input rate integrated over the frequency (base 10 logarithms in erg/s), presented as function of $T_{\rm eff}$ and log g for two sets of stellar simulations. Total excitation is higher in hotter stars and in stars with lower surface gravity, where convection is more vigorous and surface area is larger.

gravity. Higher convective fluxes require larger temperature fluctuations and velocities to transport the energy. This leads to larger gas and turbulent pressure variations and more driving. The excitation rate per unit area is reasonably well fit by a power law $dE/dt \propto T_{\rm eff}^9$ (Fig. 32).

Peak driving occurs at lower frequency for lower gravity (Fig. 29) because the natural buoyancy frequency, $N = \sqrt{g \left(1/\Gamma_1 d \ln P/dr - d \ln \rho/dr \right)}$, as well as the acoustic cutoff frequency, $\omega_{\rm ac} = c_s/2H\sqrt{(1-2dH/dr)}$, decrease (here, g is the gravitational acceleration, Γ_1 is $(d \ln P/d \ln \rho)_s$, P is the pressure, ρ is the density, c_s is the sound speed and $H = P/\rho g$ is the pressure scale height).

Simulations of solar convection with different spatial resolutions, from 25 to 200 km, show that excitation rates are insensitive to resolution at low frequencies but differ at high frequencies (Fig. 33). This is expected because at lower resolutions small features contributing to high frequency power are unresolved. The two different sources of excitation, turbulent and gas pressure, behave in a similar way. Comparison of line profiles reveal that at the highest resolution used the simulated average profiles match the observed profiles within 1% (Asplund et al. 2000), indicating that the model velocities contributing to spectral line profiles are converged at this resolution. However, no clear trend of driving with simulation resolution is apparent here, partly because the statistics is not quite sufficient to show it. One should mention that the average $T_{\rm eff}$ is slightly different for these different solar calculations: it is 5643 K for the lowest resolution, it does not differ much between the $63 \times 63 \times 63$ and $125 \times 125 \times 82$, being respectively 5673 K and 5676 K, but for the highest resolution it reaches 5735 K. Also, the simulation duration for different resolutions vary from 1

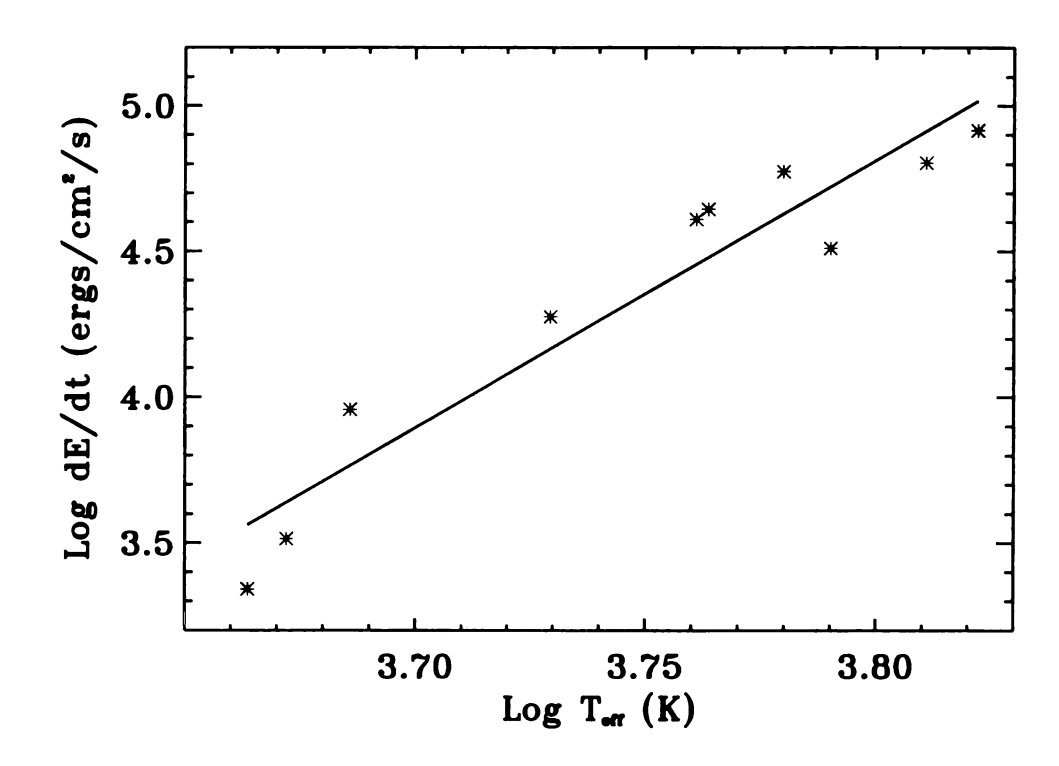


Figure 32. Energy input rate integrated over frequency as a function of effective temperature (stars). The excitation is fit by a power law, $dE/dt \propto T_{\rm eff}^9$ (solid line).

hr for the lowest resolution to 40 hr for $63\times63\times63$ and back to shorter time series of approximately 2 hours for the two highest resolution runs.

For the Sun excitation due to turbulent pressure (Reynolds stresses) and entropy (non-adiabatic gas pressure) fluctuations is comparable, with the turbulent pressure contribution slightly larger in the maximum mode driving range (Fig. 34). But this varies with stellar type. We use the consistent set of higher spatial resolution of the FV, KV and KIV stars to investigate how the relative contributions from these two sources change with stellar properties. In the FV star, the turbulent pressure contribution dominates the excitation everywhere, especially in the peak driving range (Fig. 35). In the KV star, the two components are very close to each other (Fig. 36). Finally, in the KIV star, Reynolds stresses dominate everywhere, especially near maximum driving (Fig. 37). Note, the total pressure contribution is not merely a sum of the two pressure components; sometimes these components are out of phase, and the destructive interference between them leads to a reduced total excitation rate.

The frequency integrated excitation rates due to the turbulent and gas pressure are presented in Figs. 38 and 39. One can see that the turbulent pressure contributions dominate in the majority of the simulated stars, with a few exceptions. The turbulent and gas pressure contributions are comparable in the Sun and solar-like stars, but as stars become hotter or more evolved (subgiants), convective efficiency increases and Reynolds stresses play more important role as excitation sources comparing to entropy fluctuations.

Excitation is typically thought to depend on a power of the convective velocity

(Stein 1967; Goldreich & Keeley 1977; Goldreich et al. 1994), and we find this to be the case for main sequence stars (Fig. 40). However, the power exponent is unexpectedly low, $dE/dt \propto v_{\rm rms}^{1.5}$, which is even smaller than expected for monopole radiation ($\propto v^4$). We do not know the explanation. The KIV subgiant excitation rate lies substantially below the main sequence stars with comparable velocity. Part of the explanation (about one order of magnitude) lies in the one order of magnitude shift to lower frequencies of the emission peak. Other factors are also likely to play a role.

Christensen-Dalsgaard & Frandsen (1983) and Houdek et al. (1994) argued that more evolved stars, like subgiants, will oscillate with larger amplitudes than main sequence stars, consistent with our excitation results. In order to evaluate amplitudes, though, we also need to calculate the damping rates, opposing the excitation. This will be the subject of a future paper.

7.5 Conclusions

Mode excitation rates have been calculated for different stars using simulations of their convection zones. It has been found that excitation per unit area increases with increasing effective temperature and is nearly independent of surface gravity. When viewed as a function of velocity the main sequence star excitation rates vary as approximately $v_{\rm rms}^{1.5}$, but the subgiant star falls far below this line. Reynolds stress and entropy fluctuations contribute more or less equally to mode driving in solar-like stars, while in subgiants and hotter main sequence stars, where convective velocities are larger and turbulent to total pressure ratio is higher, Reynolds stresses contribute

more to the excitation rates than the non-adiabatic gas pressure (entropy) fluctuations.

One of the goals of various international space missions is to observe stellar oscillation amplitudes. Mode amplitudes arise from the balance between mode excitation and damping. In general, stellar damping rates can be associated with the effects of the momentum balance and thermal energy balance (Houdek et al. 1999). These two contributions, in turn, can be divided into several mechanisms considered separately by different authors (cf Figure 2 in Houdek (2002)). It can be a non-trivial task to calculate such effects as transmission of waves into the atmosphere (Balmforth & Gough 1990). On the other hand, radiative damping (Christensen-Dalsgaard & Frandsen 1983), and modulation of the turbulent momentum flux (turbulent pressure) and heat flux by the pulsation (Gough 1977) should be possible to track down within the boundaries of the simulated domain. These calculations are left for future work. Once the contributions of different damping mechanisms to the total mode damping rate have been determined, excitation and damping results can be combined to estimate stellar oscillation amplitudes. One can compare them to the amplitudes extracted directly from the simulations by evaluating velocities at the observational level, and ultimately, compare these results to the actual observations. Also, predictions of amplitudes of stellar oscillations are helpful for choosing possible targets of space missions.

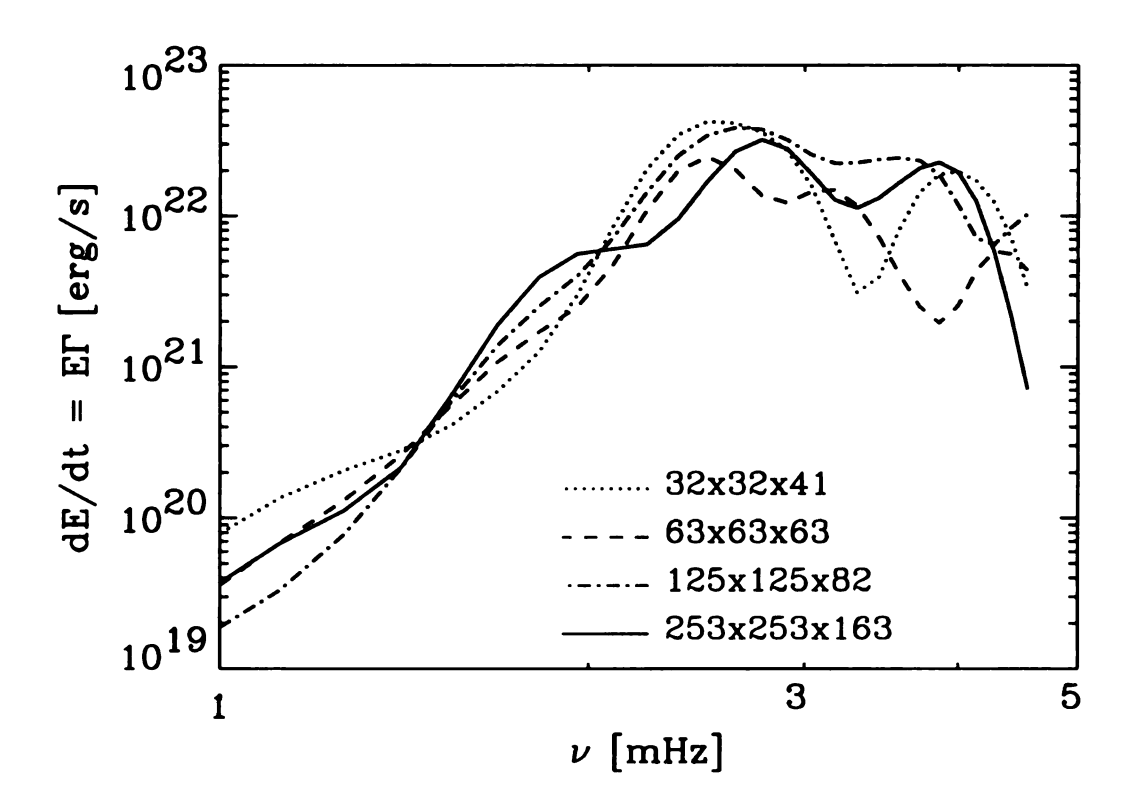


Figure 33. Energy input rates in the Sun for different spatial resolution.

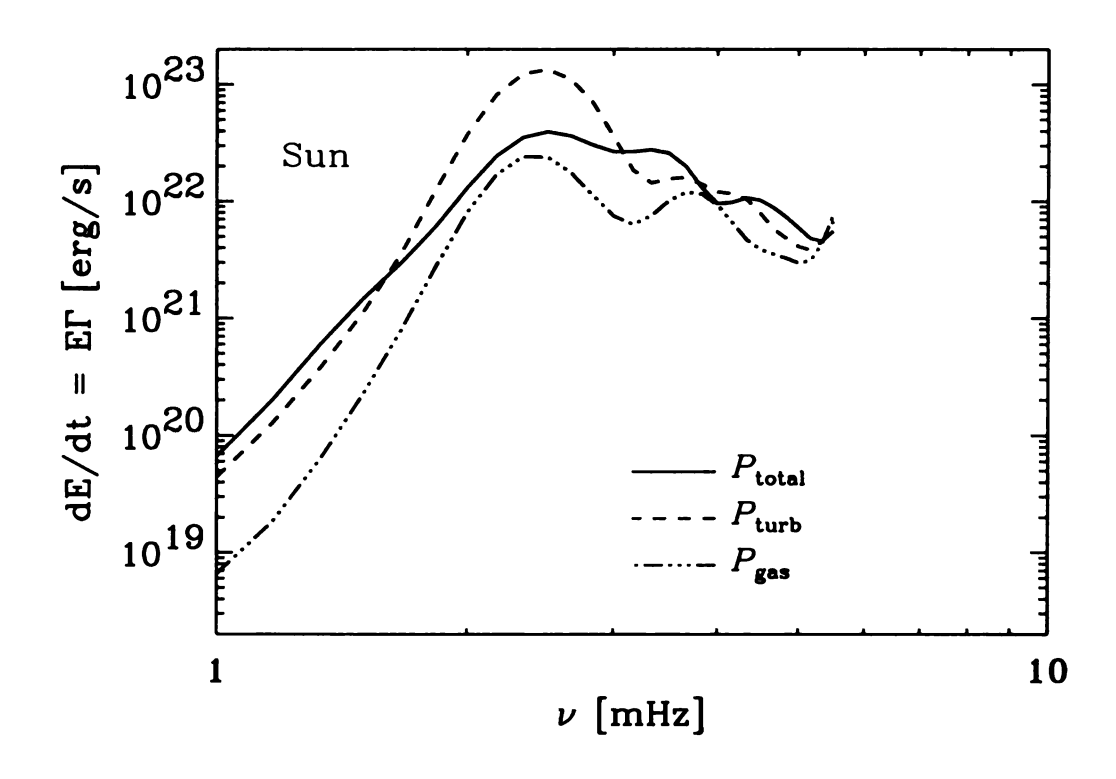


Figure 34. Mode driving in the Sun. Contributions from gas- and turbulent-pressure are shown separately, along with the total excitation rate.

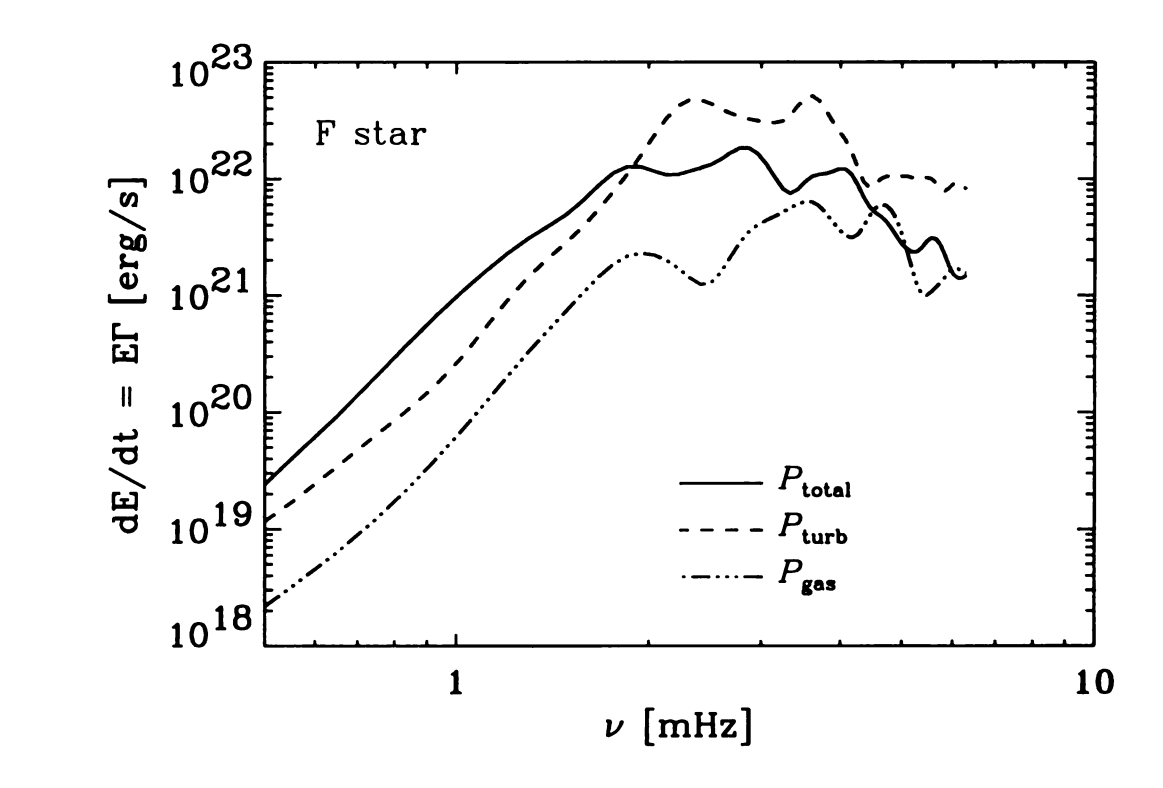


Figure 35. Mode driving in the FV star. As in Fig. 34, the individual contributions, as well as the total excitation rates, are presented.

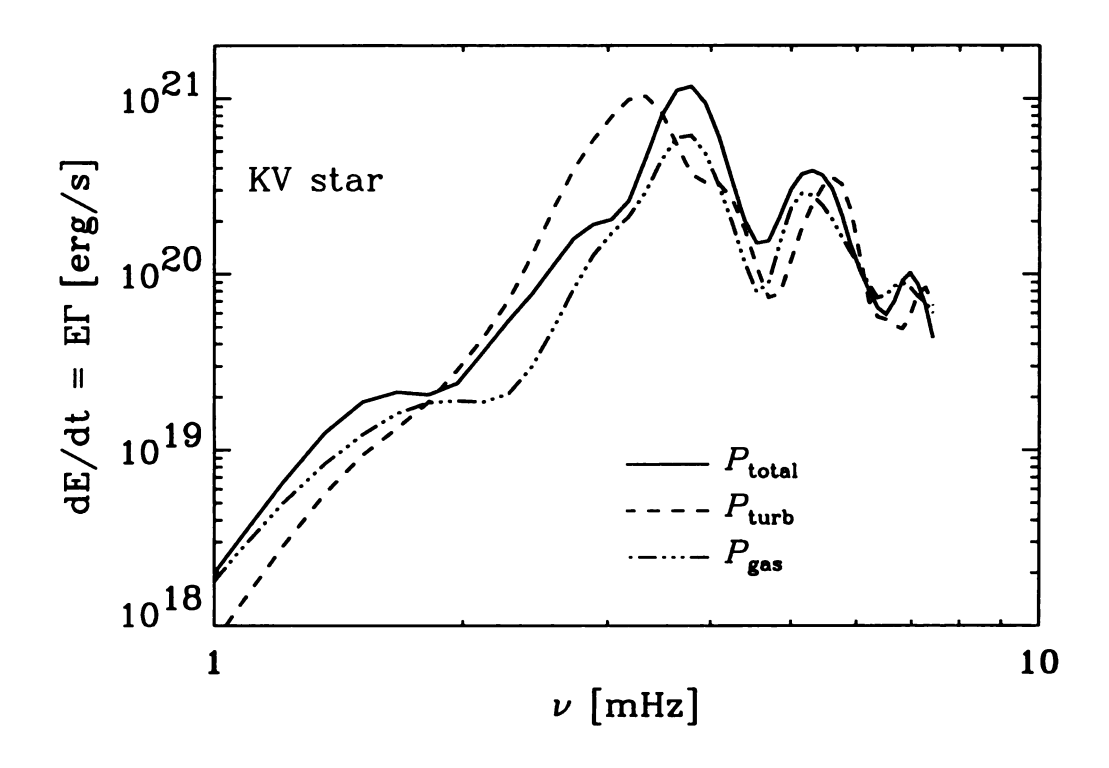


Figure 36. Mode driving in the $K\,V$ star. As in Fig. 34, the individual contributions, as well as the total excitation rates, are presented.

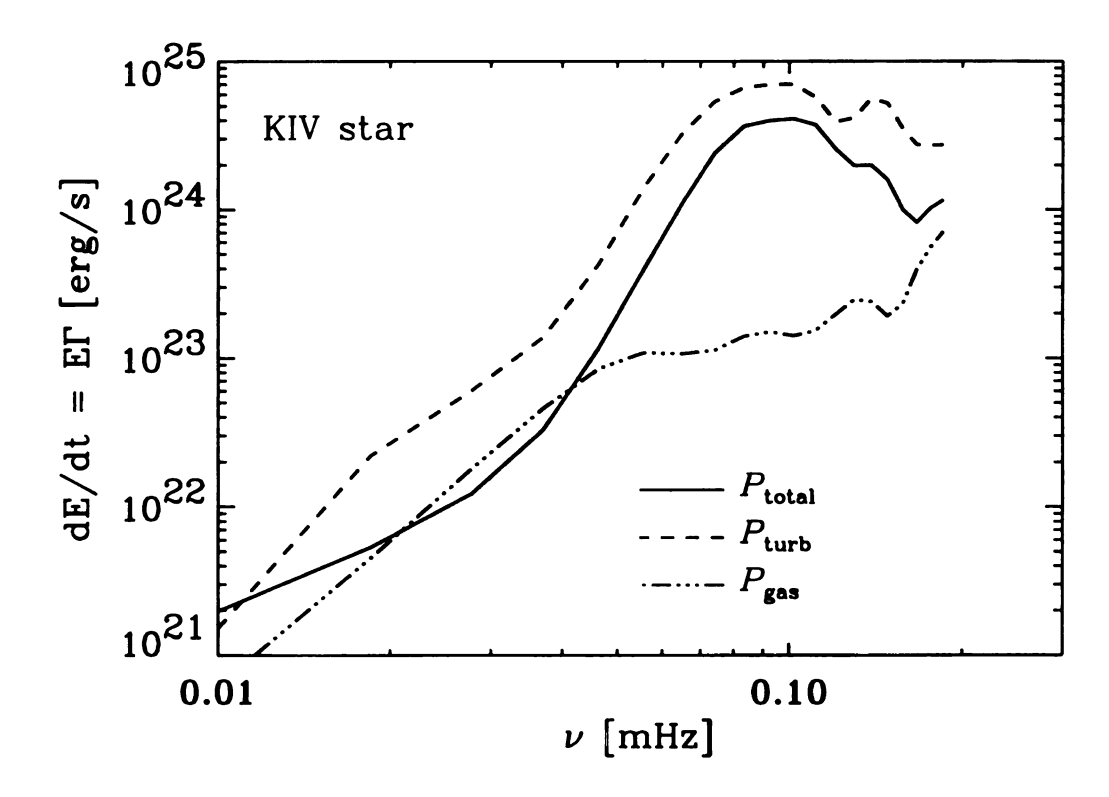


Figure 37. Mode driving in the K IV star. As in Fig. 35, the individual contributions, as well as the total excitation rates, are presented. Note the different frequency range.

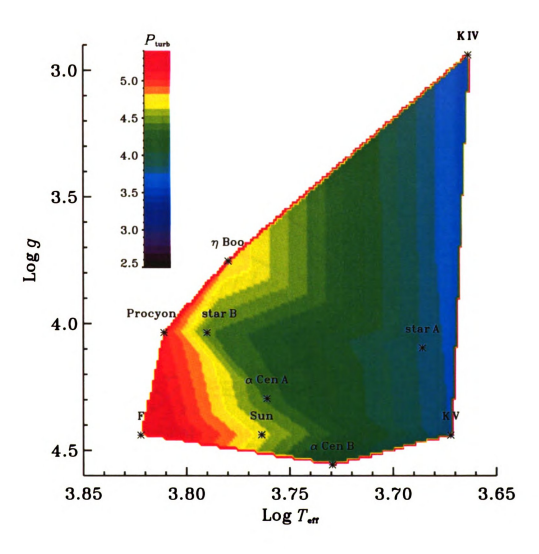


Figure 38. Energy input rate due to the turbulent pressure, per unit area, integrated over the frequency (base 10 logarithms in $\operatorname{erg}/\operatorname{cm}^2/s$) as a function of $T_{\rm eff}$ and $\log g$. Excitation is higher in hotter stars with larger convective fluxes and higher convective velocities.

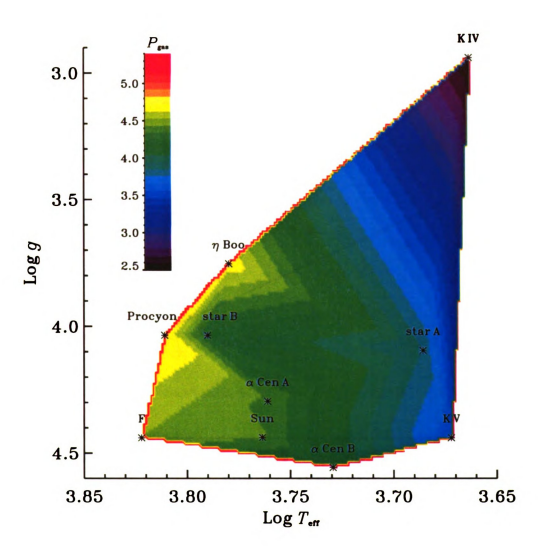


Figure 39. Energy input rate due to the gas pressure, per unit area, integrated over the frequency (base 10 logarithms in $\operatorname{erg}/\operatorname{cm}^2/\operatorname{s}$) as a function of $T_{\rm eff}$ and $\log g$ for two sets of stellar simulations. Excitation is higher in hotter stars with larger convective fluxes and higher convective velocities.

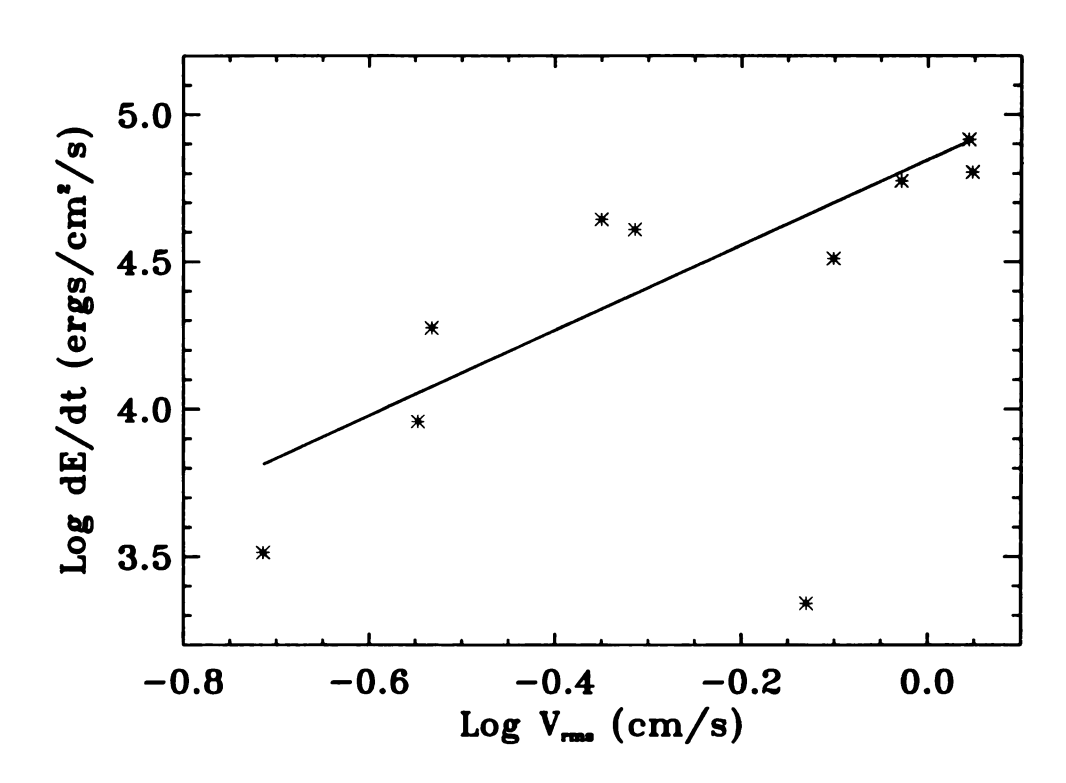


Figure 40. The frequency-integrated excitation rates as a function of the maximum rms vertical velocity. The main sequence stars' excitation vary roughly as $v^{1.5}$.

Chapter 8

CONCLUSIONS

8.1 Summary

We used realistic three-dimensional hydrodynamic simulations to study solar and stellar convection and its interaction with acoustic waves excited by turbulent convection. The properties of the acoustic modes in the simulations are very similar to the observed results. This implies that the code reproduces the basic properties of solar convection and its interaction with oscillations. We can therefore use the simulated modes to study p-mode properties that are not directly observable.

We investigated the asymmetry of the acoustic mode power spectra. We found that the temperature measured at some fixed geometrical depth corresponding to $<\tau_{\rm cont}>=1$ has same asymmetry as the velocity, while the temperature measured at optical depth $\tau_{\rm cont}=1$ has asymmetry similar to the intensity. The cause of these differences is the non-linear dependence of opacity on the temperature. Hotter local temperature leads to larger opacity, and the observed photons escape from higher, cooler layers. This effect reduces the radiation temperature in a non-uniform way across the mode peak, reversing the asymmetry. This indicates that the asymmetry reversal between the intensity and velocity can be produced by radiative transfer on

the surface of the simulated convection zone.

Acoustic source locations affect the mode spectra asymmetries. Positions of spectral maxima (eigenfrequencies) are fixed for a given resonant cavity, while positions of spectral minima depend on the source depths. They shift to higher frequencies for deeper source locations, thus changing the asymmetry sense. We studied the velocity asymmetry dependence on depth and used simple analytical models to find the source locations. Our results are very close to those predicted by other investigators: acoustic sources are located between the visible source and up to several hundred kilometers beneath it, depending on the source type. Modes of higher frequencies are excited by sources located closer to the surface, while low frequency modes are driven by deeper sources. This result reinforces the contemporary idea that the oscillations are driven by subsurface turbulent convective motions.

We studied the properties of spatial and temporal power spectra of convective parameters. Analytical predictions of the acoustic mode excitation rates are very sensitive to the details of the turbulent energy spectra. A Gaussian function is usually assumed for the temporal spectrum and a Kolmogorov scaling law for the spatial spectrum. We showed that spatial and temporal spectra exhibit different functional forms at different wavenumbers and frequencies. At low wavenumbers, temporal spectra are well represented by power laws, while at high wavenumbers they are exponential. At low frequencies, spatial spectra obey the Kolmogorov scaling law over a substantial inertial range; at high frequencies, there is no signature of the Kolmogorov energy cascade. One should be cautious when assuming general functional forms of these spectra in acoustic noise generation calculations.

We also used simulations of surface convection in other stars to learn how the interaction between the turbulent convection and oscillations manifests itself in different stars, and how mode excitation rates depend on the global stellar parameters. The simulations of only 9 main sequence stars and one subgiant were available to us, therefore our statistics is very incomplete. We found that the acoustic mode driving per unit area is practically independent of surface gravity, but increases with increasing stellar effective temperature. This happens because in hotter stars the convective flux is larger as temperature and velocity fluctuations are larger, and as a result, the excitation rates are higher.

8.2 Future Work

The results of the numerical simulations will help in interpreting the results of ground-based and space-based observations of solar-type oscillations. These results can offer important insights into the physics of both the turbulent convection and oscillations. The numerical simulations are capable of providing a comprehensive view of how the properties of turbulence-driven stellar oscillations change across the main-sequence stars on the HR diagram. The numerical results can be used to investigate the contribution of various sources (Reynolds stress and entropy fluctuations) to the energy of acoustic and surface gravity waves to determine the principal source of stochastic wave excitation in stars. The numerical simulations also will provide important characteristics of the oscillation power spectrum, the amplitude distribution, the line width and line asymmetry of the oscillation lines, the frequency shift, and the phase relation between the Doppler velocity and fluctuation of continuum intensity and

spectral lines. Knowledge of these parameters will allow use of asteroseismology data for diagnostics of stellar convection and turbulence. These characteristics are also important for planning the asteroseismology studies using data from NASA's Kepler mission and other ground-based and space observations. In addition, the simulation results will be used for testing and calibrating mixing length theories commonly employed in stellar evolution theories, and for developing a theory of interaction between waves and turbulence in stars.

REFERENCES

Abrams, D. & Kumar, P. 1996, ApJ, 472, 882

Asplund, M., Ludwig, H.-G., Nordlund, A., & Stein, R. F. 2000, A&A, 359, 669

Böhm-Vitense, E. 1958, Zeitschrift für Astrophysics, 46, 108

Baglin, A. & The COROT Team. 1998, in IAU Symp. 185: New Eyes to See Inside the Sun and Stars, 301

Balmforth, N. J. 1992, MNRAS, 255, 639

Balmforth, N. J. & Gough, D. O. 1990, ApJ, 362, 256

Basu, S., Christensen-Dalsgaard, J., Schou, J., Thompson, M. J., & Tomczyk, S. 1996, Bulletin of the Astronomical Society of India, 24, 147

Bedding, T. R., Butler, R. P., Kjeldsen, H., et al. 2001, ApJ, 549, L105

Bedding, T. R. & Kjeldsen, H. 2003, Publications of the Astronomical Society of Australia, 20, 203

Bogdan, T. J., Braun, D. C., Lites, B. W., & Thomas, J. H. 1998, ApJ, 492, 379

Bogdan, T. J., Cattaneo, F., & Malagoli, A. 1993, ApJ, 407, 316

Bouchy, F. & Carrier, F. 2001, A&A, 374, L5

Bouchy, F. & Carrier, F. 2002, A&A, 390, 205

Braun, D. C., Labonte, B. J., & Duvall, T. L. 1988, BAAS, 20, 701

Buzasi, D. 2002, in ASP Conf. Ser. 259: IAU Colloq. 185: Radial and Nonradial Pulsations as Probes of Stellar Physics, 616

Cally, P. S. & Bogdan, T. J. 1997, ApJ, 486, L67

Canuto, V. M. & Mazzitelli, I. 1991, ApJ, 370, 295

Carrier, F. & Bourban, G. 2003, A&A, 406, L23

Chou, D., Chou, H., Hsieh, Y., & Chen, C. 1996, ApJ, 459, 792

Christensen-Dalsgaard, J. 1988, in IAU Symp. 123: Advances in Helio- and Asteroseismology, 295

Christensen-Dalsgaard, J. 2002, Reviews of Modern Physics, 74, 1073

Christensen-Dalsgaard, J. & Berthomieu, G. 1991, Theory of solar oscillations (Solar interior and atmosphere (A92-36201 14-92). Tucson, AZ, University of Arizona Press, 1991, p. 401-478.), 401-478

Christensen-Dalsgaard, J. & Frandsen, S. 1983, Sol. Phys., 82, 165

Christensen-Dalsgaard, J. & Frandsen, S. 1983, Sol. Phys., 82, 469

Däppen, W., Mihalas, D., Hummer, D. G., & Mihalas, B. W. 1988, ApJ, 332, 261

Deubner, F.-L. 1975, A&A, 44, 371

Deubner, F.-L. & Fleck, B. 1989, A&A, 213, 423

Duvall, T. L., Jefferies, S. M., Harvey, J. W., Osaki, Y., & Pomerantz, M. A. 1993a, ApJ, 410, 829

Duvall, T. L., Jefferies, S. M., Harvey, J. W., & Pomerantz, M. A. 1993b, Nature, 362, 430

Espagnet, O., Muller, R., Roudier, T., & Mein, N. 1993, A&A, 271, 589

Fan, Y., Braun, D. C., & Chou, D.-Y. 1995, ApJ, 451, 877

Frandsen, S., Carrier, F., Aerts, C., et al. 2002, A&A, 394, L5

Gabriel, M. 1993, A&A, 274, 935

Georgobiani, D., Kosovichev, A. G., Nigam, R., Nordlund, Å., & Stein, R. F. 2000, ApJ, 530, L139

Georgobiani, D., Stein, R. F., & Nordlund, A. 2001, in ESA SP-464: SOHO 10/GONG 2000 Workshop: Helio- and Asteroseismology at the Dawn of the Millennium, 583

Georgobiani, D., Stein, R. F., & Nordlund, Å. 2003, ApJ, 596, 698

Goldreich, P. & Keeley, D. A. 1977, ApJ, 212, 243

Goldreich, P. & Kumar, P. 1990, ApJ, 363, 694

Goldreich, P., Murray, N., & Kumar, P. 1994, ApJ, 424, 466

Goode, P. R., Strous, L. H., Rimmele, T. R., & Stebbins, R. T. 1998, ApJ, 495, L27

Gough, D. O. 1977, ApJ, 214, 196

Hill, F., Fischer, G., Grier, J., et al. 1994, Sol. Phys., 152, 321

Houdek, G. 2002, in Radial and Nonradial Pulsations as Probes of Stellar Physics, ed. C. Aerts, T. R. Bedding, & J. Christensen-Dalsgaard, ASP Conf. Ser. 259, IAU Coll. 185, 447

Houdek, G., Balmforth, N. J., Christensen-Dalsgaard, J., & Gough, D. O. 1999, A&A, 351, 582

Houdek, G., Rogl, J., Balmforth, N. J., & Christensen-Dalsgaard, J. 1994, in GONG'94: Helio- and astero-seismology from the earth and space, ed. R. K. Ulrich, E. J. Rhodes, Jr., & W. Däppen, ASP, 641–644

Kjeldsen, H., Bedding, T. R., Viskum, M., & Frandsen, S. 1995, AJ, 109, 1313

Kolmogorov, A. N. 1941, Doklady Akad. Nauk SSSR, 32, 16

Kosovichev, A. G. & Duvall, T. L. 1997, in ASSL Vol. 225: SCORe'96: Solar Convection and Oscillations and their Relationship, 241–260

Kumar, P. 1994, ApJ, 428, 827

Kumar, P. 1997, in ASSL Vol. 225: SCORe'96: Solar Convection and Oscillations and their Relationship, 161–169

Kumar, P. & Basu, S. 1999, ApJ, 519, 389

Kurucz, R. L. 1992a, Rev. Mex. Astron. Astrofis., 23, 45

Kurucz, R. L. 1992b, Rev. Mex. Astron. Astrofis., 23, 181

Leibacher, J. W. & Stein, R. F. 1971, Astrophys. Lett., 7, 191

Leighton, R. B., Noyes, R. W., & Simon, G. W. 1962, ApJ, 135, 474

Lighthill, M. J. 1952, Royal Society of London Proceedings Series A, 211, 564

Lindsey, C. & Braun, D. C. 1997, ApJ, 485, 895

Ludwig, H. & Nordlund, A. 2000, in Stellar Astrophysics, Proceedings of the Pacific Rim Conference held in Hong Kong, 1999. Edited by L. S. Cheng, H. F. Chau, K. L. Chan, and K. C. Leung, published by Kluwer Academic Publishers, The Netherlands, 2000, 37

Ludwig, H.-G., Freytag, B., & Steffen, M. 1999, A&A, 346, 111

Marmolino, C. & Severino, G. 1991, A&A, 242, 271

Martić, M., Schmitt, J., Lebrun, J.-C., et al. 1999, A&A, 351, 993

Matthews, J. M., Kuschnig, R., Walker, G. A. H., et al. 2000, in ASP Conf. Ser. 203: IAU Colloq. 176: The Impact of Large-Scale Surveys on Pulsating Star Research, 74–75

Monin, J. S. & Yaglom, A. M. 1975, Statistical Fluid Mechanics: Mechanics of Turbulence Vol.2 (Cambridge: MIT Press)

Morel, P., Berthomieu, G., Provost, J., & Thévenin, F. 2001, A&A, 379, 245

Musielak, Z. E., Rosner, R., Stein, R. F., & Ulmschneider, P. 1994, ApJ, 423, 474

Nesis, A., Hanslmeier, A., Hammer, R., et al. 1993, A&A, 279, 599

Nigam, R. & Kosovichev, A. G. 1998, ApJ, 505, L51

Nigam, R. & Kosovichev, A. G. 1999, ApJ, 510, L149

Nigam, R., Kosovichev, A. G., Scherrer, P. H., & Schou, J. 1998, ApJ, 495, L115

Nordlund, A. 1982, A&A, 107, 1

Nordlund, A., Spruit, H. C., Ludwig, H.-G., & Trampedach, R. 1997, A&A, 328, 229

Nordlund, Å. & Stein, R. F. 1989, in NATO ASIC Proc. 263: Solar and Stellar Granulation, 453

Nordlund, Å. & Stein, R. F. 1990, Computer Physics Communications, 59, 119

Nordlund, A. & Stein, R. F. 1991, in NATO ASIC Proc. 341: Stellar Atmospheres - Beyond Classical Models, 263

Nordlund, A. & Stein, R. F. 1998, in IAU Symp. 185: New Eyes to See Inside the Sun and Stars, 199

Nordlund, Å. & Stein, R. F. 2001, ApJ, 546, 576

Oliviero, M., Severino, G., Straus, T., Jefferies, S. M., & Appourchaux, T. 1999, ApJ, 516, L45

Rast, M. P. 1999, ApJ, 524, 462

Rast, M. P. & Bogdan, T. J. 1998, ApJ, 496, 527

Rieutord, M., Roudier, T., Malherbe, J. M., & Rincon, F. 2000, A&A, 357, 1063

Roxburgh, I. & Favata, F. 2003, Ap&SS, 284, 17

- Roxburgh, I. W. & Vorontsov, S. V. 1997, MNRAS, 292, L33
- Samadi, R., Georgobiani, D., Trampedach, R., et al. 2004, ApJ, (in preparation)
- Samadi, R. & Goupil, M.-J. 2001, A&A, 370, 136
- Samadi, R., Goupil, M.-J., Lebreton, Y., & Baglin, A. 2001, in ESA SP-464: SOHO 10/GONG 2000 Workshop: Helio- and Asteroseismology at the Dawn of the Millennium, 451
- Samadi, R., Nordlund, Å., Stein, R. F., Goupil, M. J., & Roxburgh, I. 2003a, A&A, 404, 1129
- Samadi, R., Nordlund, Å., Stein, R. F., Goupil, M. J., & Roxburgh, I. 2003b, A&A, 403, 303
- Scherrer, P. H., Bogart, R. S., Bush, R. I., et al. 1995, Sol. Phys., 162, 129
- Severino, G., Straus, T., & Jefferies, S. M. 1998, in Structure and Dynamics of the Interior of the Sun and Sun-like Stars SOHO 6/GONG 98 Workshop Abstract, June 1-4, 1998, Boston, Massachusetts, 53
- Skartlien, R. 2001, ApJ, 554, 488
- Skartlien, R. & Rast, M. P. 2000, ApJ, 535, 464
- Stein, R. F. 1967, Sol. Phys., 2, 385
- Stein, R. F. & Nordlund, A. 1989, ApJ, 342, L95
- Stein, R. F. & Nordlund, Å. 1991, in Challenges to Theories of the Structure of Moderate-Mass Stars, Proceedings of a Conference held at the Institute for Theoretical Physics, University of California, Santa Barbara, CA, USA, 19-22 June 1990. Edited by D. Gough and J. Toomre. Springer-Verlag Berlin Heidelberg New York. Also Lecture Notes in Physics, volume 388, 1991, 195
- Stein, R. F. & Nordlund, Å. 1998a, in Structure and Dynamics of the Interior of the Sun and Sun-like Stars SOHO 6/GONG 98 Workshop Abstract, June 1-4, 1998, Boston, Massachusetts, 693
- Stein, R. F. & Nordlund, A. 1998b, ApJ, 499, 914
- Stein, R. F. & Nordlund, A. 2000, Sol. Phys., 192, 91
- Stein, R. F. & Nordlund, A. 2001, ApJ, 546, 585
- Straus, T., Fleck, B., Severino, G., et al. 1998, in ESA SP-417: Crossroads for European Solar and Heliospheric Physics. Recent Achievements and Future Mission

- Possibilities, 293
- Tassoul, M. 1980, ApJS, 43, 469
- Trampedach, R., Christensen-Dalsgaard, J., Nordlund, Å., & Stein, R. F. 2003a, ApJ, (in preparation)
- Trampedach, R., Stein, R. F., Christensen-Dalsgaard, J., & Nordlund, Å. 1998, in Theory and tests of convection in stellar structure, ed. Á. Giménez, E. F. Guinan, & B. Montesinos, ASP conf. series, First Granada Workshop, 233–236
- Trampedach, R., Stein, R. F., Christensen-Dalsgaard, J., & Nordlund, Å. 2003b, ApJ, (in preparation)
- Ulrich, R. K. 1970, ApJ, 162, 993
- Unno, W. 1964, Transactions of the International Astronomical Union, 12, B555
- Vorontsov, S. V., Jefferies, S. M., Duval, T. L., & Harvey, J. W. 1998, MNRAS, 298, 464